DYNAMIC TUNNELING FORCE MICROSCOPY

AND SINGLE ELECTRON TUNNELING

FORCE SPECTROSCOPY

by

Jon Paul Johnson

A dissertation submitted to the faculty of
The University of Utah
in partial fulfillment of the requirements for the degree of

Doctor of Philosophy

in

Physics

Department of Physics and Astronomy

The University of Utah

August 2010

The University of Utah Graduate School

STATEMENT OF DISSERTATION APPROVAL

The dissertation of **Jon Paul Johnson**

has been approved by the following supervisory committee members:

Clayton C. Williams	, Chair	**6/4/2010** Date Approved
Scott L. Anderson	, Member	**6/4/2010** Date Approved
Christoph Böhme	, Member	**6/4/2010** Date Approved
John Lupton	, Member	**6/4/2010** Date Approved
Mikhail Raikh	, Member	**6/4/2010** Date Approved

and by **David B. Kieda**, Chair of the Department of **Physics and Astronomy**

and by Charles A. Wight, Dean of The Graduate School.

ABSTRACT

An introduction to Scanning Probe Microscopy is given along with some basic principles in the detection of electron tunneling by Atomic Force Microscopy (AFM) using electrostatic force. Dynamic Tunneling Force Microscopy (DTFM), a new scanned probe force-detected tunneling technique, is presented and described, in which shuttling of electrons between electron trap states and a conductive AFM probe provides a means to image these trap states with subnanometer spatial resolution. The further development of Single Electron Tunneling Force Spectroscopy (SETFS) is described, providing a method to measure the energy of electronic trap states. It is used to find the energy spectrum of individual monolayer-protected gold clusters. A novel technique is presented whereby the electron trap states' depth and energy are independently determined using SETFS. Finally, a new technique is described and explored, by which "single spin" electron spin resonance measurements can in principle be performed. The method employs the detection of magnetic resonance through spin dependent tunneling, providing a means to identify individual paramagnetic electron states in dielectric films with atomic spatial resolution.

To my wife, Bryanna—my reason for everything.

TABLE OF CONTENTS

LIST OF FIGURES

ACKNOWLEDGEMENTS

I thank Prof. Clayton Williams for his support during my time in his group, his motivational speeches, and for the excellent mentoring I have received from him.

Ning Zheng and Ezra Bussmann taught me to use the UHV microscope, and I thank them for their patience and willingness to help. Dustin Winslow and Adam Payne were always willing to discuss anything from politics to science. Thanks to Scott Anderson, Bill Kaden, and Will Kunkel for their help with the bare metal cluster work, though it's not included here.

I also thank my committee for their support. If someday I become half the scientist that any one of them is, I will consider myself successful. Christoph Böhme with Dane McCamey explained the concepts behind mangetic resonance. John Lupton's condensed matter course was excellent, as was Scott Anderson's on surface science—both broadened my view. Thanks to Mikhail Raikh for his genuine interest in my future.

Thanks also to the professors I worked for in various teaching situations and for their mentoring and support: Rich Ingebretsen, George Williams, John DeFord, Paolo Gondolo, Gernot Laicher, Dave Chapman, Holly Godsey, and Ian Harvey. Teaching is my professional goal, and I am a better teacher today because of each one of them.

Finally, thanks to my wife, two boys, parents, parents-in-law, and even siblings who supported me immensely during my time as a graduate student. Although it may sound trite, I couldn't have done it without them.

CHAPTER 1

INTRODUCTION

1.1 Motivation

The performance of semiconductor devices such as transistors is limited by the properties of the insulating layers used to couple the gate electrode to the channel [1, 2]. Electron traps in these dielectric layers are localized defect states that can accommodate one or two electrons, and are undesirable in device fabrication because they can provide a pathway for charge to hop through the oxide films, change the threshold voltages for device switching, and reduce carrier mobility in the channel [2, 3]. These effects decrease device performance. In flash memory, charge traps influence the performance by changing the retention time of stored charge.

As the effect of individual electrons becomes more important to device operation, knowledge about the spatial and energetic distribution of these trap states is critical to optimize the insulating films. In this work, new methods to characterize and image these charge traps in dielectrics are presented, for the first time allowing subnanometer spatial imaging of their location in thick films, along with a spectroscopic characterization of their energies in the band gap.

1.2 Scanning probe microscopy and previous work

The force-detected tunneling discussed in this work is achieved using an Atomic Force Microscope (AFM). AFM is part of a family of microscopic techniques called Scanning Probe Microscopy (SPM), which do not have the same diffraction limit on resolution that far-field optical microscopy has. It takes its name from the way a small tip is scanned over a surface while recording information about the interaction between the tip and the surface. The spatial scanning is normally accomplished using a high-precision piezoelectric scanner, which gives fine enough control of the tip position that individual atoms on surfaces can be resolved, first achieved with Scanning Tunneling Microscopy (STM) [4]. For three decades, many variations of SPM have offered unprecedented access to information about the atomic and electronic structure of surfaces, and this section describes several of these techniques and their relation to the work in this dissertation.

1.2.1 Scanning Tunneling Microscopy

The first successful implementation of SPM, Scanning Tunneling Microscopy (STM), was demonstrated by Binnig and Rohrer [5]. In STM, the interaction between a metal tip and a conducting sample is an electrical current of tunneled electrons. STM has been very successful since its discovery because it relies on quantum tunneling of electrons through a vacuum barrier, and the tunneling rate is extremely sensitive to changes in the gap distance [6, 7]. The tunneling rate has been calculated and measured and typically increases by an order of magnitude for every 1Å change in tip-sample gap [8]. The tunneling current must be large enough to detect, typically greater than about

100fA (~10^6 e^- per second) [9]. STM is therefore able to image insulating films only as long as they are thin enough to allow sufficient electron tunneling and even detect trap states in these films [10, 11], but in Chapter 2 a new technique is presented which images these localized electron trap states with subnanometer resolution. Because of the requirement on tunneling current, the electrons in the STM current cannot be used to directly image electronic states with electron dwell times longer than about 1μs. The tunneling current can be affected by such states, but the tunneling current must pass through these states.

In addition to topographical imaging, the density of states can be mapped out by measuring the differential current over a single point as the bias voltage is ramped in Scanning Tunneling Spectroscopy (STS), a form of I-V spectroscopy [12]. Semiconductors in particular have been studied by STS [13-15] but as with STM, completely nonconducting surfaces are not addressable by STS. STS is well-suited to finding the spectrum of metal and semiconductor nanoparticles when the particles are placed on a conducting surface [16-19], but the proximity of the metal surface and tip may shift the energy spectrum of the particles and broaden the peaks in the dI/dV spectra [20]. With this technique, molecule-like, size-dependent spectra due to quantum confinement effects have been observed [18, 20]. A method for direct tunneling to the electronic states of Au monolayer-protected clusters that are placed on completely non-conducting surfaces is demonstrated in Chapter 3, which allows spectroscopy of these particles in a more electrically isolated environment.

Many techniques related to STM and STS give additional information about surfaces or control of their environment. Electronic trap states have been observed via the

change in tunneling current as the occupation of these states changes [10]. Individual atoms and molecules have been manipulated by the tip to restructure the surface [21-23]. Spectroscopic information about subsurface electronic states and interfaces can be determined using Ballistic Electron Emission Microscopy [24, 25], which depends on ballistic transport of electrons through a thin metal electrode placed on an insulating or semiconducting layer. In BEEM, as in STM, the measured current passes through the states and no direct measurement of the charging of trap stats is available.

Magnetic samples can be imaged with atomic resolution by using a spin-dependent tunneling current in Spin-polarized Scanning Tunneling Microscopy (SPSTM) [26], which can image magnetic domains on conductive magnetic materials. In SPSTM, the tip is replaced by a magnetic material that provides a spin-dependent density of states so that the tunneling current is a function of the magnetic polarization of the states in the sample that the electrons tunnel to. SPSTM has achieved atomic-resolution imaging of the local polarization. SPSTM is only useful on conductive samples, and is not aimed at detecting individual paramagnetic states but at imaging magnetic samples. Detection of single electron spins has been demonstrated using a number of techniques, such as magnetic resonance force microscopy (MRFM) [27], electrically detected magnetic resonance (EDMR) [28, 29], optically detected magnetic resonance (ODMR) [30-32], and possibly ESR-scanning tunneling microscopy [33]. Of these, only the optical method has detected a single spin at room temperature—the spin of an individual NV center in diamond, but not with nanometer-scale resolution. There is a possibility that coupling individual diamond NV centers to other individual spins could be used in some way to sense spins close to it at room temperature [34, 35], although to the present this has not

been demonstrated. The MRFM method has detected a single spin, but it requires long averaging times to detect it and must be performed at low temperature. A new method based on the force detection of individual charges is introduced in Section 1.3 that could allow single-spin detection at room temperature with atomic-scale resolution.

1.2.2 Atomic Force Microscopy

Atomic Force Microscopy (AFM) was developed to image nonconducting surfaces [36, 37]. In AFM the same scanning technique is employed, but the force between the tip and sample is the interaction of interest. The effects of this interaction is measured through the deflection of a cantilever, giving high-sensitivity force measurements and even allowing atomic resolution of nonconducting surfaces [38-40] and chemical identification of individual surface atoms [41].

1.2.3 Electrostatic Force Microscopy and related techniques

There are numerous Scanning Probe Micrsocopies that are due to the electrostatic force between the tip and sample. Electrostatic Force Microscopy (EFM) and Scanning Capacitance Microscopy (SCM) are the simplest implementations [42-44]. EFM is sensitive to electrostatic forces between the sample and tip, and so can be used to image electrostatic potentials and the way charge is distributed in a nonconducting sample. To reduce sensitivity to forces due to other tip-sample interactions, the EFM signal is measured by applying an alternating bias voltage between tip and sample, which also allows the sign of the measured charge to be found [42]. Another technique similar to EFM and SCM is Kelvin Probe Force Microscopy (KPFM), with which the contact

potential difference between two metals (or between a metal and a semiconductor, etc.) can be measured, again using the electrostatic force on the tip [45]. SCM has been applied to investigating local charge defects in dielectric films (for example, see [46]), but none of these techniques has the ability to address individual charge trap states because the best spatial resolution is generally limited by the size of the tip.

1.2.4 Single Electron Tunneling Force Microscopy

EFM was first shown to be sensitive to the electrostatic force from single electrons by Schönenberger, et al. [47], in the change of the EFM signal as the charge on a surface left the measurement region. Klein and Williams observed single electron tunneling between tip and sample by recording the changes in amplitude induced on the cantilever after a tunneling event [48]. Later, single electron tunneling was observed by Bussmann and Williams by monitoring the shift in the frequency of the cantilever's resonance due to changes in the electrostatic force gradient on the tip caused by the tunneling electron at the sample surface [49]. This technique was used to perform spectroscopy of a single trap state in SiO_2 and also to image states with nanometer-scale resolution [50, 51]. Single Electron Tunneling Force Spectroscopy (SETFS) has another advantage over STS, namely that because the tunneling rate can be many orders of magnitude smaller in SETFS than what is required STS, the metal tip electrode can be kept further from states under study. As mentioned above, the electronic coupling to the metal electrodes in STS can broaden or shift the peaks in the energy spectrum. The repeatability of the SETFM imaging method was not perfect due to apparent charge fluctuations at the dielectric surface. A similar spectroscopic method, which relies on

inducing electrons to tunnel between trap states and the back electrode, has been used in spectroscopic studies of nanoparticles [52, 53], but because this method does not involve tunneling between the tip and sample, it does not provide imaging with STM-like resolution.

1.3 Introduction to work described in this dissertation

This work describes advances in nanoscale imaging of electronic trap states in three dimensions and spectroscopy of both trap states and metal nanoclusters, as well as an introduction to a new technique to detect individual electronic spins, potentially with subnanometer spatial resolution and at room temperature. The spatial imaging of trap states described in [51] was improved by developing a novel technique called Dynamic Tunneling Force Microscopy (DTFM), described in Chapter 2, which is sensitive to electron shuttling between tip and sample. This removes the sensitivity to background fluctuations in the surface charge. For the first time, trap states are imaged with sub-nanometer resolution in SiO_2 and with similar resolution in a hafnium silicate film. The work by Bussmann [51] led to a new method for performing spectroscopy. Chapter 3 describes the use of an improved implementation of Single Electron Tunneling Force Spectroscopy (SETFS) to obtain the energy spectrum of electronic states in gold monolayer-protected clusters (MPCs). The work in Chapter 3 was done jointly with Ning Zheng. Another new capability is described in Chapter 4, involving the measurement of both the depth and energy of buried trap states in dielectric films using SETFS. The depth and energy of states in a film of HfO_2 is measured. Chapter 5 explores the possibility of employing the single electron tunneling measurement to perform single spin electron spin

resonance measurements, by tunneling between paramagnetic states on either side of the gap and applying an appropriate RF magnetic field to manipulate the spins in a static magnetic field. Chapter 6 summarizes the work in this dissertation and future prospects.

1.4 Principles of single electron tunneling force microscopy

1.4.1 Force detection through frequency shift

Because all of the methods discussed in this work are based on force detection through frequency shift, a description of this principle is given here. When an oscillating AFM cantilever experiences a force gradient, the resonant frequency is shifted from its natural resonance f_0 [54] and the new frequency is given by the expression

$$f = f_0 \sqrt{1 - \frac{F'_{eff}}{K}}\,, \tag{1}$$

where K is the spring constant and F'_{eff} is the effective force gradient. This can be expanded to get

$$f = f_0 \sqrt{1 - \frac{F'_{eff}}{K}} = f_0 - \frac{f_0 F'_{eff}}{2K} + f_0 O\left(\frac{F'_{eff}}{K}\right)^2. \tag{2}$$

For small effective force gradients compared to the spring constant K, higher-order terms can be ignored and the frequency shift is approximated by

$$df \equiv f - f_0 \approx \frac{f_0 F'_{eff}}{2K}. \tag{3}$$

The effective force gradient for a tip interaction force F and tip oscillation amplitude A has been shown generally to be [55]

$$F'_{eff} = -\frac{2}{\pi A}\int_{-1}^{+1} F\left(z + A(1+u)\right)\frac{u}{\sqrt{1-u^2}}du, \tag{4}$$

where z is the distance of closest approach, and the substitution $u = \cos(2\pi f_0 t)$ has been made. The effective force gradient found in equation (4) can be substituted into equation (3) to find how far the oscillator is detuned from its resonance by the interaction force.

1.4.2 Tunneling conditions

The techniques described in this work also depend on quantum tunneling between electronic states. In order for tunneling to occur from tip to sample or vice versa, two conditions must be met. The first is an energy condition, namely that there must be an available empty electronic state at the same energy as a filled state across the tunneling gap. See Figure 1.1. The second condition, also illustrated in Figure 1.1, is a spatial condition. The tunneling rate depends on the overlap of the filled tip state wavefunction and the empty electronic state wavefunction. If the states are too far apart, the tunneling rate will be too small for tunneling to occur in the measurement time.

It is the wavefunction overlap condition and the exponential decay of the wavefunction in classically forbidden regions that are the source of the high spatial resolution in STM and DTFM [8]. Zheng calculated the tunneling rate as a function of the spatial and energetic location of states in dielectric films [8]. The requirement imposed by

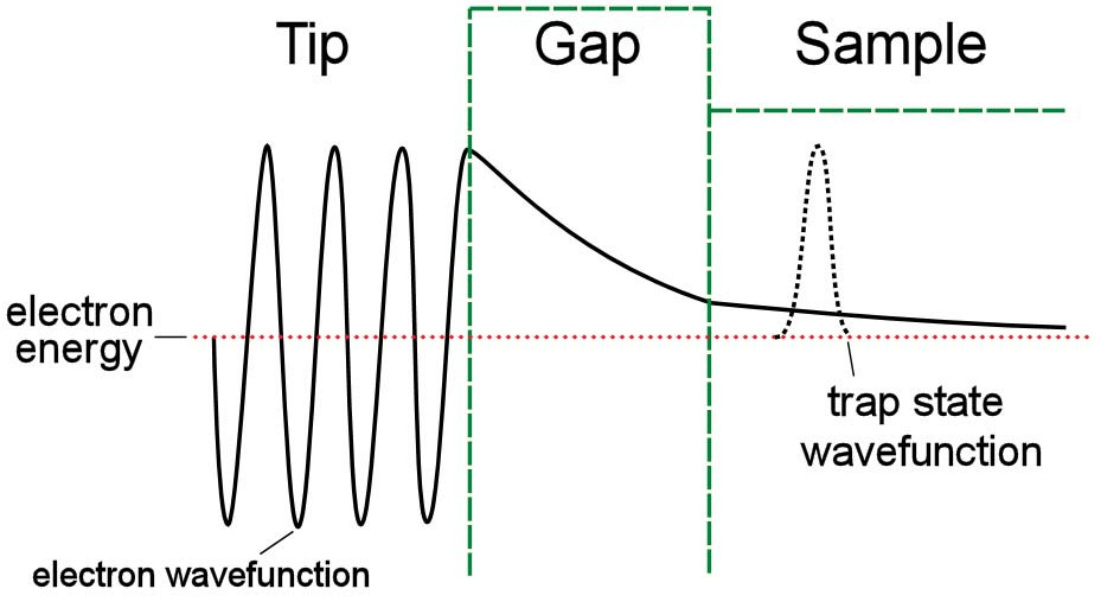

Figure 1.1 Energy and wavefunction overlap conditions for tunneling. This is an energy diagram (dashed lines) with overlaid wavefunctions for a filled electronic state in the tip (solid line) and an empty trap state in the sample (dotted line). Electron tunneling between the tip and sample is dependent on two conditions being satisfied—an energy condition and a spatial (tunneling rate) condition. First, a filled tip state must be at the same energy as an empty state across the gap for tunneling to occur. Second, the electron wavefunction must overlap sufficiently with the state in the sample so that tunneling can occur during the measurement time. In the classically forbidden regions, the wavefunction decays exponentially.

the energy condition makes it possible to perform spectroscopy. The position of the Fermi energy of the tip can be moved relative to states in the sample by applying a bias between the tip and the sample. It is important to note that not all of the voltage is dropped in the tip-sample gap. There is electric field in the dielectric, as well, so proper care must be taken to determine how much of the applied voltage is dropped between the tip and sample states.

1.5 References

[1] Muller D A, Sorsch T, Moccio S, Baumann F H, Evans-Lutterodt K and Timp G 1999 *Nature* **399** 758

[2] Wilk, G D, Wallace R M and Anthony J M 2001 *J. Appl. Phys.* **89** 5243

[3] Xu Z, Houssa M, De Gent S and Heyns M 2002 *Appl. Phys. Lett.* **80** 1975

[4] Binnig G, Rohrer H, Gerber C and Weibel E 1983 *Phys. Rev. Lett.* **50** 120

[5] Binnig G, Rohrer H, Gerber C and Weibel E 1982 *Phys. Rev. Lett.* **49** 57

[6] Binnig G, Garcia N, Rohrer H, Soler J M and Flores F 1984 *Phys. Rev. B* **30** 4816

[7] Chen, J C 1993 *Introduction to Scanning Tunneling Microscopy*, Oxford University Press, New York, pp. 53-74

[8] Zheng N, Williams C C, Mishchenko E G and Bussmann E 2007 *J. Appl. Phys.* **101** 093702

[9] Ferrari G and Sampietro M 2007 *Rev. Sci. Instrum.* **78** 094703

[10] Welland M E and Koch R H 1986 *Appl. Phys. Lett.* **48** 724

[11] Brobov K, Mayne A J and Dujardin G 2001 *Nature* **413** 616

[12] Feenstra R M, Thompson W A and Fein A P 1986 *Phys. Rev. Lett.* **56** 608

[13] Hamers R J 1989 *Ann. Rev. Phys. Chem.* **40** 531

[14] Tromp R M 1989 *J. Phys.: Condens. Matter* **1** 10211

[15] Feenstra R M and Lutz M A 1990 *Phys. Rev. B* **42** 5391

[16] Wilkins R, Ben-Jacob E and Jaklevic R C 1989 *Phys. Rev. Lett.* **63** 801

[17] Amman M, Field S B and Jaklevic R C 1993 *Phys. Rev. B* **48** 104

[18] Banin U, Cao Y, Katz D and Millo O 1999 *Nature* **400** 542

[19] Zhang H, Schmid G and Hartmann U 2003 *Nano Lett.* **3** 305

[20] Jdira L, Overgaag K, Stiufiuc R, Grandidier B, Delerue C, Speller S, and Vanmaekelbergh D 2008 *Phys. Rev. B* **77** 205308

[21] Eigler D M and Schweizer E K 1990 *Nature* **344** 524

[22] Becker R S, Higashi G S, Chabal Y J and Becker A J 1990 *Phys. Rev. Lett.* **65** 1917

[23] Stipe B C, Rezaei M A and Ho W *Science* **279** 1907

[24] Kaiser W J and Bell L D 1988 *Phys. Rev. Lett.* **60** 1406

[25] Kaczer B, Meng Z and Pelz J P 1996 *Phys. Rev. Lett.* **77** 91

[26] Wiesendanger R, Güntherodt H-J, Güntherodt G, Gambino R J and Ruf R 1990 *Phys. Rev. Lett.* **65** 247

[27] Rugar D, Budakian R, Mamin H J, Chui B W 2004 *Nature* **430** 329

[28] Elzerman J M, Hanson R, Willems van Bevern L H, Witkamp B, Vandersypen L M K, and Kouwenhoven L P 2004 *Nature* **430** 431

[29] Xiao M, Martin I, Yblonovitch E and Jiang H W 2004 *Nature* **430** 435

[30] Wrachtrup J, von Borcyskowski C, Bernard J, Orrit M and Brown R 1993 *Phys. Rev. Lett.* **71** 3565

[31] Jelezko F, Gaebel T, Popa I, Gruber A and Wrachtrup J 2004 *Phys. Rev. Lett.* **72** 076401

[32] Hanson R, Gywat O and Awchalom D D 2006 *Phys. Rev. B* **74** 161203

[33] Mannasen Y, Hamers R J, Demuth J E and Castellano A J, Jr.1989 *Phys. Rev. Lett.* **62** 2531

[34] Maze J R, Stanwix P L, Hodges J S, Hong S, Taylor J M, Cappellaro P, Jiang L, Gurudev Dutt M V, Togan E, Zibrov A S, Yacoby A, Walsworth R L and Lukin M D 2008 *Nature* **455** 644

[35] Balasubramanian G, Chan I Y, Kolesov R, Al-Hmoud M, Tisler J, Shin C, Kim C, Wojcik A, Hemmer P R, Krueger A, Hanke T, Leitenstorfer A, Bratschitsch R, Jelezko F and Wrachtrup J 2008 *Nature* **455** 648

[36] Binnig G, Quate C F and Gerber C 1986 *Phys. Rev. Lett.* **56** 930

[37] Giessibl F J 2003 *Rev. Mod. Phys.* **75** 949

[38] Binnig G, Stoll E, Albrecht T R and Quate C F 1987 *Europhys. Lett.* **3** 1281

[39] Alexander S, Hellemans L, Marti O, Schneir J, Elings V, Hansma P K, Longmire M and Gurley J 1989 *Journ. Appl. Phys.* **65** 164

[40] Giessibl F J 1995 *Science* **267** 68

[41] Sugimoto Y, Pou P, Abe M, Jelinek P, Pérez R, Morita S and Custance O 2007 *Nature* **446** 64

[42] Martin Y, Abraham D W, Wickramasinghe H K 1988 *Appl. Phys. Lett.* **52** 1103

[43] Williams C C, Slinkman J, Hough W P, and Wickramasinghe H K 1989 *Appl. Phys. Lett.* **55** 1662

[44] Girard P 2001 *Nanotech.* **12** 485

[45] Nonnenmacher M, O'Boyle M P and Wickramasinghe H K 1991 *Appl. Phys. Lett.* **58** 2921

[46] Naitou Y, Arimura H, Kitano N, Horie S, Minami T, Kosuda M, Ogiso H, Hosoi T, Shimura T and Watanabe H 2008 *Appl. Phys. Lett.*, **92** 012112

[47] Schönenberger C and Alvarado S F 1990 *Phys. Rev. Lett.* **65** 3162

[48] Klein L J and Williams C C 2002 *Appl. Phys. Lett.* **81** 4589

[49] Bussmann E, Kim D J and Williams C C 2004 *Appl. Phys. Lett.* **85** 2538

[50] Bussmann E and Williams C C 2006 *Appl. Phys. Lett.* **88** 263108

[51] Bussmann E B, Zheng N and Williams C C 2006 *Nano Lett.* **6** 2577

[52] Dâna A and Yamamoto Y 2005 *Nanotech.* **16** S125

[53] Stomp R, Miyahara Y, Schaer S, Sun Q, Guo H, Grutter P, Studenikin S, Poole P and Sachrajda A 2005 *Phys. Rev. Lett.* **94** 056802

[54] Hölscher H, Schwarz U D and Wiesendanger R 1999 *Appl. Surf. Sci.* **140** 344

[55] Dürig U 1999 *Appl. Phys. Lett.* **75** 433

CHAPTER 2

DYNAMIC TUNNELING FORCE MICROSCOPY

This chapter contains a paper that was published in Nanotechnology (copyright IOP Publishing, ltd. iopscience.org/nano) Vol. 20 055701 (2009) entitled *Atomic scale imaging and spectroscopy of individual electron trap states by force detected dynamic tunnelling* by Jon Paul Johnson, Ning Zheng, and Clayton C. Williams. It contains the first imaging results from a new technique called Dynamic Tunneling Force Microscopy (DTFM). The paper has been reformatted to match the style of this dissertation.

DTFM is achieved by inducing and detecting the continuous shuttling of electrons to and from a trap state at the surface at a particular frequency, instead of injecting/extracting charge in a single direction. Because DTFM is only sensitive to signal at a particular shuttling frequency, it has the advantage that surface charge noise can be largely filtered out by using a lock-in amplifier to detect the change in the frequency shift that occurs at the shuttling frequency, providing the DTFM signal. The signal is analogous to an Alternating Current Scanning Tunneling Microscope (AC-STM) current. Because it relies on tunneling, the spatial resolution of the DTFM signal is, in principle, the same as for the STM. Depth dependent tunneling was observed in this experiment, which motivated the experiment described in Chapter 4.

2.1 Abstract

We report the first atomic-scale imaging and spectroscopic measurements of electron trap states in *completely nonconducting* surfaces by Dynamic Tunneling Force Microscopy/Spectroscopy. Single electrons are dynamically shuttled to/from individual states in thick films of hafnium silicate and silicon dioxide. The new method opens up surfaces that are inaccessible to STM for imaging and spectroscopy on an atomic scale.

2.2 Body

For two decades, the Scanning Tunneling Microscope (STM) has provided unprecedented atomic scale imaging and spectroscopy of metallic and semiconducting surfaces. Despite its enormous power, the STM is limited to surfaces of finite conductivity—a current greater than 0.1 picoamperes (~10^6 electrons/sec) is typically required. Electron trap states in *completely nonconducting* dielectric films cannot be directly detected by the STM. These localized electronic trap states are of great interest. In computer memory chips, such trap states degrade device performance [1], and in FLASH memory, they provide a basis for charge storage. These states may eventually be useful in quantum information processing.

Multiple attempts have been made to produce electron tunneling images of dielectric surfaces over the years. Kochanski in 1989 [2] and Weiss in 1993 [3] both attempted to do a form of AC tunneling to dielectric surfaces. These efforts did not produce convincing atomic scale imaging results, and the work was not continued. Additionally, STM and Ballistic Electron Emission Microscopy (BEEM) have been applied to the imaging of ultrathin dielectric films [4,5]. In STM and BEEM, however,

electrons do not tunnel directly to the trap states, but rather through the trap states or directly to the substrate. BEEM also requires a measurable tunneling current. Kelvin Probe Force Microscopy (KPFM), Electrostatic Force Microscopy (EFM) and Scanning Capacitance Microscopy (SCM) have also been used to investigate defects in insulators [6-12]. KPFM and EFM are sensitive only to the charge present at the surface, not to the electronic states themselves, so uncharged states cannot be observed. KPFM, EFM and SCM are also limited in spatial resolution to a value on the order of the tip radius.

Recently, Single Electron Tunneling Force Microscopy (SETFM) was demonstrated. Single electrons are manipulated, one at a time, between tip and individual trap states by quantum tunneling [13-15] and directly detected by the electrostatic force produced on the scanning probe tip. See Figure 2.1(a). This approach has enabled electronic spectroscopy of individual trap states, by direct tunneling from *substrate to state* [16-17], and from *tip to state* [18]. Tunneling between *tip and state* provides the ability to *image* the trap distribution in the dielectric surface with atomic scale spatial resolution [19]. The image repeatability in this earlier imaging work was modest, due to low frequency charge fluctuations at the dielectric surface.

In the approach described here, called Dynamic Tunneling Force Microscopy (DTFM), single electrons are *dynamically* shuttled to and from the electron trap states, providing a means to isolate the tunneling signal from these low frequency fluctuations.

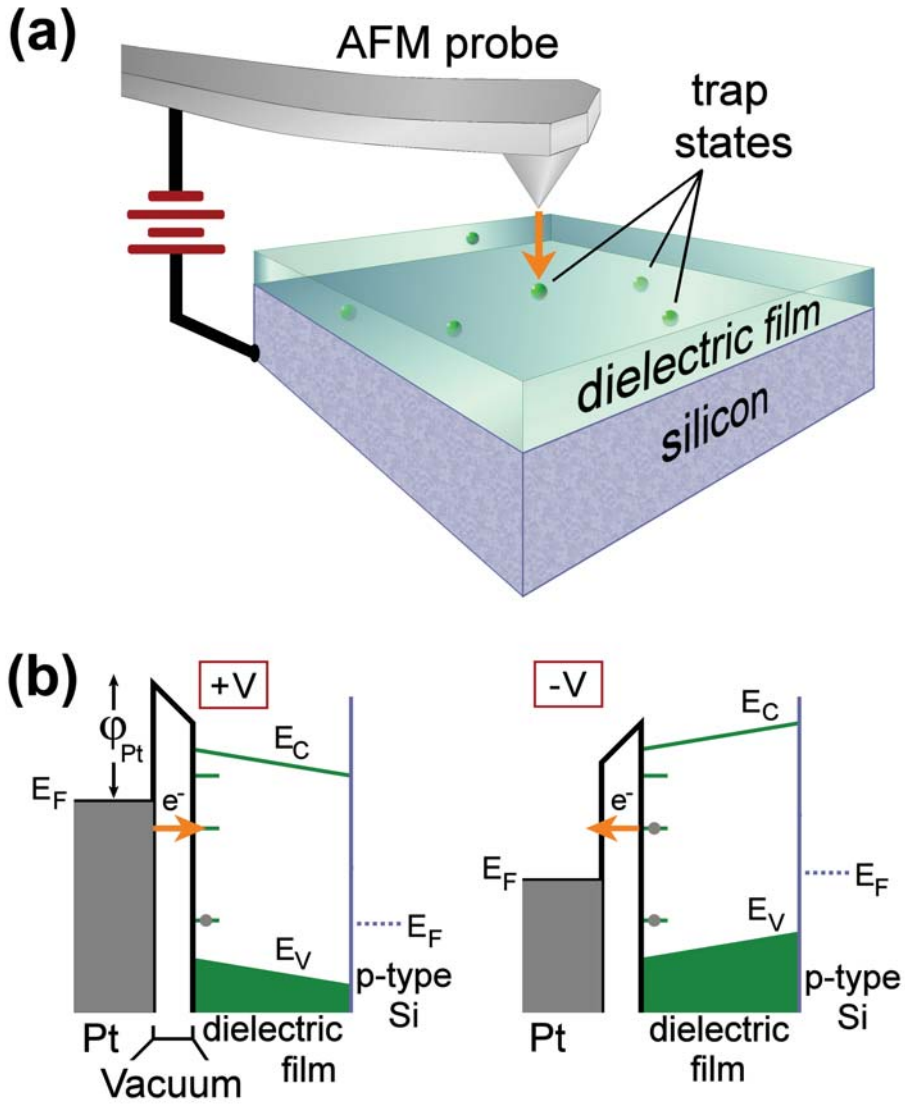

Figure 2.1. Dynamic tunneling system and energy diagram. (a) Individual electrons tunnel between a conductive tip and localized electronic states in a dielectric film, as a shuttling voltage waveform is applied. (b) Energy diagram illustrating how electrons are induced to tunnel to and from states at the surface, with positive and negative applied voltage.

The dynamic tunneling approach now provides beautiful, repeatable and direct images of individual trap states in completely nonconducting surfaces, with a spatial resolution comparable to that of the STM.

To understand how dynamic tunneling works, the energies of trap states and probe states must be considered. Trap states have energies that fall between the valence and conduction bands of the dielectric material. See Figure 2.1(b). When a metal DTFM probe tip is brought within tunneling range of an unfilled trap state in the dielectric surface, and the Fermi level of the tip (controlled by the applied voltage) is greater than the energy of the unfilled trap state, an electron will tunnel to the unfilled trap state. After the electron fills the trap state, the Fermi level of the probe tip can be lowered (by the applied voltage), and the electron in the trap will tunnel back to the tip. Thus, the voltage applied to the tip can exquisitely control the occupancy of the trap. In fact, the energy of the state can be measured by carefully noting the voltage at which the electron tunnels into or out of the trap state [18].

In Dynamic Tunneling Force Microscopy (DTFM) measurements, electrons are dynamically shuttled to/from trap states. Detecting this electron shuttling involves monitoring subtle changes in the resonance frequency of the oscillating AFM probe. The measurements are performed with an Omicron Multiprobe S Atomic Force Microscope (AFM) under a vacuum of 10^{-8} Torr at room temperature. A metal coated AFM probe (Mikromasch NSC15/Ti-Pt), with 40 nm oscillation amplitude and 50 N/m stiffness is brought within 1 nm (closest approach) of a dielectric surface. The oscillation amplitude is kept constant by a feedback loop (as in Dynamic Force Microscopy) on its natural resonance frequency near 280 kHz. A periodic electron shuttling voltage waveform at

300 Hz is applied to the sample (with the tip grounded), consisting of a positive voltage (typically 3 to 5 volts) for 85% of its duty cycle and a negative pulse voltage (-3 to -5 volts) for the remaining 15%. See Figure 2.2(a). The positive and negative voltage levels (such as +3 and -3 volts) are chosen to be equal in magnitude and opposite in sign with respect to the flat band voltage, so as to avoid a large frequency shift caused solely by the applied voltage (the background electrostatic force gradient and frequency shift are proportional to the square of the applied voltage with respect to the flat band voltage [14]). Therefore, when the applied voltage levels are symmetric with respect to flat band, the background frequency shift is constant during the periodic applied shuttling waveform. Under this condition, the only frequency shift detected is due to the shuttled charge. The closest-approach tip-sample gap is also modulated sinusoidally with a height modulation of 3 nm at exactly twice the electron shuttling voltage frequency (600 Hz). Under this condition, the voltage applied to the sample alternates sign each time the tip moves into tunneling range. This provides the conditions for an electron to shuttle between the tip and state each time the gap modulation brings the tip within tunneling range.

When an electron tunnels to or from a trap state at the sample surface, it alters the local electrostatic surface potential of the sample. The oscillating AFM probe experiences a shift in resonance frequency associated with the modified charge at the surface [14]. This frequency shift is detected by an FM demodulator. The shift induced by a single electron (a few Hz) is readily detectable at room temperature under appropriate conditions. The effect of the electron shuttling produces a frequency modulated signal that is detectable by a lock-in amplifier at 300 Hz (the electron shuttling frequency). The

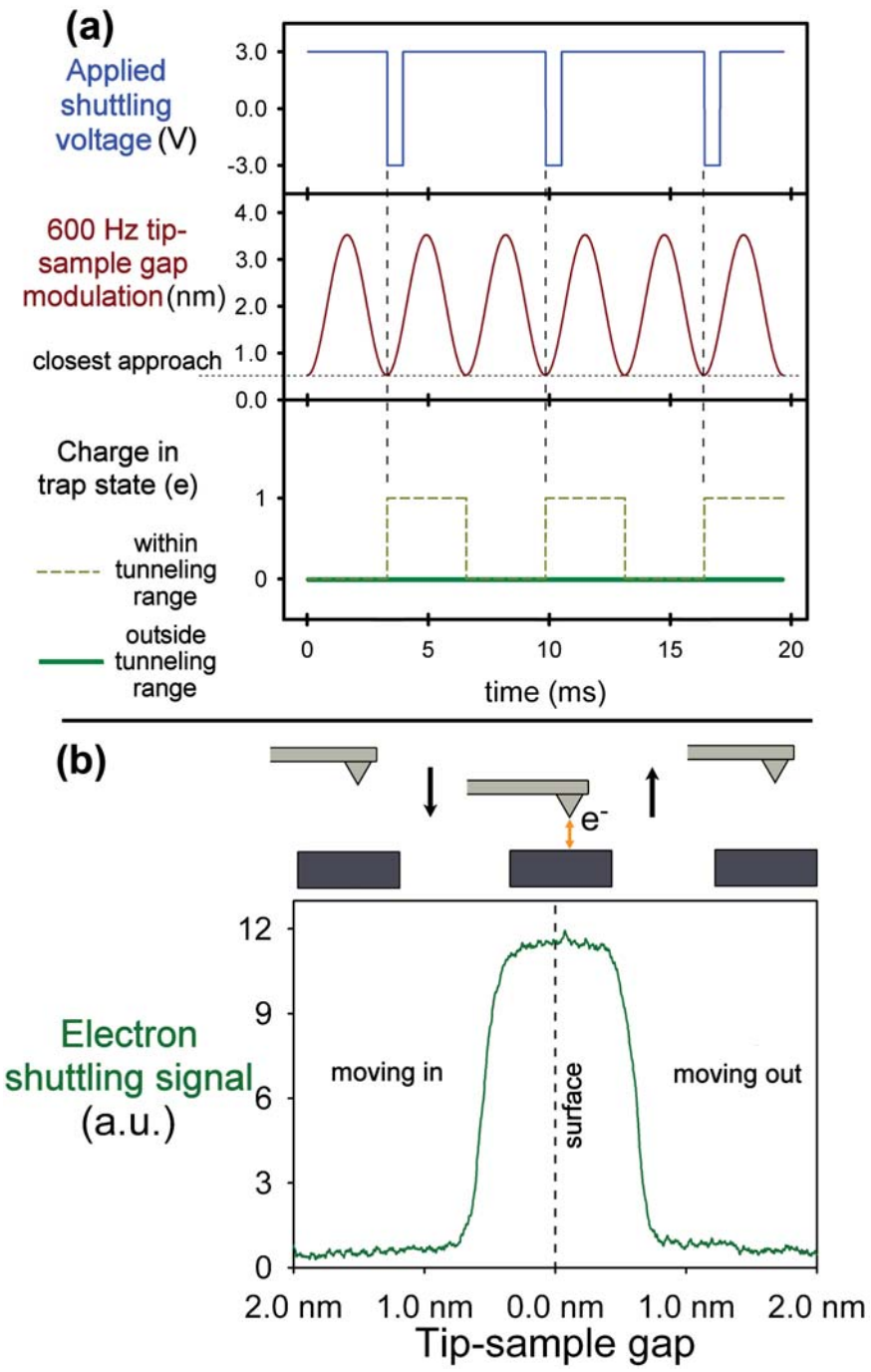

Figure 2.2. Electron shuttling waveforms and signal. (a) Time relationship between the applied 300 Hz shuttling voltage, the 600 Hz tip-sample gap modulation, and charge in the state for DTFM measurements. (b) Actual electron shuttling signal (DTFM signal) obtained by scanning the tip toward a hafnium silicate surface and then away from the surface. The electron shuttling signal is the lock-in amplifier detected frequency modulation (at 300 Hz) caused by the shuttling charge. The signal increases when electrons begin to shuttle between tip and sample. The tip movement is illustrated schematically above the plot.

phase of the shuttling voltage waveform is adjusted so that the initial edge of the negative voltage pulse appears just as the tip height modulation brings the tip to its closest approach, as shown in Figure 2.2(a). This causes the signal due to the shuttled electron to be 90 degrees out of phase with a background signal that is proportional to the local surface potential. Variations in this background surface potential signal, caused by static charge variations in the surface, can thus be separated from the electron shuttling signal by phase sensitive detection, because they are 90 degrees out of phase with the electron shuttling signal.

As a demonstration of the dynamic tunneling method, an oscillating tip is situated over a trap state in a dielectric film at a single location, and the tip is slowly scanned directly toward the surface. The data are shown in Figure 2.2(b). Initially, the tip is out of dynamic tunneling range, and the lock-in amplifier (DTFM) signal is near zero. When the tip is close enough to allow consistent shuttling of an electron to the trap state, the lock-in amplifier signal rises. After an initial rise, the dynamic tunneling signal saturates, because there are no new states to which electrons can tunnel.

To form a DTFM image, the tip is raster scanned at a constant height (no height feedback) over the surface, while the lock-in amplifier (DTFM) signal is recorded at each point, producing a two-dimensional image proportional to the electron shuttling signal. The lock-in amplifier time constant is typically set to 10-30 milliseconds, with a typical image acquisition time of 3 minutes.

The exponential decay of the tip and trap state wave functions in the gap (classically forbidden region) gives rise to the exponential dependence of the tunneling rate on the tip-sample gap, as is observed in STM experiments. For typical tunneling

barrier heights, the tunneling probability drops off by an order of magnitude for each 0.1 nanometer increase in the tip/sample gap. Theoretical calculations have been performed to estimate the electron tunneling rate between a metallic probe tip and a trap state (represented by a three-dimensional spherical potential well), as a function of tip/sample gap, state energy and depth in the dielectric surface [20]. These calculations are consistent with the typical tunneling gaps observed in our previous single electron tunneling measurements [15]. In DTFM measurements, the typical vacuum gap at which dynamic tunneling is first observed (at a 300 Hz shuttling rate) for dielectrics (hafnium silicate and silicon dioxide) is ~0.6 nm.

A DTFM image of a 4.7 nm thick hafnium silicate film (a high-k dielectric) is shown in Figure 2.3(a) (left). The sample was fabricated by growing a 0.7 nm layer of SiO_2 on a silicon substrate, followed by a 4.0 nm layer of hafnium silicate, $Hf_xSi_{1-x}O_2$ (with x=0.6) [21]. The hafnium silicate sample is heated to 300°C for 30 minutes in vacuum prior to imaging, to remove surface contamination The image shows multiple, isolated point-like trap states, randomly distributed near the surface.

The shuttling signal displayed in the image is proportional to the amount of shuttled charge at each location. It is observed that the magnitude of the shuttling signal varies from state to state. For all states which accept only 1 electron at the shuttling voltage range applied (single electron states) and that are near the surface (easily within tunneling range, i.e., with tunneling probability approximately 1 in the measurement time), the magnitude of the shuttling signal is expected to be the same. For single electron states that are deeper in the surface, and near the threshold for tunneling (tunneling probability less than 1 but greater than 0), the magnitude of the shuttling signal is

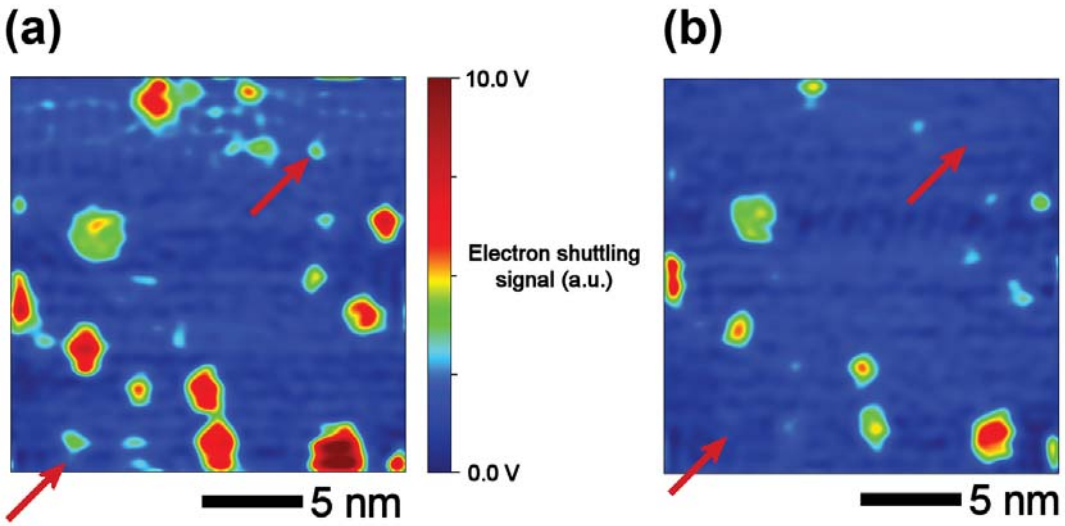

Figure 2.3. Imaging of electronic trap states in hafnium silicate. Two consecutive 20-nm by 20-nm scans of the same area of a 4.7 nm thick HfSiOx film on silicon. The arrows point to states which appear in image a (smaller tunneling gap) that are not present in image b (larger tunneling gap).

expected to be smaller than for those states nearer the surface. This explains the variations in the shuttling signal magnitude in the image.

A second feature is also observable in the images. The lateral size of the states varies from state to state. This effect is also related to the depth of the states. When the probe tip is very near a particular state, it can be moved laterally a relatively large distance before the shuttling signal is lost, because tunneling can occur from probe tip regions up further from the tip apex. When a state is deep within the surface (just barely within tunneling range), a slight lateral displacement will take it out of tunneling range. Therefore, states near the surface have an apparent lateral image size which is larger than states which are deeper in the surface. As seen in Figure 2.3, the states with the smallest lateral dimension also have the smallest magnitude of the shuttling signal. Exceptions to this rule are likely explained by clusters of states.

The image, seen in Figure 2.3(b) is acquired at the same location as in Figure 2.3(a), but at an increased tip/sample gap (nominally ~0.1 nm). The image shows the same states as seen in 3a, but the states have a slightly smaller lateral size, as expected. At least 2 states (see arrows) have disappeared from the image relative to Figure 2.3(a), indicating that these states are out of tunneling range due to the increased tip/sample gap. This pair of images illustrates the true three-dimensional atomic scale spatial resolution of this approach. Similar dynamic tunneling images have been obtained on silicon dioxide films, with the same repeatability and spatial resolution. See Figure 2.4. Some of the states in DTFM images have a measured spatial extent of 0.5 nm (FWHM).

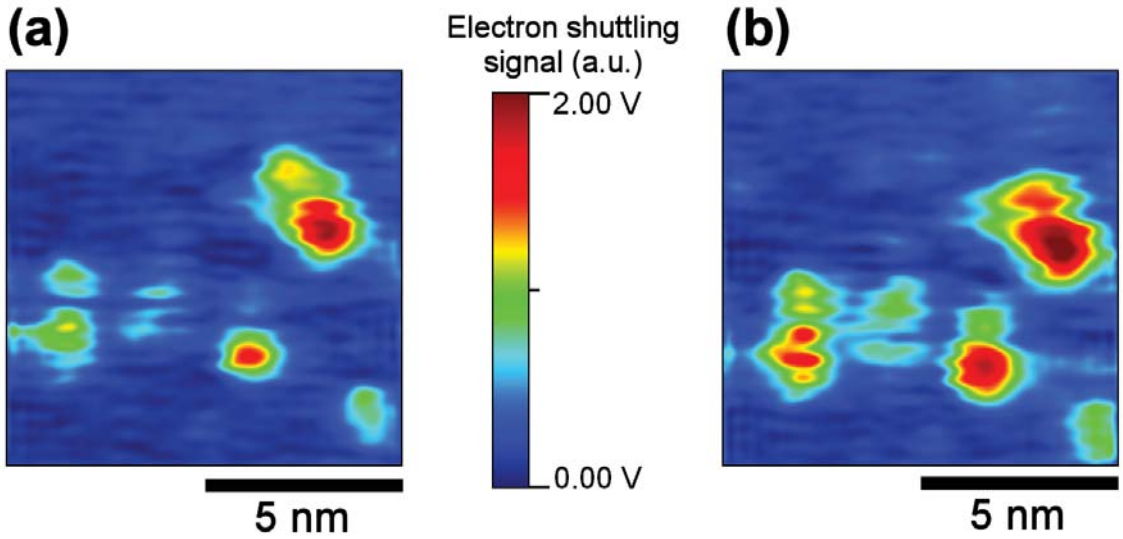

Figure 2.4. Imaging of electronic trap states in SiO_2. (a) 10-nm by 10-nm DTFM scan of a 20 nm thick SiO_2 film on silicon. Resolution is about 0.5 nm. (b) Repeat scan of the same area demonstrating the repeatability of this technique.

The spatial resolution achieved is limited by the atomic scale structure of the tip (as in STM) and the height of the probe tip above the surface. Vertical drift must be low (0.1 nm / minute) in order to achieve high quality images. For the images in Figure 2.3, the lock-in amplifier time constant was set to 10 milliseconds. Both images were acquired as 128x128 pixel images. A circular digital FFT filter was then applied, with a cutoff frequency of 27% of the maximum image frequency, and then each image was linearly interpolated to 512x512 pixels. The images in Figure 2.4 had the same processing steps applied, but the lock-in amplifier time constant was 30 milliseconds.

Dynamic Tunneling Force Spectroscopy (DTFS) measurements have been performed on two nearby states (separated by 5 nm) in the hafnium silicate film. To perform these measurements, the slow scan (y-direction) is disabled and the tip is scanned repeatedly over a single line containing the two states (see Figure 2.5). By varying the magnitude of the pulse voltage in the applied voltage waveform, the energy range, by which dynamic electron shuttling occurs, can be adjusted. The dynamic tunneling signal is recorded for four different shuttling energy ranges (shown in the four line scan data sets in Figure 2.5). To determine the shuttling energy range, the applied voltage must be scaled, since part of the applied voltage is dropped across the dielectric film, and part is dropped between the tip and the trap state [18]. It is observed in Figure 2.5 that electrons are shuttled to both states when the shuttling energy range is 1.7 eV to -1.7 eV. However, when the shuttling range becomes 1.7 eV to -1.1 eV, the shuttling signal from the state on the right disappears, while the signal from the left state remains. These data show that the two states have different energies, which can be differentiated spectroscopically by DTFS.

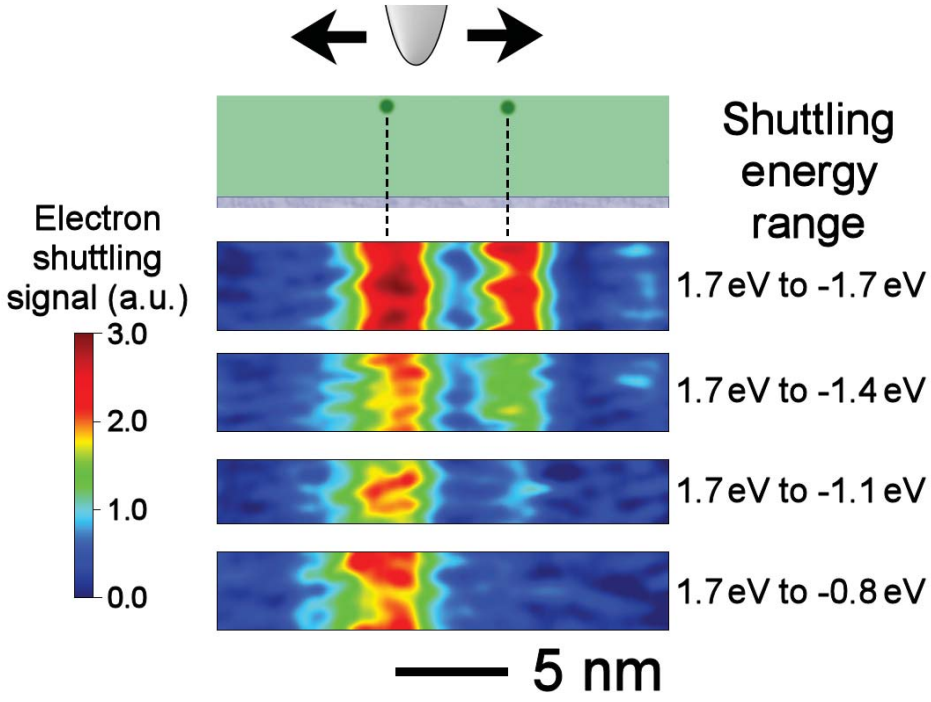

Figure 2.5. Spectroscopic energy measurement of two different states. In this experiment the y scan is disabled so that the tip scans repeatedly over two states during the spectroscopic data acquisition. The four sets of data show the electron shuttling signal (colour scale shown at far left) at different shuttling energy ranges (shown on the right). As the shuttling energy range is decreased, shuttling to the state on the right state stops, while it continues to the left state. These data indicate that the energy of the state on the right is closer to the valance band than the state on the left. When the shuttling energy range is restored to 1.7 eV to -1.7 eV, shuttling to both states resumes.

While the chemical identity of the states being imaged by dynamic tunneling cannot be verified at this time, they are not likely to be $HfSiOx/SiO_2$ interface states (at a depth of 4.0 nm), since the probability of tunneling to midgap states at the $HfSiOx/SiO_2$ interface has been calculated to be small, using the previously published analysis [20]. The disappearance of some states at increased tunneling gap shows that the states are not all at the surface either, since they are observed to be at different depths (see Figure 2.3). This disappearance cannot be attributed to a tunneling energy condition, since an increased tunneling gap actually increases the range of accessible energies available for tunneling (increased gap causes the portion of the applied voltage dropped in the tip/sample gap to increase), resulting in an increased movement of the tip fermi level relative to states in the surface due to the applied shuttling voltage. This means that in Figure 2.3(b), the states disappear only because they are out of tunneling range. A method to independently determine state energy and depth is being currently explored.

DTFS measurement of the energy of these states may eventually provide a means of determining their chemical identity. Recent theoretical calculations have predicted the energy of several types of trap states at the surface of silicon dioxide [22]. Such energy calculations, when compared with DTFS measurements, could provide a basis for providing a unique chemical identification. It is important to note that in previous tunneling measurements [18], it has been shown that the energy resolution of the tunneling measurement is limited only by the thermal energy k_BT (~25 meV) at room temperature. At low temperature (5K), this resolution should improve to less than 0.5 meV. Energy measurements at this temperature could provide a powerful means to help determine state identity and also probe the local physical environment of the trap state.

In summary, our results demonstrate the successful extension of STM-like imaging and spectroscopy capabilities to trap states in completely nonconducting surfaces. Trap states in SiO_2 and hafnium silicate films have been imaged with sub-nanometer spatial resolution, and dynamic tunneling spectroscopic measurements have been demonstrated. These measurements point toward other interesting possibilities, including atomic scale investigations of midgap states in wide band gap semiconductors and other dielectric materials such as diamond. Also of interest is the imaging of electronic states in molecules, nanoclusters, and other nanostructures which sit upon completely nonconducting substrates. The combined imaging and spectroscopic power of this method should provide new insight into the electronic properties of many atomic scale systems, previously inaccessible to the STM.

2.3 Acknowledgements

We thank S. Zafar (IBM T.J. Watson Research Center) for providing the hafnium silicate samples. We acknowledge financial support for this project from the Air Force Office of Scientific Research (Grant #FA9550-06-1-0100) and the Semiconductor Research Corporation.

2.4 References

[1] Robertson, J 2006 *Rep. Prog. Phys.* **69** 327

[2] Kochanski G P 1989 *Phys. Rev. Lett.* **10** 2285

[3] Stranick S J, Weiss P S, Parikh A N, and Allara D L 1993 *J. Vac. Sci. Technol. A* **11** 739

[4] Welland M E and Koch R H 1986 *Appl. Phys. Lett.* **48** 724

[5] Kaczer B, Meng Z and Pelz J P 1996 *Phys. Rev. Lett.* **77** 91

[6] Martin Y, Abraham D W and Wickramasinghe H K 1988 *Appl. Phys. Lett.* **52** 1103

[7] Terris B D, Stern J E, Rugar D, Mamin H J 1989 *Phys. Rev. Lett.* **63** 2669

[8] Schonenberger C and Alvarado S F 1990 *Phys. Rev. Lett*. **65** 3162

[9] Ludeke R and Cartier E 2001 *Appl. Phys. Lett.* **78** 3998

[10] Zhu J, Brink M and McEuen P L 2005 *Appl. Phys. Lett.* **87** 242102

[11] Barth C and Henry C 2008 *Phys. Rev. Lett.*, **100** 096101

[12] Naitou Y, Arimura H, Kitano N, Horie S, Minami T, Kosuda M, Ogiso H, Hosoi T, Shimura T and Watanabe H 2008 *Appl. Phys. Lett.*, **92** 012112

[13] Klein L J and Williams C C 2002 *Appl. Phys. Lett.* 81 4589

[14] Bussmann E, Kim D J and Williams C C 2004 *Appl. Phys. Lett.* **85** 2538

[15] Bussmann E B, Zheng N and Williams C C 2005 *Appl. Phys. Lett.* **86** 163109

[16] Dâna A and Yamamoto Y 2005 *Nanotech.*, **16** S125

[17] Stomp R, Miyahara Y, Schaer S, Sun Q, Guo H, Grutter P, Studenikin S, Poole P and Sachrajda A 2005 *Phys. Rev. Lett.* **94** 056802

[18] Bussmann E and Williams C C 2006 *Appl. Phys. Lett.* **88** 263108

[19] Bussmann E B, Zheng N and Williams C C 2006 *Nano Lett.* **6** 2577

[20] Zheng N, Williams C C, Mishchenko E G and Bussmann E 2007 *J. Appl. Phys.* **101** 093702

[21] HfSiOx sample supplied by Sufi Zafar, IBM T. J. Watson Research Center

[22] Giordano L, Sushko P V, Pacchioni G, and Shluger A L 2007 *Phys. Rev. Lett.* **99** 136801

CHAPTER 3

SINGLE ELECTRON TUNNELING FORCE SPECTROSCOPY OF AU MONOLAYER PROTECTED CLUSTERS

This chapter contains a paper accepted for publication by the journal Nanotechnology (copyright IOP Publishing, ltd. iopscience.org/nano) entitled *Electronic characterization of individual monolayer-protected Au clusters by single electron tunneling force spectroscopy* by Ning Zheng, Jon Paul Johnson, Clayton C. Williams and Gangli Wang.

This is the first time spectroscopic characterization of electronic states by Single Electron Tunneling Force Spectroscopy (SETFS) has been directly compared with results obtained by a standard spectroscopic technique. The Au Monolayer Protected Clusters (MPCs) exhibit interesting phenomena such as quantum confinement effects and have an electronic energy structure that depends on particle size. The MPC spectra characterized by SETFS are compared with electrochemical data.

The division of work for the results of this paper was approximately as follows: MPC samples and surfaces were prepared by G Wang; the SETFS data acquisition and processing were shared approximately equally between N Zheng and J. Johnson; and the

writing and revision of the paper was divided approximately as G Wang 20%, N Zheng 20%, C Williams 30%, and J Johnson 30%.

3.1 Abstract

Gold Monolayer Protected Clusters (MPCs) exhibit strong quantum confinement effects and size dependent electronic, optical and chemical properties. Chemical tuning of these properties can be achieved by established synthesis methods, providing an excellent system for the study of the relationship between chemical and electronic structure. In this letter, the first electronic spectra of individual Au MPCs (Au_{25}) acquired by Single Electron Tunneling Force Spectroscopy on nonconducting silicon dioxide surfaces are reported. A HOMO-LUMO energy gap is observed in the Au_{25} spectra. Hysteretic charging of the particles is also observed while obtaining the energy spectra. The new single electron tunneling measurement methodology is described. A model explaining the measurements supports the existence of mid HOMO-LUMO gap defect states.

3.2 Introduction

Since the seminal two-phase synthesis route reported by Brust et al. [1], Au MPCs with 1-5 nm core diameter and various thiolate monolayers have served as a prototype system for fundamental studies [2-4]. With tunable electronic properties and excellent stability and structural functionality, Au MPCs are promising candidates for applications in solar energy conversion, catalysis, and biomedicine [5-7]. As Au MPC properties are strongly correlated with size, extensive efforts have been made to obtain mono-disperse materials [8-10]. Recently, the crystal structure of individual Au MPCs with atomic scale

resolution has been resolved by X-ray crystallography and compared with theoretical calculations [11-14]. A new S-Au-S model has been identified (the 'staple' thiol binding motif), which could impact the current understanding of MPC electronic structure and ligand exchange [15-19].

Previously, electrochemical measurements of both large and small Au MPCs have been performed. In larger MPCs, the gold cluster represents a nanosized capacitor surrounded by a ligand dielectric layer. The voltammograms (cyclic voltammogram, CV and differential pulse voltammogram, DPV) of larger Au MPCs (with ~140-atom cores) passivated with a hexanethiolate monolayer (referred to as $Au_{140}C6_{53}$) show redox-like continuous charging peaks in electrochemical measurements in solution [20, 21]. Each well-resolved charging peak shown in the CV or DPV corresponds to one electron transfer between the MPCs and the working electrode. A concentric spherical model has been used to describe the charging behavior [22]. Improved agreement with experimental results was achieved by taking into account ion and solvent penetration using the Poisson-Boltzmann equation [23]. The electrochemical charging spectrum is similar to tunneling measurements performed with the Scanning Tunneling Microscope [24].

In small MPCs, molecule-like charging behavior has been observed. In these clusters, an opening of a HOMO-LUMO energy gap arises. The transition from bulk-to-molecule electronic structure has been observed in voltammetric and near-IR absorbance studies of alkanethiolate-coated Au monolayer-protected clusters (MPCs) with Au core masses of 8 to 38 kDa [25]. Initially attributed to be Au_{38} [26, 27] and later established as $Au_{25}^{-}N(C_8H_{17})_4^{+}$, an electrochemical gap of 1.60-1.69 eV has been observed [12, 14, 28]. Using a slightly different synthetic route, other small clusters were also prepared with

hexanethiolate ligands [29, 30]. With mass spectrometry, these synthesized MPCs, measured to be Au_{38} and Au_{11} by mass spectrometry, were shown to have electrochemical gaps of 1.2 eV and 1.9 eV, respectively [29].

UV-Visible-Near IR absorbance of Au MPCs also displays size dependent energy gaps and electronic transitions [25]. Spectra of Au_{25} MPCs display several absorption bands attributed to hybrid orbitals of Au and S atomic states [9, 31, 32]. With the experimental discovery of the novel S-Au-S bonding [11, 12, 14], optimized theoretical descriptions of Au_{25} MPC electronic structures have found excellent agreement with experimental results [13, 14]. Density Functional Theory calculations predict that MPC energetics are weakly dependent on alkyl chain length but vary significantly with respect to ligand structure and polarity [33, 34]. Chirality changes induced by ligand exchange reactions demonstrate the influence of thiol ligands on the electronic structure and properties of Au MPCs using circular dichroism [35]. Near-IR luminescence from various Au MPCs with different core size and ligands has been observed [36, 37]. The broad emission at a common energy with a wide range of quantum efficiency leads to speculation about a metal-atom-based or surface-defect-related luminescence mechanism [38-40]. Energy relaxation between the excitation and emission (generally > 1eV) and weak correlation with the absorbance features support the argument but the origin of the states has not been identified.

Pseudopotential and tight-binding methods have been used to calculate the energy levels and many-body excitation spectra of a number of nanocrystals [41-44]. Energy spectra of semiconductor and metal quantum dots and MPCs have been measured by optical [45-47], electrochemical [20, 27] and Scanning Tunneling Spectroscopy (STS)

[48-55]. While each approach has its unique capabilities, it is difficult to separately investigate electron and hole energy levels by optical spectroscopy, as it inherently involves transitions between two levels. Electrochemical methods provide a direct means to obtain electronic spectra on MPCs. However, the measurements reflect only the average properties of MPCs. Electrochemical measurements tend to average out non-uniform electronic structure (heterogeneity) within the samples. In addition, the origin of the background current in CV, either at the valley between the peaks or the sloping at higher applied potential, has been attributed to the polydispersity of the sample. Scanning Tunneling Spectroscopy (STS) [51, 55] is particularly suitable for providing information on the local DOS on individual clusters with subnanometer resolution, but the application of STS is limited to MPCs on conducting substrates. Close proximity to conducting substrates can induce energy level shifts in the MPC. In single electron tunneling measurements, the tunneling rate is typically 6 orders of magnitude smaller, allowing measurements at an increased tunneling gap (up to 0.6 nm) when compared to STM measurements, significantly reducing the energy level shifts induced in the MPC. It is also difficult to use STS to study internal electron energy relaxation that may occur while the injected electron is still in an MPC (for example, electron relaxation from a LUMO state to a midgap defect state with long dwell time greater than 1 microsecond). When the dwell time is greater than 1 microsecond, not enough current can be detected (< 1 picoampere) to measure the energy relaxation to such a state, since the STS tunneling current occurs through the states and not to the states involved. In contrast to STS, Single Electron Tunneling Force Spectroscopy (SETFS) is capable of injecting/extracting single electrons directly to/from electron states which exist on completely nonconducting

surfaces [56]. With the inherent subnanometer spatial resolution provided by tunneling, SETFS can be applied to investigate individual MPCs sitting upon a dielectric surface, which provides a weak coupling between the states in the cluster and the surface. Recently, force detected single electron tunneling *from conducting substrates* to semiconductor quantum dots [57-59] and MPCs [60] has been reported.

In this paper, we report the measurement of the energy spectra of Au_{25} MPCs using a recently developed surface potential measurement technique [61] and Single Electron Tunneling Force Spectroscopy (SETFS) [56] at room temperature. Since SETFS probes single MPCs, this method could eventually provide quantitative information about the electronic structure of MPCs, which is averaged out by ensemble methods, and direct information about internal electron relaxation processes within the MPC.

3.3 Experimental methodology

Figure 3.1(a) shows a schematic of the experimental apparatus, constructed using a commercial AFM (Omicron Multiprobe S) operated at room temperature and 10^{-8} mbar pressure. The AFM cantilever has a platinum coated tip with a nominal probe radius of less than 35 nm. Au MPCs, with a core of 25 gold atoms, are chemically immobilized on the surface of thermally grown SiO_2 on silicon (p-type, 38-63 Ω·cm), which is modified by silane chemistry (see Background Information). Part of the silane layer has molecules that are terminated with a thiol group, which tether the MPCs to the surface by forming a bond via ligand exchange. Varying the concentration of the thiol-terminated molecules in the silane layer allows for density control of the MPCs.

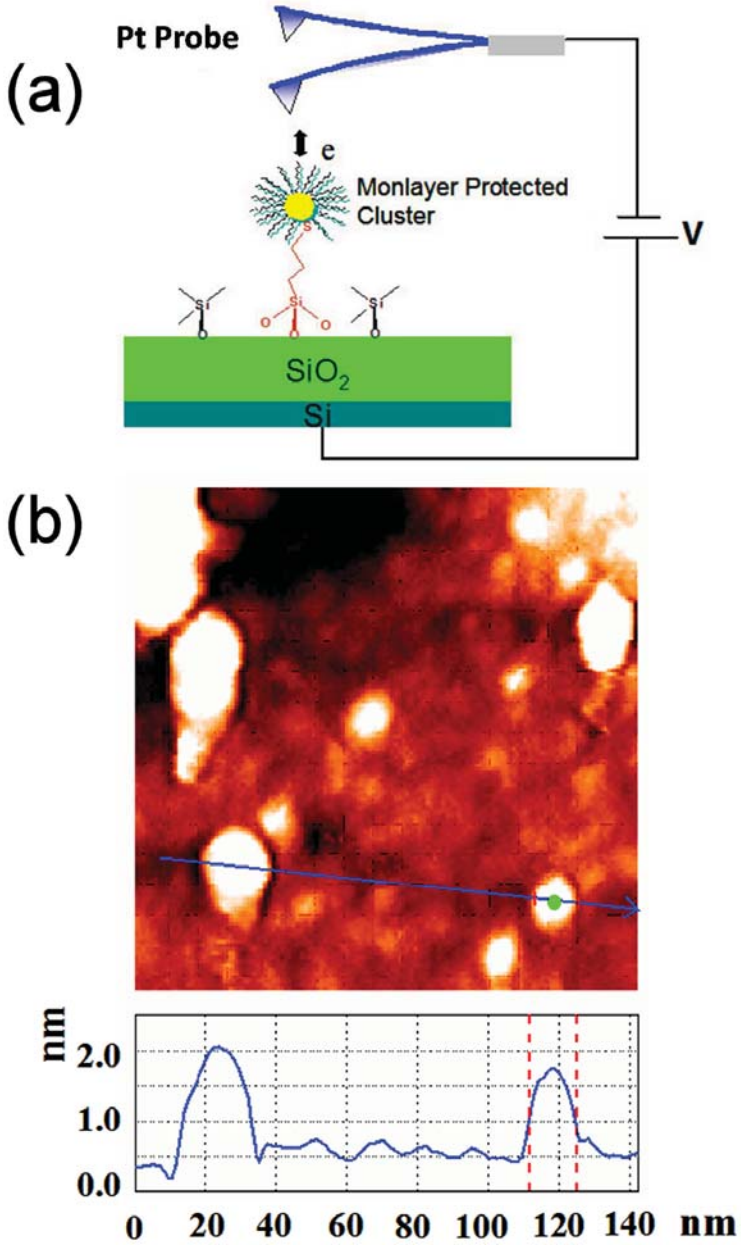

Figure 3.1. Schematic illustration of Single Electron Tunneling Force Spectroscopy (SETFS) and topographic image of Au_{25} MPCs on the SiO_2 surface. (a) Schematic illustration of SETFS. Under typical experiment conditions, the probe is oscillated at its resonance frequency (~250 kHz) and fixed amplitude (30-50 nm) by an external oscillator with a feedback circuit. With a bias applied to the sample, when the apex of the metal-coating probe approaches an individual Au MPC on a nonconducting substrate, single-electron tunneling can occur. The tunneling event is detected by comparing an electrostatic measurement of the surface potential (SP) before and after a tunneling attempt. (b) Topographic image of Au_{25} MPCs on the SiO_2 surface imaged by non-contact AFM. The measured diameter (height of MPC) is typically 1.5 ± 0.4 nm. SETFS is performed with the probe tip directly above a Au MPC.

The nominal diameter of a Au_{25} MPC is 2.35 nm, with a 1 nm core and a ligand monolayer of 0.7 nm thickness [12,14]. Its shape is nearly spherical. In Figure 3.1(b), individual Au_{25} MPCs are observed by Dynamic Force Microscopy, operating with a 50 nm oscillation amplitude and a +5 Hz set point (repulsive contact mode). The Au MPCs are seen scattered on the substrate with measured apparent heights (diameters) of 1.5 ± 0.4 nm. The measured height is likely influenced by the force exerted on the MPC by the AFM probe tip. SETFS measurements are performed by placing the probe directly over a single Au MPC within tunneling range.

The potentiometric method used to perform the spectroscopic measurements is described in a previous paper [61]. The spectrum is acquired with the application of a series of voltage steps, which shift the Fermi level of the probe with respect to the energy levels of the Au MPC and which induce electrons to tunnel between the MPC and the probe. Electrons injected to or extracted from the MPC by tunneling produce a change in the local electrostatic surface potential (SP). To measure the change in SP, the feedback loop is frozen, the tip is withdrawn to a height of 4 nm above the cluster (out of tunneling range), and an ac voltage (85 Hz symmetric square wave around the flatband voltage with a 2V amplitude) is applied between tip and sample to measure the surface potential. An FM detector and lock-in amplifier record the shifts in the AFM probe resonant frequency induced by the electrostatic force gradient on the probe tip [61] at the square wave frequency. The change in this SP signal is proportional to the amount of charge which has tunneled between the probe and Au MPC [61]. Subtraction of the measured SP before and after a tunneling attempt provides an output which shows occasional abrupt changes in the surface potential that can be attributed to electron tunneling between tip and

sample. The applied voltages at which electron tunneling is observed are recorded, as the applied dc voltage is ramped, yielding the tunneling spectrum for the Au MPC.

In this experiment, a LABVIEW program is used to control the magnitude, polarity, and timing of the applied dc voltages and to monitor the tunneling between probe tip and Au MPC. Figure 3.2(a) shows the sequence of tip movements, applied voltages, and surface potential signal for given charging events. In region (1), an AC voltage V_{AC} is applied to record the SP signal. In region (2), the AC voltage is removed, and the probe is brought within tunneling range of the MPC to assure that tunneling can occur. A DC voltage V_{DC} is then applied to induce tunneling. If the energy condition is satisfied, tunneling should occur. The probe stays at this minimum gap distance for 0.4 seconds, and is then withdrawn to its previous height (4.0 nm) where the SP is again measured to determine whether tunneling has occurred. The change in SP measured between (1) and (3) implies a tunneling event in region (2). This process is repeated, each time with a different applied voltage (V_{DC}) to perform the spectroscopic scan. As an example, the lack of change in SP between (3) and (5) indicates that no tunneling has occurred in (4), while the change from (5) to (7) implies another tunneling event in (6).

Figure 3.2(b) shows some raw data from a single SETFS voltage scan on an individual Au_{25} MPC on a 10-nm-thick SiO_2 film. As the figure indicates, when the *applied* dc voltage to the substrate (solid curve in the figure) is stepped between 0V and +3V, raising the Fermi level of the probe with respect to the electronic states of the MPC, no electron tunneling occurs (only noise is observed). At +3.4V, two electrons tunnel to

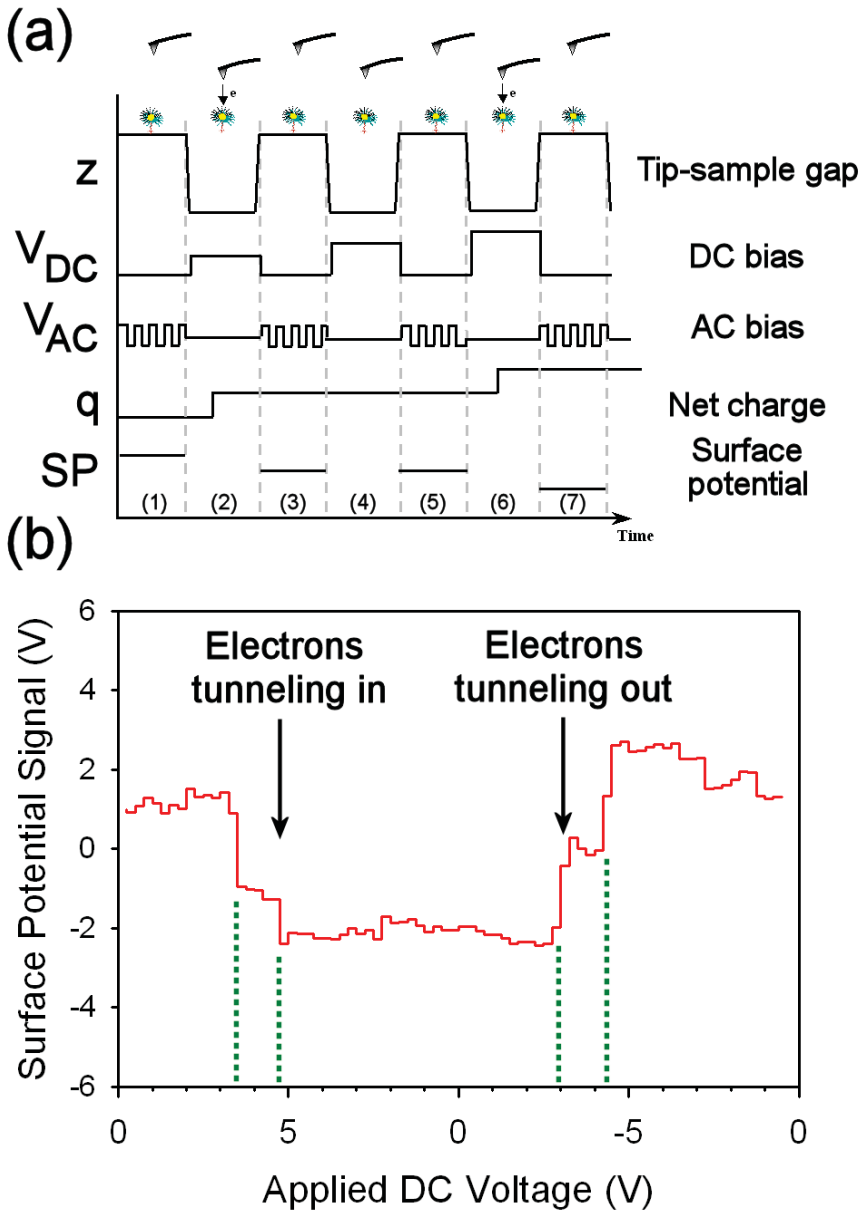

Figure 3.2. Algorithm for measuring the energy spectrum by SETFS and a single surface potential scan on a Au_{25} MPC. (a) The algorithm for measuring the energy spectrum of the Au MPC by SETFS. Z indicates the probe-sample separation, V_{DC} the dc voltage used to induce electron tunneling, V_{AC} the ac voltage used to measure surface potential (SP), and q the net number of electrons in the MPC. SP is the surface potential measurement used to count the tunneling electrons by comparing the potential before and after tunneling attempts. (b) A single SP scan on an Au_{25} MPC. Note that the voltage ramps up from zero to the maximum positive voltage (5V), then down through zero to the maximum negative voltage (-5V), and finally back to zero. The dotted lines point out voltages at which electrons tunnel into or out of the Au MPC. Electrons injected in the MPC during the ramp from 0V to 5V are not removed at the same voltages during the ramp down (5V to 0V). This hysteresis is attributed to relaxation of the electrons to mid-gap states that are inaccessible to direct tunneling from the tip.

the Au_{25} MPC, causing the abrupt change of SP signal. With two extra electrons on the Au_{25} MPC, the surface potential becomes more negative. A single electron tunnels at 4.8V, with an additional reduction in the surface potential of half the magnitude of the first pair of injected electrons. When the dc voltage is ramped back down from 5V to 0V, surprisingly *no tunneling occurs*. As the ramp then continues from 0V to -5V (lowering the Fermi level of the probe below mid-gap), 2 electrons on the MPC tunnel back to the probe at an applied voltage of -2.9V, and two more tunnel at -3.25V. Each pair of returning electrons yield a change in SP signal equal in magnitude but of opposite sign to the change at +3.4V, and twice the value at +4.8V. The hysteresis observed in the measurements will be discussed below.

In order to detect single electron tunneling, the SP change caused by a single electron must be larger than the SP noise caused by background charge fluctuations at the oxide surface. Before measurements are made, the change in the SP signal caused by single electron tunneling is unknown, as it depends upon several factors [62]. Therefore, a screening criterion to identify single and double electron tunneling events in the measured SP signal is helpful. Figure 3.3 shows a histogram of all measured changes in SP signal from 60 scans on three individual Au_{25} MPCs (4800 total measurements of the change in SP). Clear peaks on either side of the center peak of the histogram identify single- and two-electron tunneling events. SP changes of smaller amplitude (peak centered around zero) correspond to noise which is measured in the absence of tunneling. The width of the side peaks is due in part to this background noise in the measurement. Note that there are relatively few two-electron tunneling events compared to single-electron tunneling events. The inset in Figure 3.3 shows part of the histogram, but stretched in the vertical direction to show the side peaks more clearly. A Gaussian curve

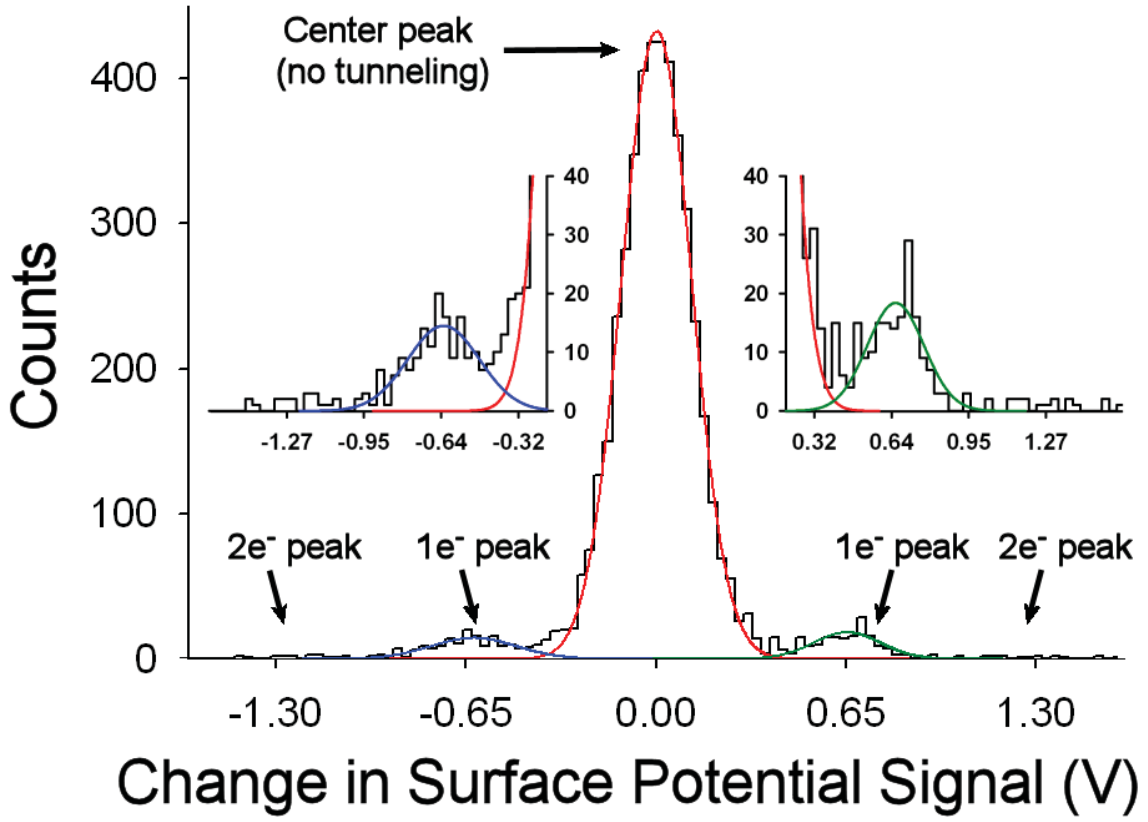

Figure 3.3. Histogram of the changes in surface potential (SP) signal from 20 repeated SETFM scans over three individual Au_{25} MPCs (60 scans total, or 4800 measurements). The large center peak indicates that for most applied voltages, no tunneling occurred. The peaks immediately to either side correspond to single electron tunneling. The smooth curves are Gaussian functions fit to each peak, and the width of the peaks indicates noise in the measurement. Inset: The same histogram rescaled to show the detail near the x axis. Events inside the center peak, i.e., all events between the intersection points of the Gaussian curves, are not included in the SETFS spectra.

is fitted to the center and nearest side peaks. The intersections of the Gaussian curves that are fit to the center and side peaks are used as threshold values for separating real tunneling events from background noise. Only SP changes greater than these threshold values are included in the MPC tunneling spectra. A similar approach is also used to separate single tunneling events from two-electron tunneling events. The final SETFS energy spectrum of the MPC is determined by adding up the number of tunneling events recorded during the voltage scans versus the energy at which the events take place, ignoring those SP changes with magnitudes smaller than the SP threshold value. The spectrum is then normalized by taking the sum of all SP changes greater than threshold at each DC voltage value and dividing by the number of voltage scans and by the SP change that one electron causes (determined by the average SP value of the centers of the two single electron tunneling side peaks). This provides a spectrum that describes the number of electron tunneling events per attempt at each applied voltage.

3.4 Results and discussion

Figure 3.4 contains two unscaled average energy spectra obtained from SETFS measurements on three different Au_{25} MPCs (60 spectroscopic scans total, 20 scans on each MPC). Note that there is no absolute zero in the graph of the spectra, since local charge in the oxide could shift the entire spectrum. These spectra are constructed using only data from 2 of the 4 segments of the full voltage ramp. As discussed above, the full ramp goes from 0 to +5V, +5V to 0, 0 to -5V, -5V to 0. The spectrum shown in Figure 3.4 is taken from the first (0 to +5V) and third (0 to -5V) segments. The reasoning for

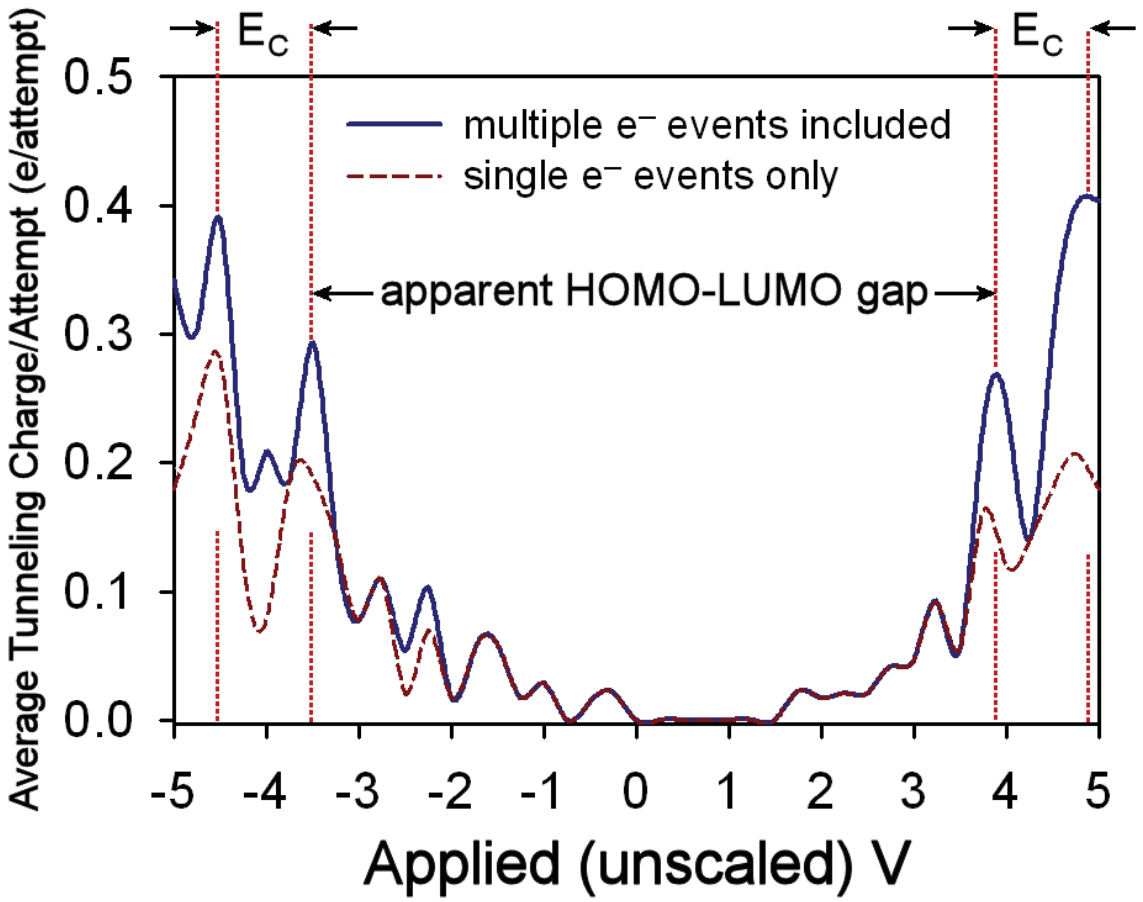

Figure 3.4. Combined tunneling spectra from three individual Au_{25} MPC spectra obtained by SETFS. Note that the applied voltage must be scaled by a factor of approximately 0.177 to correspond to the actual voltage dropped between the probe tip and the MPC gold core. The spectrum shows evidence for a HOMO-LUMO energy gap. On either side of the gap, HOMO and LUMO peaks are separated by a charging energy E_C. The SETFS spectrum in which only single electron tunneling events are included is shown as a dashed line. The solid line represents the SETFS spectrum that includes both single and multiple tunneling events.

choosing these segments is that not much tunneling occurs during the second and forth segments (hysteresis is evident in Figure 3.2b). The red curve represents the Au MPC energy spectrum with only single electron tunneling events included. The blue curve is the MPC energy spectrum if all electron tunneling events greater than the single electron event threshold are included. The single electron tunneling spectrum will be discussed first.

In the single electron tunneling spectrum (red), four major tunneling peaks are observed at applied voltages of −4.5, −3.5, 3.9, and 4.9 V. The peak at 3.9 V represents an electron tunneling into the LUMO level. This extra electron changes the net charge on the MPC, requiring the Fermi level of the probe to be at the energy of the LUMO E_{LUMO} + E_p, the MPC polarization energy [63]. If that electron remains on the MPC, the next electron which tunnels into the LUMO state (which can handle 2 electrons, spin up/spin down), must tunnel at a higher energy $E_{LUMO} + E_p + E_c$, where Ec is the Coulomb charging energy. This peak occurs at 4.9 V. The charging energy thus creates the observed double peak structure associated with the LUMO.

Reversing the direction of the voltage scan eventually induces electron tunneling from the Au MPC back to the probe, but not until the applied voltage is well below the LUMO (in fact, after the voltage becomes negative). This indicates that the electrons injected into the LUMO are no longer available for tunneling back to the probe tip. As the applied voltage is scanned downward, the next large tunneling peak observed is at −3.5 V, which corresponds to the first electron which *tunnels out* of the MPC, this time from the HOMO level. In order for this to occur, the Fermi level of the probe must have an energy of $E_{HOMO} + E_p + E_c$, because the MPC is still charged with the 2 previously

injected electrons. The tunneling peak at −4.5 V corresponds to a second electron removed from the HOMO level, this time with a single additional charge on the MPC, with tip Fermi level at $E_{HOMO} + E_p$.

A physical model is required to explain the observed hysteresis in the SETFS measurements. As Figure 3.2 illustrates, electrons do not tunnel *out* of the LUMO state at energies very near (within a few k_BT) that needed to tunnel *into* the state, in contrast to previous SETFS measurements on an electron trap state in silicon dioxide [64]. This implies that a post-tunneling relaxation has occurred in the MPC measurement. One possible explanation is that an injected LUMO electron relaxes to a midgap state between the HOMO and LUMO levels. Such midgap states may or may not be accessible by direct tunneling to/from the probe tip, depending upon whether they are on the near or the far side of the MPC (relative to the probe tip). Such states have been postulated by researchers trying to explain luminescence from similar MPCs [65, 66]. These states may be defects at the core-ligand interface, and could exist at random locations on the surface of the almost spherical MPC core.

If midgap defect states exist on the measured MPCs or electronic states re-structure after the first electron transfer occurs (inducing a midgap state), the observed spectra obtained by SETFS can be explained as follows. When the first electron tunnels to the LUMO level (3.9 V), the probe Fermi level is near the $E_{LUMO} + E_c$ (charging energy). The injected electron may then relax into a midgap state on the far side of the MPC, leaving the cluster charged. See Figure 3.5(a). After the second LUMO electron tunnels (at $E_{lumo} + E_p + E_c$), it may also relax into a far side midgap state, leaving the MPC doubly charged. When the applied voltage is scanned back from +5V to 0 (the

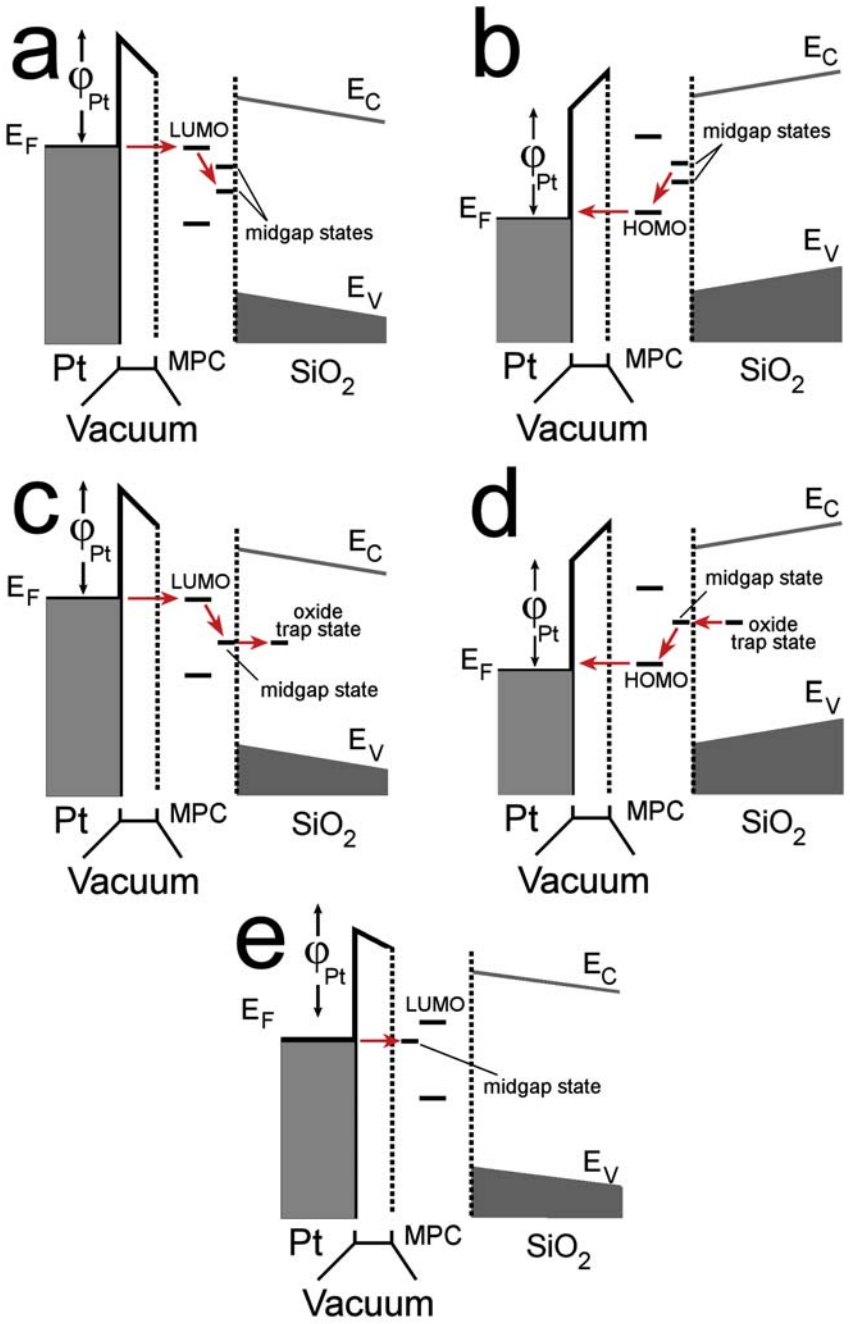

Figure 3.5. Energy diagram illustrating a model to explain the hysteresis and features in the single-electron (a,b,e), multiple-electron (c,d,e) tunneling spectra shown in Figure 3.4. (a) When an electron tunnels into the LUMO, it may relax into a midgap state on the far side of the MPC which is outside of tunneling range. (b) When an electron is later removed from the HOMO, an electron from an occupied midgap state can take its place. (c) If an electronic trap state exists in the oxide beneath the particle, the electron injected into the LUMO may relax to a midgap state and immediately tunnel to such a state, allowing a second electron to tunnel into the LUMO at the same energy as the first injected electron. (d) Similar to case (c) but for extraction from the HOMO level. (e) Direct tunneling to midgap states between the HOMO and LUMO which are located on the tip side of the MPC.

probe Fermi level is lowered w.r.t. the MPC states), the two injected electrons cannot tunnel back to the probe tip, as they reside in far side states, outside of tunneling range (core diameter ~ 1.0 nm). However, when the Fermi level reaches the HOMO level, an electron can tunnel out of the HOMO level (at $E_{HOMO} + E_p + Ec$). The partially empty HOMO level may then be backfilled from the filled midgap states. See Figure 3.5(b). When the probe Fermi level is lowered further by a charging energy, a second electron can then be extracted from the HOMO level, at an energy of $E_{HOMO} + E_p$, leaving the MPC uncharged. The injection/extraction cycle can then be repeated. This model is consistent with the measured single electron SETFS spectrum.

Now, let us consider the SETFS spectrum which includes both single electron tunneling events as well as multiple tunneling events. As can be seen in Figure 3.4, including the multiple tunneling events increases the size of the HOMO and LUMO peaks. This can be explained as follows. If an electron injected into the LUMO level quickly (much less than the tunneling attempt time of 400 ms) drops into a midgap state and tunnels into another nearby electron trap state at the oxide surface, a second electron can tunnel into the empty LUMO at approximately the same energy because the first charge is no longer on the MPC. See Figure 3.5(c). Trap states that can accept an electron are known to exist at the surface of oxides. These states have been imaged and characterized by SETFS [61] and DTFM [67], and often have a density on the order of 15 per $(20nm)^2$. Since a given MPC may not always be near an oxide trap state, it is not always the case that two or more electron tunneling events occur, consistent with the SETFS electron tunneling spectrum. But the fact that there is a significant change in the height of the LUMO peaks in the SETFS spectrum, when multiple tunneling events are

included, requires a physical explanation. This explanation must account for the fact that more than one electron tunnels into the LUMO level (without an additional charging energy). The same picture is also true for the HOMO peak. In that case, a possible explanation for the extra height in the HOMO peaks when multiple tunneling events are included is that there are already filled trap states in the oxide within tunneling range of midgap MPC states. When the probe tip Fermi level is lowered to the HOMO level ($E_{HOMO} + E_p + E_c$), more than one electron can be extracted from the HOMO level, without changing the charge of the MPC. See Figure 3.5(d). In this analysis, it is important to note that if an electron tunnels to the MPC and stays on the MPC in a LUMO or midgap state (no leakage to the oxide surface), it is observed by SETFS as a tunneling event, and it raises the potential of the MPC by one charging energy. If it tunnels to the MPC (LUMO or midgap state) and then tunnels to a nearby oxide trap state, it is still observed as a tunneling event, but the energy of the MPC only changes by a few tens of milli-electron volts, which is an order of magnitude smaller than the charging energy. This is what could allow for occasional multiple tunneling events to occur.

To enable a direct comparison of the SETFS spectrum with previously obtained electrochemical data [27], proper scaling of the SETFS data must take place and the relationship established between the true HOMO-LUMO gap and the apparent energy difference (ΔE_{SETFS}) between the first LUMO level injection ($E_{LUMO} + E_p$) and the first HOMO level extraction ($E_{HOMO} + E_p + E_c$). The relationship is shown below.

$$\Delta E_{SETFS} = (E_{LUMO} + E_p) - (E_{HOMO} + E_p + E_c) = E_{LUMO} - E_{HOMO} - E_c.$$

The true HOMO-LUMO gap ($E_{LUMO} - E_{HOMO}$) from SETFS measurements is therefore given by

$$E_{LUMO} - E_{HOMO} = \Delta E_{SETFS} + E_c.$$

As previously mentioned, an electrochemical study of the energy spectrum of Au_{25} MPCs [27] showed an apparent electrochemical gap energy of 1.62 eV. In electrochemical measurements, the apparent electrochemical gap voltage corresponds to "$E_{LUMO} - E_{HOMO} + E_c$" [63], the difference between the LUMO and HOMO energies plus a charging energy E_c. The electrochemical charging energy was measured to be 0.29eV [27], the separation of the two HOMO peaks. With the charging energy subtracted, the electrochemically measured true HOMO-LUMO gap for the Au_{25} MPC is 1.33 eV [27].

To obtain a correct energy scale in SETFS measurements, the one-dimensional parallel plate model [62] shown below is used to calculate V_{diff}, the voltage dropped between the probe and the core of the Au MPC. This scaling takes into account the fact that the applied voltage moves both the tip Fermi level and the MPC states at different rates. The movement of the tip Fermi level with respect to the electronic states in the MPC is much smaller than the applied voltage. A one-dimensional voltage division model gives

$$V_{diff} = \frac{d + \frac{t_2}{\varepsilon_2}}{d + \frac{t_1}{\varepsilon_1} + \frac{2t_2}{\varepsilon_2}} V_{dc},$$

where d is the minimum tip/MPC vacuum gap, t_1 is the thickness of silicon dioxide, t_2 is the thickness of ligand monolayer on Au core (2 layers), ε_1 is the dielectric constant for silicon dioxide, ε_2 is the dielectric constant for the monolayer surrounding the Au core and V_{dc} is the applied bias voltage.

Before each measurement, the probe tip is lowered until the interaction of the tip and MPC causes the frequency shift of the cantilever (initially negative due to attractive forces) to start to rise (frequency still negative but rising). Note that this frequency shift is much smaller than the +5 Hz frequency set point used to find and image the MPCs, for which the average height was 1.5 +/- 0.4 nm The tip is then pulled back by 0.7 nm from this position, and the SETFS measurements are performed. Due to the unknown stiffness of the ligand layer of the Au MPC, it is difficult to know with high accuracy the vacuum gap used in the SETFM measurement. However, we estimate that during the tip/MPC contact, the ligand layer may be compressed by a couple of tenths of nanometers on each side (top and bottom), before the frequency shift is observed to rise. When the tip is then pulled back by 0.7 nm to perform the SETFS measurements, the estimated vacuum gap would be near 0.3 nm +/- 0.2 nm.

Since the scaling factor for the SETFS energy spectrum depends strongly on the absolute value of the vacuum gap (d), the uncertainty in the absolute vacuum gap makes it impossible to determine with high accuracy the HOMO-LUMO gap based upon the available SETFS data. Here, we show that the scaling is reasonable, by fitting the SETFS HOMO-LUMO gap to known electrochemical data.

If a tip/MPC vacuum gap of d=0.42nm is *assumed*, and with other parameters, t_1=10nm, t_2=0.67nm, ε_1 = 3.9 and ε_2 = 4 [68], the voltage scaling factor is $V_{diff} \approx 0.177$

V_{dc}, and the SETFS measured true HOMO-LUMO gap is 1.33 eV, matching the electrochemical data. Using this same scale factor, the SETFS measured charging energy of the Au_{25} MPC is 0.18 eV. The gap required to achieve this match is within the uncertainty (+/- 0.2 nm) of the experimentally estimated vacuum gap of 0.3 nm, showing that the match is physically reasonable. With additional methodology development to improve the measurement of the absolute vacuum gap, future SETFS measurements may be able to provide an accurate and independent energy scale for measured spectra.

The electrochemical spectrum agrees qualitatively with the SETFS spectrum in the existence of both a HOMO-LUMO gap and an observable charging energy. However, even with the fitting of the HOMO-LUMO gap to electrochemical data, there is a quantitative difference between the SETFS (0.18 eV) and electrochemical (0.29 eV) charging energies. This difference is not currently understood and requires further study. The results presented here represent the first measurements by SETFS on MPCs. Random fluctuations from measurement to measurement were observed on single MPCs, and from MPC to MPC. This variation required that averaging be performed. The origin of these fluctuations may be similar to the spectral diffusion that has been observed in STM measurements [69]. It is also unknown what effect the charging of the MPC core has on the ligand layer.

It is worthy of note that the SETFS data support the previously proposed model that midgap defect states exist between HOMO-LUMO levels on some MPCs [65, 66]. Between the HOMO and LUMO levels seen in the SETFS spectrum, as seen in Figure 3.4, it is apparent that there are a finite number of direct tunneling electron events to such midgap states (those that *are* within tunneling range). See Figure 3.5(e). While this does

not represent conclusive evidence for these states, these observed events are real (above the noise threshold) and must be explained. It must be remembered that these measurements are quite different from previous electrochemical or STM measurements, in that there is no DC current flowing through the MPC. It sits on a completely non-conducting substrate. Most of the electron tunneling that does occur goes directly to existing states on the MPC and remains there, until removed by the probe tip. Electrochemical or STM approaches are not sensitive to the one-time charging of states, which are not electronically coupled to the substrate. Therefore, these states may not show up in these more standard measurements since an appreciable current signal, e.g., pA, requires ~10^7 electrons to be transferred per second. An averaging effect could also wash out the appearance of such states. If MPCs have states at many different midgap energies, the EC spectrum could average them out, providing only baseline current in the midgap energy region [70]. In contrast, the SETFS measurements offer direct experimental access to such midgap states.

3.5 Summary

In summary, Single Electron Tunneling Force Spectroscopy has demonstrated the ability to investigate the electronic structure of Au MPCs on nonconducting surfaces. The energy spectrum of Au_{25} MPCs shows HOMO and LUMO peaks. A strong hysteresis in the charging of the MPCs supports the existence of midgap states. Multiple electron–tunneling events observed in the measurements support the existence of some coupling between the MPC and local electron trap states at the oxide surface. These first spectroscopic measurements on nonconducting surfaces provide a unique measurement

approach to obtaining the electronic structure of individual nanoclusters that are weakly coupled to their support.

3.6 Acknowledgements

This work is funded by the Air Force Office of Scientific Research Grant #FA9550-06-1-0100 and the Semiconductor Research Corporation. Gangli Wang would like to acknowledge Prof. Henry S. White for his support.

3.7 Background Information

Chemicals: Hydrogen tetrachloroaurate trihydrate (HAuCl43H2O), tetraoctylammonium bromide, hexanethiol (C6), 2-Phenylethane thiol (PhC2), sodium borohydride from Sigma-Aldrich, and solvent methanol, acetonitrile, methylene chloride from Fisher, trimethylchlorosilane (TMS) and mercaptopropyltriethoxysilane (MPS) from Gelest Inc. were used as received.

$Au_{25}(SCH_2CH_2Ph)_{18}$ MPCs were synthesized by a modified Brust procedure as reported previously [26, 27] with composition corrected recently [12, 71].

High quality silicon dioxide substrates (10nm oxides) were first rinsed with piranha solution (30 % hydrogen peroxide 70% sulfuric acid) for 5-10 minutes. The substrates were then thoroughly rinsed with water and acetonitrile. To chemically modify the substrates via silane reaction, the cleaned substrate was soaked in a mixture of TMS and MPS (mole ratio of ~20:1) acetonitrile solution for ~ 40 minutes. The thiol groups on MPS molecules provide MPC ligand exchange sites while TMS functions as an inert spacer to control the MPC surface density. Ligand exchange of the MPCs with the

mercapto groups on the substrate was quenched after 10-15 minutes by removal of the MPC methylene chloride solution and extensive solvent wash. Only those MPCs chemically attached to the modified surface can be repeatedly imaged and studied by SETFS. The surface modification ensures individual MPC attachment on the surface without excessive aggregation and with controllable surface coverage as confirmed by morphological imaging.

3.8 References

[1] Brust M, Walker M, Bethell D, Schiffrin D J and Whyman R 1994 *J. Chem. Soc.-Chem. Comm.* **7** 801

[2] Daniel M C and Astruc D 2004 *Chem. Rev.* **104** 293

[3] Murray R W 2008 *Chem. Rev.* **108** 2688

[4] Templeton A C, Wuelfing W P and Murray R W 2000 *Acc. Chem. Res.* **33** 27

[5] Subramanian V, Wolf E E and Kamat P V 2004 *J. Am. Chem. Soc.* ***126*** 4943

[6] Tsunoyama H, Ichikuni N and Tsukuda T 2008 *Langmuir* **24** 11327

[7] Han G, Ghosh P and Rotello V M 2007 *Nanomed* **2** 113

[8] Schaaff T G and Whetten R L 1999 *J. Phys. Chem. B* **103** 9394

[9] Negishi Y, Nobusada K and Tsukuda T 2005 *J. Am. Chem. Soc.* **127** 5261

[10] Jimenez V L, Leopold M C, Mazzitelli C, Jorgenson J W and Murray R W 2003 *Anal. Chem.* **75** 199

[11] Jadzinsky P D, Calero G, Ackerson C J, Bushnell D A and Kornberg R D 2007 *Science* **318** 430

[12] Heaven M W, Dass A, White P S, Holt K M and Murray R W 2008 *J. Am. Chem. Soc.* **130** 3754

[13] Akola J, Walter M, Whetten R L, Hakkinen H and Gronbeck H 2008 *J. Am. Chem. Soc.* **130** 3756

[14] Zhu M, Aikens C M, Hollander F J, Schatz G C and Jin R 2008 *J. Am. Chem. Soc.* **130** 5883

[15] Walter M, Akola J, Lopez-Acevedo O, Jadzinsky P D, Calero G, Ackerson C J, Whetten R L, Gronbeck H and Hakkinen H 2008 *Proc. Nat. Acad. Sci. USA* **105** 9157

[16] Dass A, Stevenson A, Dubay G R, Tracy J B and Murray R W 2008 *J. Am. Chem. Soc.* **130** 5940

[17] Shibu E S, Muhammed M A H, Tsukuda T and Pradeep T 2008 *J. Phys. Chem. C* **112** 12168

[18] Funston A M, Mulvaney P and Murray R W 2009 *Langmuir* **25** 13840

[19] Jiang D.-e, Tiago M L, Luo W and Dai S 2008 *J. Am. Chem. Soc.* **130** 2777

[20] Hicks J F, Miles D T and Murray R W 2002 *J. Am. Chem. Soc.* **124** 13322

[21] Quinn B M, Liljeroth P, Ruiz V, Laaksonen T and Kontturi K 2003 *J. Am. Chem. Soc.* **125** 6644

[22] Hicks J F, Templeton A C, Chen S, Sheran K M, Jasti R, Murray R W, Debord J, Schaaff T G and Whetten R L 1999 *Anal. Chem.* **71** 3703

[23] Garcia-Morales V and Mafe S 2007 *J. Phys. Chem. C* **111** 7242

[24] Sato T and Ahmed H 1997 *Appl. Phys. Lett.* **70** 2759

[25] Chen S, Ingram R S, Hostetler M J, Pietron J J, Murray R W, Schaaff T G, Khoury J T, Alvarez M M and Whetten R L 1998 *Science* **280** 2098

[26] Donkers R L, Lee D and Murray R W 2004 *Langmuir* **20** 1945

[27] Lee D, Donkers R L, Wang G, Harper A S and Murray R W 2004 *J. Am. Chem. Soc.* **126** 6193

[28] Zhu M, Eckenhoff W T, Pintauer T and Jin R 2008 *J. of Phys. Chem. C* **112** 14221

[29] Toikkanen O, Ruiz V, Ronnholm G, Kalkkinen N, Liljeroth P and Quinn B M 2008 *J. Am. Chem. Soc.* **130** 11049

[30] Zhu M, Andersen U N and Jin R 2009 *The Journal of Physical Chemistry A* **113** 4281

[31] Schaaff T G and Whetten R L 2000 *J. Phys. Chem. B* **104** 2630

[32] Price R C and Whetten R L 2005 *J. Am. Chem. Soc.* **127** 13750

[33] Gronbeck H, Walter M and Hakkinen H 2006 *J. Am. Chem. Soc.* **128** 10268

[34] Hakkinen H, Walter M and Gronbeck H 2006 *J. Phys. Chem. B* **110** 9927

[35] Gautier C and Bürgi T 2008 *J. Am. Chem. Soc.* **130** 7077

[36] Link S, Beeby A, FitzGerald S, El-Sayed M A, Schaaff T G and Whetten R L 2002 *J. Phys. Chem. B* **106** 3410

[37] Huang T and Murray R W 2001 *J. Phys. Chem. B* **105** 12498

[38] Wang G, Huang T, Murray R W, Menard L and Nuzzo R G 2005 *J. Am. Chem. Soc.* **127** 812

[39] Wang G, Guo R, Kalyuzhny G, Choi J P and Murray R W 2006 *J. Phys. Chem. B* **110** 20282

[40] Shibu E S, Muhammed M A H, Tsukuda T and Pradeep T 2008 *J. Phys. Chem. C* **112** 12168

[41] Hakkinen H, Barnett R N and Landman U 1999 *Phys. Rev. Lett*. **82** 3264

[42] Xue Y and Ratner M A 2004 *Phys. Rev. B* **70** 115408

[43] Niquet Y M, Delerue C, Allan G and Lannoo M 2002 *Phys. Rev. B* **65** 165334

[44] Zhang H, Yasutake Y, Shichibu Y, Teranishi T and Majima Y 2005 *Phys. Rev. B* **72** 205441

[45] Norris D J, Sacra A, Murray C B and Bawendi M G 1994 *Phys. Rev. Lett.* **72** 2612

[46] Empedocles S A, Norris D J and Bawendi M G 1996 *Phys. Rev. Lett.* **77** 3873

[47] Banin U, Lee J C, Guzelian A A, Kadavanich A V, Alivisatos A P, Jaskolski W, Bryant G W, Efros A L and Rosen M 1998 *J. Chem. Phys.* **109** 2306

[48] Wilkins R, Ben-Jacob E and Jaklevic R C 1989 *Phys. Rev. Lett.* **63** 801

[49] Banin U, Cao Y, Katz D and Millo O 1999 *Nature* **400** 542

[50] Bakkers E P A M, Hens Z, Zunger A, Franceschetti A, Kouwenhoven L P, Gurevich L and Vanmaekelbergh D 2001 *Nano Lett.* **1** 551

[51] Zhang H, Schmid G and Hartmann U 2003 *Nano Lett.* **3** 305

[52] Hou J G, Wang B, Yang J, Wang K, Lu W, Li Z, Wang H, Chen D M and Zhu Q 2003 *Phys. Rev. Lett.* **90** 246803

[53] Naitabdi A, Ono L K and Roldan Cuenya B 2006 *Appl. Phys. Lett.* **89** 043101

[54] Steiner D, Aharoni A, Banin U and Millo O 2006 *Nano Lett.* **6** 2201

[55] Jdira L, Liljeroth P, Stoffels E, Vanmaekelbergh D and Speller S 2006 *Phys. Rev. B* **73** 115305

[56] Bussmann E B, Zheng N and Williams C C 2005 *Appl. Phys. Lett.* **86** 163109

[57] Stomp R, Miyahara Y, Schaer S, Sun Q, Guo H, Grutter P, Studenikin S, Poole P and Sachrajda A 2005 *Phys. Rev. Lett.* **94** 056802

[58] Dâna A and Yamamoto Y 2005 *Nanotech.* **16** S125

[59] Zhu J, Brink M and McEuen P L 2005 *Appl. Phys. Lett.* **87** 242102

[60] Azuma Y, Kanehara M, Teranishi T and Majima Y 2006 *Phys. Rev. Lett.* **96** 016108

[61] Bussmann E B, Zheng N and Williams C C 2006 *Nano Lett.* **6** 2577

[62] Bussmann E, Kim D J and Williams C C 2004 *Appl. Phys. Lett.* **85** 2538

[63] Laaksonen T, Ruiz V, Liljeroth P and Quinn B M 2008 *Chem. Soc. Rev.* 37 1836

[64] Bussmann E and Williams C C 2006 *Appl. Phys. Lett.* **88** 263108

[65] Wang G, Guo R, Kalyuzhny G, Choi J P and Murray R W 2006 *J. Phys. Chem. B* **110** 20282

[66] Wang G, Huang T, Murray R W, Menard L and Nuzzo R G 2005 *J. Am. Chem. Soc.* **127** 812

[67] Johnson J P, Zheng N and Williams C C 2009 *Nanotech.* **20** 055701

[68] Chen S, Murray R W and Feldberg S W 1998 *J. Phys. Chem. B* **102** 9898

[69] Smith R K, Nanayakkara S U, Woehrle G H, Pearl T P, Blake M M, Hutchison J E and Weiss P S 2006 *J. Am. Chem. Soc.* **128** 9267

[70] Bard A J and Faulkner L R 2001 *Electrochemical methods: fundamentals and applications*, *2nd ed,* (New York: Wiley) pp. 87-136, 534-579

[71] Tracy J B, Crowe M C, Parker J F, Hampe O, Fields-Zinna C A, Dass A and Murray R W 2007 *J. Am. Chem. Soc.* **129** 16209

CHAPTER 4

STATE DEPTH AND ENERGY SEPARATION

This chapter contains a manuscript that is prepared for submission entitled *Measurement of depth and energy of buried trap states in dielectric films by Single Electron Tunneling Force Spectroscopy* by Jon Paul Johnson, Dustin W. Winslow and Clayton C. Williams.

After depth dependent tunneling was observed in DTFM images (Chapter 2), this technique was developed to take advantage of the ability to perform Single Electron Tunneling Force Spectroscopy (SETFS) measurements at different probe/sample gaps, providing a means to determine not just the energy of electron trap states in dielectric films, but also their physical depth below the surface. The energy/depth spectrum of trap states in a HfO_2 film is measured.

4.1 Abstract

Electronic trap states in dielectric materials critically influence the reliability and performance of electronic devices. A method to characterize such states with atomic scale spatial resolution is presented. The method is based on tunneling charge measurements, performed at different voltages and tip-sample gaps, and a tunneling model. When combined with previously demonstrated two-dimensional trap state imaging, this method

will provide for three-dimensional imaging of electronic defect states in dielectrics with atomic scale spatial resolution.

4.2 Introduction

Electron traps in gate oxides degrade device performance and reliability by shifting threshold voltage, increasing leakage current and reducing mobility in the channel [1]. Many efforts to characterize electronic trap states in dielectric materials have been made. The approaches include electrical stress measurements [2, 3], Kelvin Probe Force Microscopy [4], conductive Atomic Force Microscopy [5, 6], IV spectroscopy [7], spectrophotometry [8], charge pumping [9], spectroscopic ellipsometry [10, 11], and photoionization [12]. While these measurements provide very useful information about these states, none of them can measure their three-dimensional distribution with atomic scale spatial resolution. This paper describes a method to simultaneously measure the depth and energy of buried trap states.

Single Electron Tunneling Force measurements [13-15], Single Electron Tunneling Force Spectroscopy (SETFS) [16, 17] and Dynamic Tunneling Force Microscopy (DTFM) [18] have been developed to *image* the spatial distribution of individual electron or hole trap states in dielectric films and to measure their relative *energy* [16-18]. These methods are based upon electrostatic force detection of single electron tunneling events between a metallic probe tip and individual trap states in completely nonconducting dielectric films. Atomic scale spatial resolution achieved in these measurements, as in Scanning Tunneling Microscopy (STM), is due to the exponential dependence of the electron tunneling on tip-trap state gap. Most of the

tunneling occurs from a subnanometer region at the apex of the metallic tip. In contrast, Electrostatic Force Spectroscopy (EFS) [19, 20], which also provides electrostatic force detection of single electron tunneling events, *does not provide atomic scale spatial resolution*, because the tunneling occurs *between the substrate and states of interest*. In these measurements, the tip serves only as a force detector. Using the EFS approach, the energy spectrum of localized states in InAs quantum dots [19, 20] and of quantum dots in carbon nanotubes [21] has been investigated.

When electrostatic force is used to detect electron tunneling to/from trap states in a dielectric film, the electric field in the vacuum gap and the dielectric film causes a *depth dependent* shift in the energy of the trap states relative to the tip Fermi level [17, 19]. To extract the true density of states from the tunneling measurements, electrostatic modeling is necessary. Additionally, the depth to which tunneling from the tip can occur in a given measurement time is dependent upon the trap state energy and the tip-sample gap. This letter describes a methodology to simultaneously determine both the depth and the energy of individual trap states in the surface of a dielectric film. The methodology is based upon a series of SETFS measurements performed at different tip-sample heights. These measurements are combined with a tunneling model that includes the dependence of the tunneling probability on trap state depth and energy.

4.3 Theoretical basis for depth and energy determination by tunneling

Single Electron Tunneling Force Spectroscopy makes use of quantum tunneling of electrons between a metal-coated tip and electronic trap states in completely

nonconducting films [16, 17]. The tunneling of electrons requires that two conditions be satisfied. The first is an energy condition. For an electron to elastically tunnel, there must be an available empty (filled) trap state in the dielectric below (above) the Fermi level of the probe tip. The applied voltage shifts the Fermi level of the probe tip relative to the energy levels of trap states in the oxide. The shift of the Fermi level relative to a particular state depends upon many parameters, including the tip-sample gap, the *depth* of the state in the oxide, and the thickness and dielectric constant of the dielectric film. The second condition that must be met is a tunneling probability condition. There must be sufficient overlap of the electronic wave functions of the probe tip and trap state for tunneling to occur. In other words, the tunneling barrier (width and height) must be small enough for tunneling to occur in the measurement time. General calculations have been performed which predict the tunneling rate as a function of the tip-sample gap, energy and depth of the trap state, and the electronic properties of the dielectric [17]. With a typical vacuum-metal work function, the tunneling probability drops off by approximately an order of magnitude per 0.1 nm of vacuum gap. In the dielectric, the drop off of the tunneling probability with depth is typically less rapid than in vacuum, due to the smaller barrier height (the energy difference between the trap state and the conduction band). This means that states nearer the conduction band can be accessed at greater depths in a dielectric film.

The concept of the methodology for independent depth and energy determination is illustrated in Figures 4.1 and 4.2. Figure 4.1 shows an illustrative diagram of the position of four random trap states (above midgap) in depth-energy space. The vertical axis represents the energy of the state in the dielectric film (midgap energy level = 0).

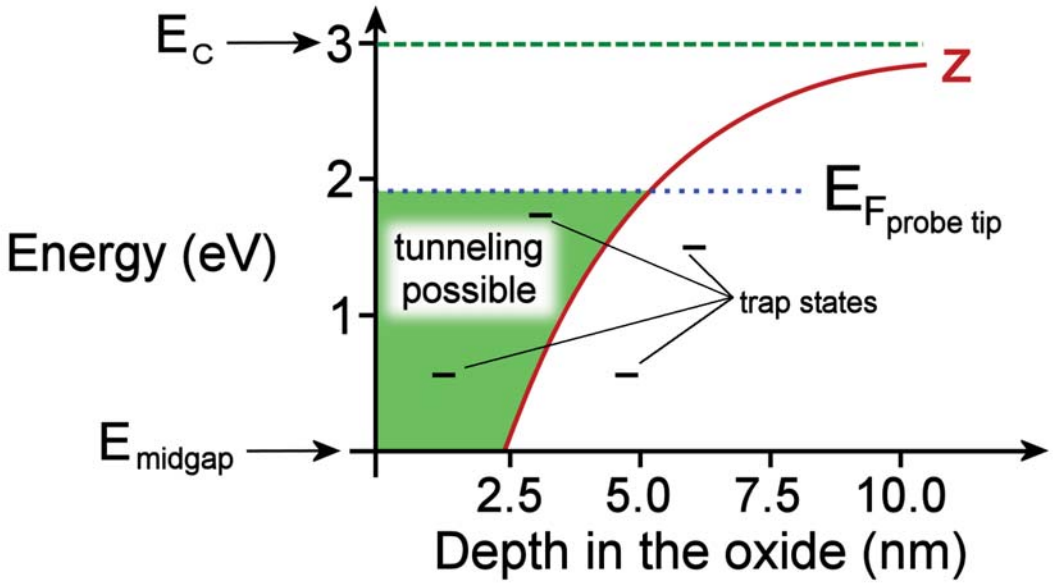

Figure 4.1. Energy-depth diagram illustrating the probability and energy condition for tunneling. To the left of the solid tunneling probability curve, drawn for a given tip-sample gap *z*, the tunneling probability is greater than the minimum tunneling rate (typically 1 electron/second). Beneath the dotted line (representing the probe tip Fermi level), the tunneling energy condition is satisfied for electron injection. The shaded area shows where both the tunneling condition and the energy condition are satisfied. More positive applied voltage to the sample moves the probe Fermi energy (dotted line) upward relative to the trap states, accessing a greater area in energy-depth space. Decreasing the gap (*z*) allows for tunneling deeper in the dielectric film.

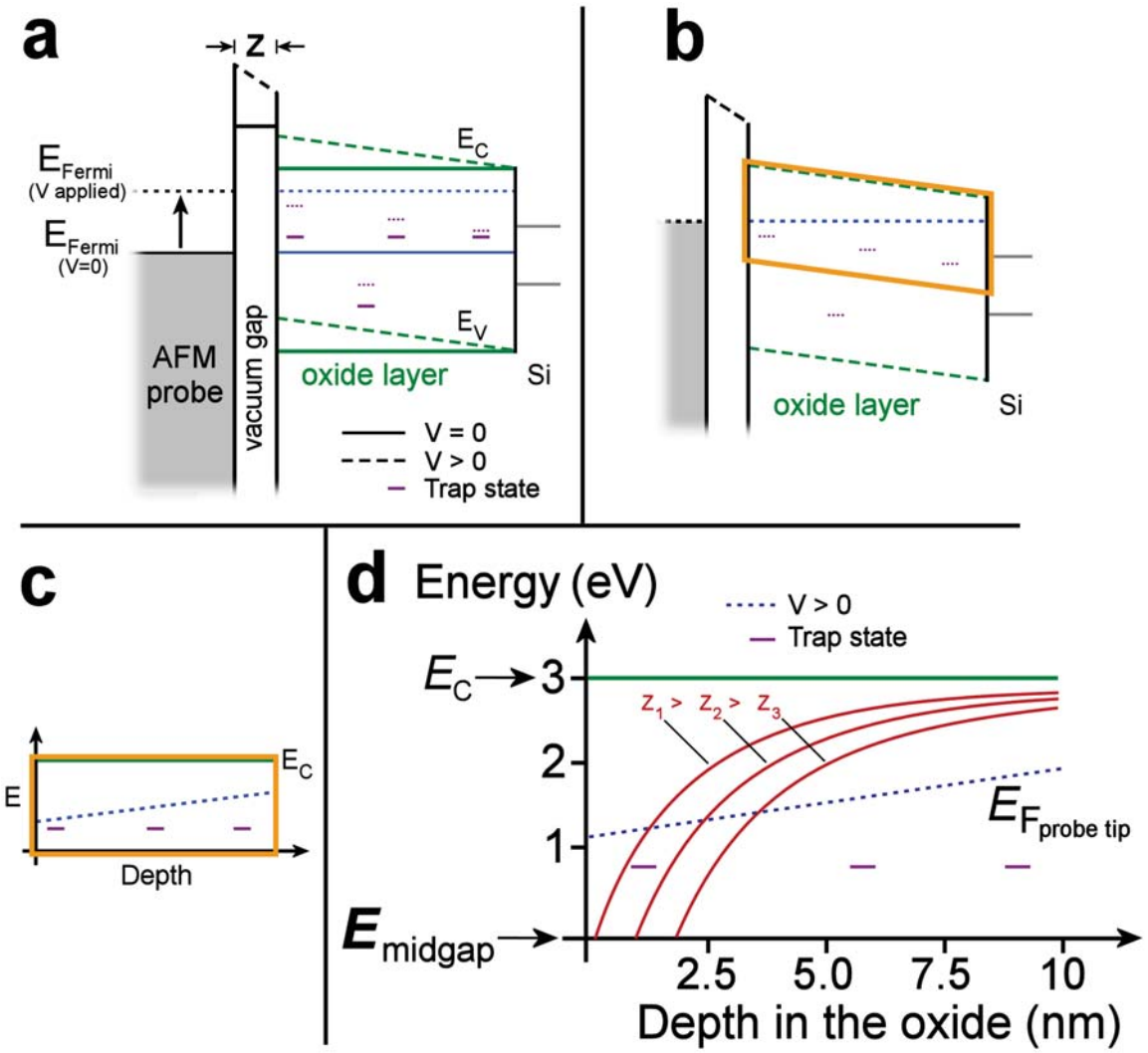

Figure 4.2. Diagrams illustrating the influence of applied voltages on tunneling conditions. **(a)** Energy diagram before (solid) and after (dotted) application of a voltage. **(b)** With an applied voltage, the energy depth space is changed to a trapezoid. The region above midgap is highlighted with a thick solid line. (c) The highlighted trapezoidal region in (b) is remapped to a rectangle. **(d)** A diagram of the oxide layer under an applied voltage, remapped to a rectangle as in (c).

The energy range below midgap is not shown, as the depth-energy analysis is similar whether the state is above or below midgap.

When a tip is placed directly over a particular trap state in a dielectric film, with a tip-sample gap *z* and a voltage V applied between tip and sample, there is a curve on the energy-depth graph (solid in Figure 4.1) that defines the depth to which tunneling can occur in a given measurement time. The shape of the curve arises from the smaller effective barrier height for states nearer the conduction band in the dielectric film. The curve represents a contour of constant tunneling rate (for example, 1 electron/second). This calculation is based upon the tip state wave function decay through two barriers: the vacuum barrier and the barrier in the dielectric film. For the vacuum barrier, the wave function decays as

$$e^{-z\sqrt{\frac{2m_e(E_{vac}-E_s)}{\hbar^2}}},$$

where m_e is the mass of the electron, z is the tip-sample gap, and E_{vac}-E_s is the barrier height—the difference in energy between the vacuum level and the energy of the state in question. In the dielectric film, the wavefunction decays as

$$e^{-d\sqrt{\frac{2m_e^*(E_c-E_s)}{\hbar^2}}},$$

where m_e^* is the effective mass of the electron in the oxide, d is the depth in the dielectric film, and the barrier height is now determined by the difference between the state energy

and the conduction band energy (E_c-E_s). The shaded area corresponds to the region of depth-energy space for which both the energy and tunneling probability conditions are met.

Corrections must be made to the graph in Figure 4.1 to account for the electric field in the gap and sample when a voltage is applied. Figure 4.2 illustrates these effects. The applied voltage modifies the vacuum barrier and bends the bands in the dielectric, shifting the energy of the states relative to the tip Fermi level by an amount which depends upon their physical depth in the film, as shown in Figure 4.2(a). In Figure 4.2(b), the region in depth-energy space above the midgap energy level in the oxide is highlighted. When a voltage is applied, this region becomes trapezoidal, due to the band bending in the oxide. Since the energy difference between the trap states and the conduction band does not change with the applied voltage, the trapezoid can be remapped into a rectangle, which is independent of the applied field. This is shown in Figure 4.2(c). Note that when plotted in this way, the line representing the position of the Fermi level of the probe tip (dotted line) relative to the trap states is no longer horizontal. Also note that the applied field causes a greater shift of the probe Fermi level with respect to deeper states than to states nearer the oxide surface. Figure 4.2(d) combines Figure 4.2(c) with several tunneling probability curves for three different tip-sample gaps (z). The quantitative calculation of both the tunneling probability and the position of the tip Fermi energy relative to states in the film with an applied bias is implemented in a program written in Maple.

4.4 Experimental methods

The experiments are performed in UHV (~10^{-9} Torr) using an Omicron Multiprobe-S AFM/STM. The dielectric sample consists of a 10nm HfO_2 film grown on a 1.5nm-thick interfacial SiO_2 layer on Si, which was rapid thermal annealed at 1000ºC for 5 seconds before measurement. After the anneal, the sample is cleaned in an ultrasonic bath in acetone and then in an ultrasonic bath in IPA, after which it is rinsed in deionized H_2O and blown dry with N_2. After insertion in the vacuum chamber, the sample is heated to 500ºC for 30 minutes to remove organic contamination before imaging.

The following method is employed to measure tunneling charge injected/extracted during the spectroscopic measurements [15, 17]. An oscillating AFM probe tip with a metallic coating (45 nm amplitude, 300 kHz frequency) starts on the surface with standard Dynamic Force Microscopy height control feedback, with a positive set point of 5 Hz (repulsive contact). The feedback loop is then disabled, with the tip on the surface, and the tip is retracted to a height outside of tunneling range (5.4nm). At this height, the local surface potential is measured [15] by applying a square wave (+3/-3V) between the tip and the sample at 318 Hz, while monitoring the cantilever's frequency changes (using an FM detector and lock-in amplifier) at the frequency of the square wave. The square wave voltage is then turned off, and the tip is brought to the desired tunneling gap (initially 0.4 nm) and a stepped voltage ramp is initiated. With the first DC voltage step of the ramp applied, states that are empty and below the Fermi-level of the probe tip are filled by injection from the tip. The tip is then brought back to a height outside of tunneling range (5.4 nm), and the surface potential is measured again. The value of the surface potential change (before and after the tunneling attempt) is proportional to the

amount of charge injected during that voltage ramp step. After the surface potential change is measured, the tip is put back down on the surface under feedback control, before the next data point is taken. This eliminates the effects of vertical drift between the probe tip and sample.

To perform the energy-depth separation measurements, the tip is placed within tunneling range of the sample surface at a location which has at least one trap state. A series of tunneling measurements are performed as a function of applied voltage. The applied voltage is ramped from –5V to 5V in 1V steps, and tunneling charge is measured for each voltage step. The tip-sample gap is then slightly increased (typically by 0.2 nm), and another tunneling charge versus applied voltage curve is acquired. The probe height is increased in steps after each set of tunneling measurements are performed, until the tip is completely out of tunneling range. The recorded tunneling charge data versus tip height and applied voltage is then put into a two-dimensional array, which is then processed to determine the differential tunneling charge associated with each of the individual regions of depth-energy space.

As shown above in Figure 4.1, at a given applied injection voltage and tip-sample gap, the charge which tunnels corresponds to all available empty states in the sample (shaded region) which are below the apparent Fermi level of the tip (dotted line), and within tunneling range (to left of the solid tunneling probability curve). When the probe voltage is increased or the gap decreased, additional states may become accessible to tunneling. To obtain the differential charge injected exclusively into newly accessible states, the charge injected at the previous ramp voltage must be subtracted. The same must be done for previous tip heights. This process is shown in Figure 4.3, using two

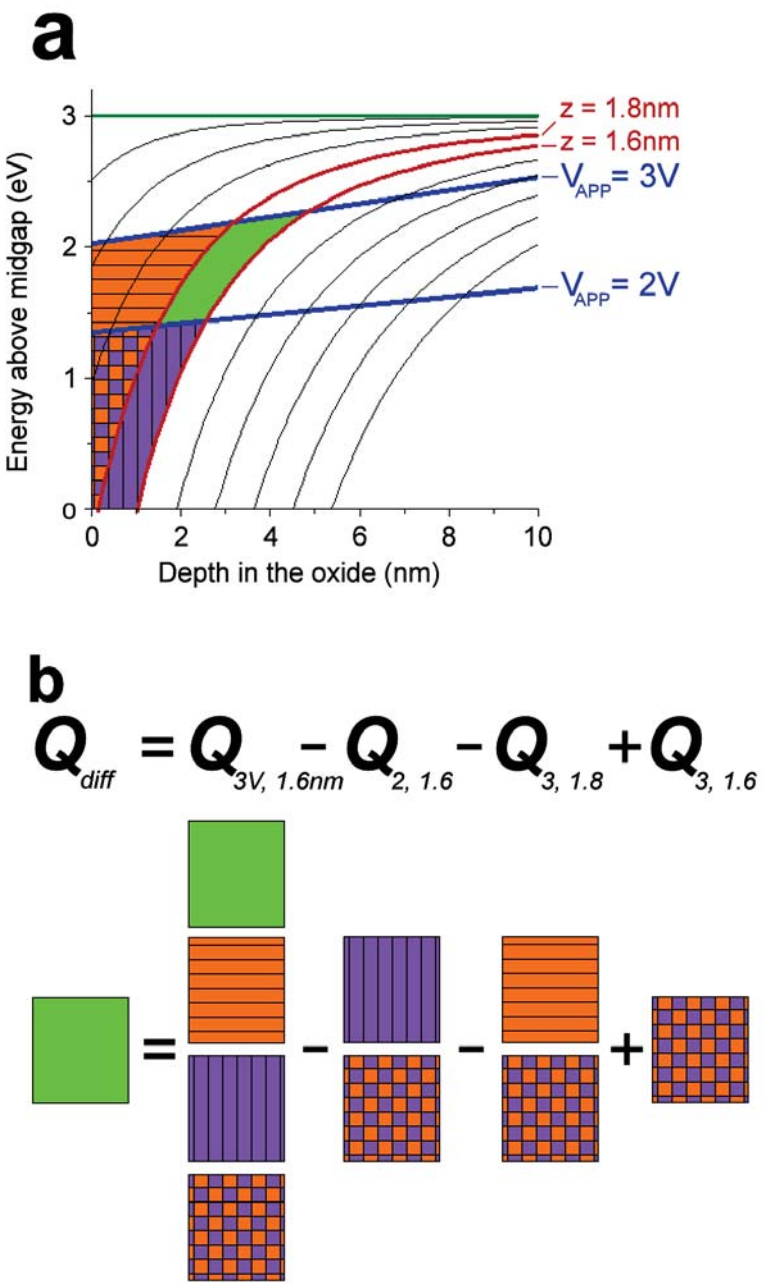

Figure 4.3. Depth-energy separation algorithm using modeled tunneling curves. **(a)** Contours showing the depth of possible tunneling (thin black curves) for certain values of the tip-sample gap *z*, and tip Fermi-level positions as a function of state depth for certain applied voltages V_{app} (labeled V_{app} = 3V, 2V). For a given V_{app} and *z*, tunneling is possible to the left of the *z* curve (labeled z = 1.8nm, 1.6nm) and below the Fermi-level curve. **(b)** To determine the differential charge injected into the area that is shaded solid (no hatchmarks), the charge injection signal measured under the four conditions (two voltages, two heights) is combined according to the expression shown in both algebraic and graphical form.

consecutive applied voltages and tip heights. The differential injected charge is obtained by taking the total injected charge at 3V and 1.6 nm, subtracting the injected charge at 2V and 1.6 nm, subtracting the charge at 3 V and 1.8 nm, and adding back in the amount of injected charge at 3V and 1.6 nm (since this charge was doubly subtracted). This differential process is applied sequentially to the entire two-dimensional array of measured data until the differential charge in each region of energy-depth space is determined. This differential charge is proportional to the density of trap states in that region of energy-depth space. The differencing is performed by a program written in Sigmaplot.

4.5 Results

Multiple SETFS scans taken at a particular location on the high-k dielectric film are shown in Figure 4.4. The surface potential signal (the difference between surface potential before and after a tunneling attempt at a particular ramp voltage step) is proportional to the amount of charge which tunnels during that tunneling attempt. Each data point on the graph represents the average of four tunneling attempts at the corresponding applied voltage and tip-sample gap, and the standard deviation of those four measurements is shown by the error bars. At large tip-sample gaps, no tunneling is observed, which is consistent with the small tunneling probability (wave function overlap) expected at this distance. The first consistent tunneling events are observed at a minimum tip-sample gap of 1.4nm, consistent with previous calculations of the tunneling rate [22] for the approximate time (2 milliseconds) the oscillating probe tip spends within tunneling range per measured point.

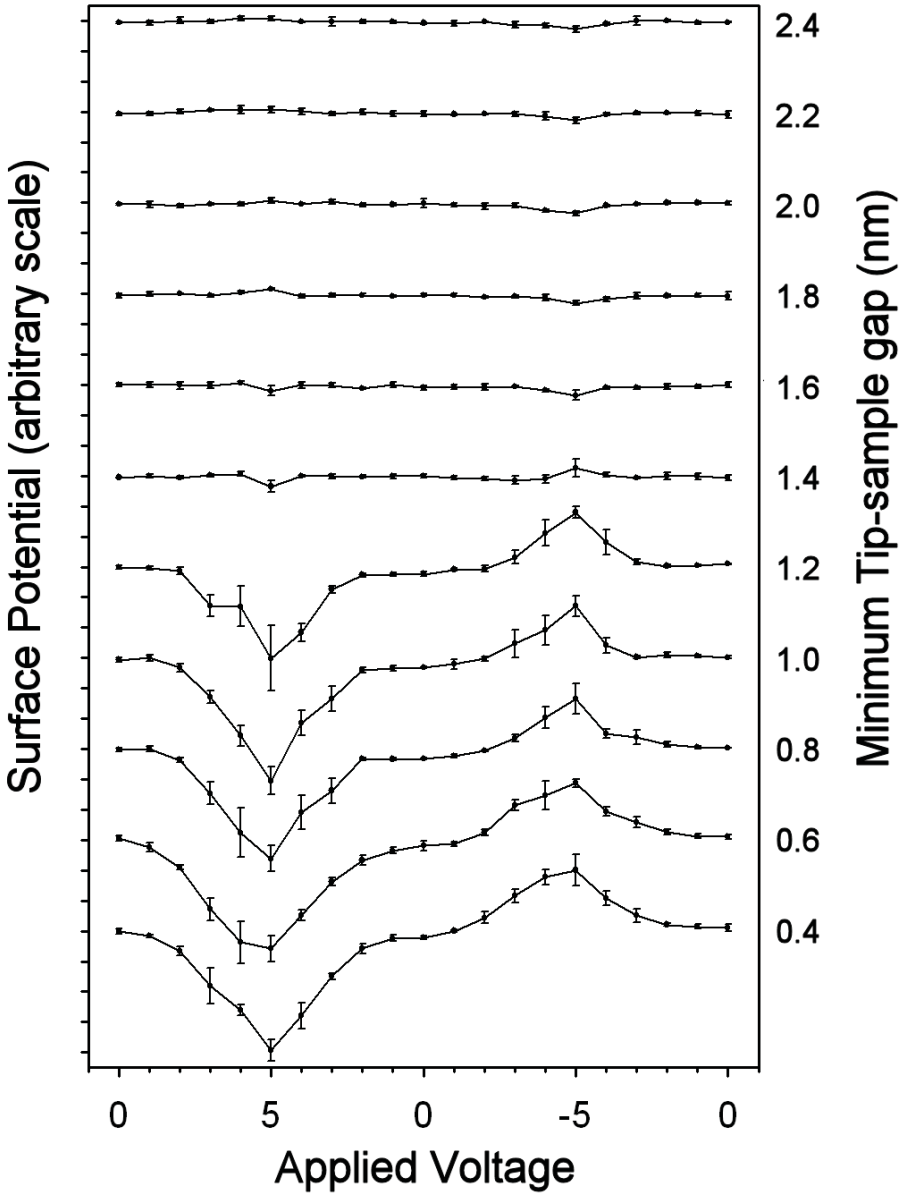

Figure 4.4. Multiple SETFS scans acquired at approximately the same location on the HfO_2 film. The surface potential is proportional to the amount of charge which tunnels at the given applied voltage. The surface potential signal increases as more depth-energy space is made accessible by either increasing the magnitude of the applied voltage or by decreasing the minimum tip-sample gap. The error bars represent the standard deviation of four measurements at each point. The scans have been offset for clarity, but each begins and ends near 0V surface potential.

A small lateral drift of the tip relative to the sample occurs during these measurements (estimated to be ~ 3Å/min). Therefore small changes in the exact location of the tunneling occurs during the spectroscopic data acquisition (spectra require 1.5 min/scan). However, it was observed that spectra acquired at different locations on this film do not change significantly, indicating that the density of trap states is relatively uniform. In future measurements, the drift rate can be reduced either by going to lower temperatures or performing faster spectroscopic scans. Currently, the scan rate is limited by charge detection measurement noise.

The differential charge data are input into the Maple program, which defines the regions of depth-energy space associated with each applied voltage/tip-sample height and assigns the values of differential charge to the appropriate regions. Figure 4.5 shows the differential charge which tunnels to each region of the depth-energy space. The data shown in Figure 4.4 and the algorithm in Figure 4.3 are used to assign these values, while the tunneling rate curves bounding the regions are calculated using the two-barrier method described above [22], with a simplifying assumption of a square vacuum tunneling barrier. The entire depth-energy space inside the HfO_2 dielectric layer is shown in Figure 4.5, in contrast to some of the previous figures which show only the region above midgap. The SETFS measurements performed on the HfO_2 sample did not show discrete single electron tunneling events. The trap density is apparently high enough that trap states are electronically coupled together. The data are therefore plotted with an arbitrary scale (vertical axis), showing only the relative density of trap states. The processed data show multiple dominant states or groups of states (in white), one at a depth of 4-6 nanometers and an energy between 1.5 and 2.3 eV above midgap. A second

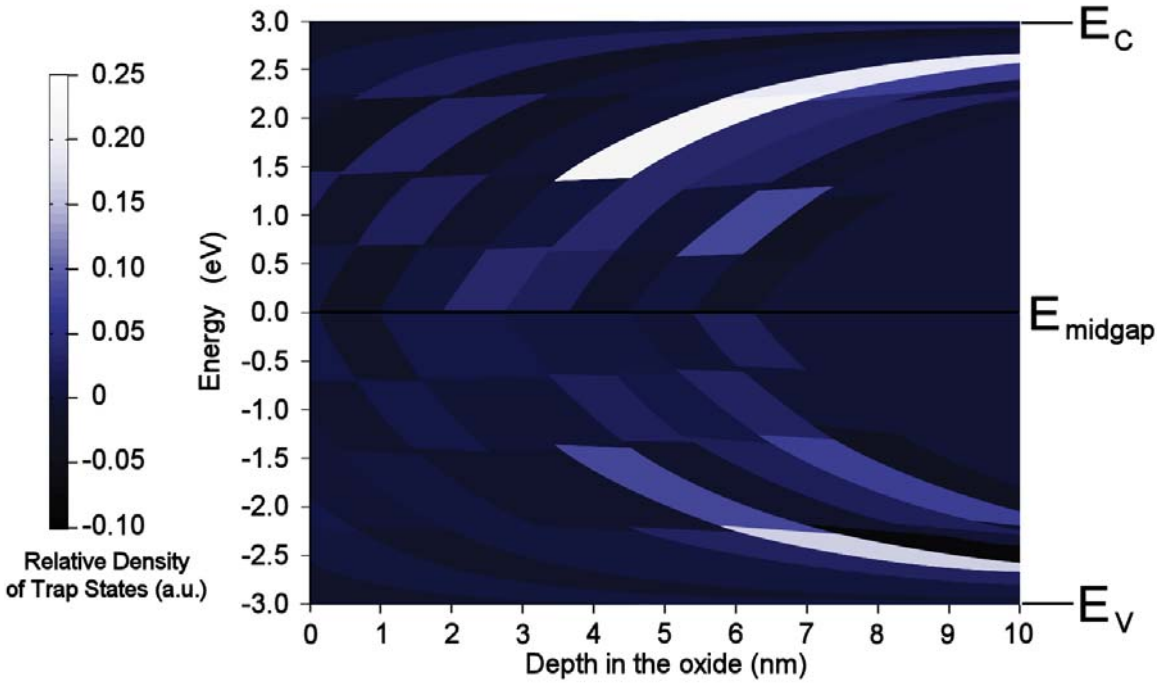

Figure 4.5. The relative density of trap states in depth-energy space. Three regions stand out as having large values for the differential charge, all shown as bright regions in the figure.

state or group of states appears at a depth of between 6 and 10 nm, with an energy beween 2.3 eV and 2.7 eV. Another appears at a depth of 6 to 10 nm and an energy between –2.3 eV and –2.7 eV. The other variations seen in Figure 4.4 are likely caused by noise in the measured data. The data noise is also the reason that some regions in the plot have a negative value. Note that the depth resolution near the center of the gap in these measurements is ~0.8 nm. The number of height and voltage steps taken during the measurement determines the resolution in both depth and energy. While the number of steps can be arbitrarily increased, the signal to noise ratio in the differenced data becomes smaller as the step size becomes smaller. It is very likely that the noise sources can be reduced in future experiments. With reduced noise, atomic resolution in the vertical dimension should be achievable.

The data presented here show the density of states in both energy and depth at a single location of a HfO_2 film. By combining the energy-depth methodology with the two-dimensional state imaging provided by DTFM [18], three-dimensional mapping of the spatial location of trap states with atomic spatial resolution may be achievable along with a determination of state energy. These results represent a first demonstration of the methodology to achieve this goal. Further refinements in both experimental method and modeling are expected.

4.6 Summary

In summary, an experimental and theoretical methodology for independently determining the energy and depth of buried trap states in a dielectric film has been described. A first demonstration of the concept has been performed. The method, when

combined with the two-dimensional imaging capability of Dynamic Tunneling Force Microscopy, should provide quantitative three-dimensional images of trap states in dielectric films with atomic scale spatial resolution. This capability opens a new door to study and understand atomic scale defects in electronic materials.

4.7 Acknowledgements

We thank S. Zafar and M. Frank of the IBM T.J. Watson Research Center for providing the processed HfO_2 samples and for useful discussions. We acknowledge support from IBM and the Semiconductor Research Corporation for this work.

4.8 References

[1] Wilk, G. D.; Wallace, R. M.; Anthony, J. M. *J. Appl. Phys.* **2001**, *89*, 5243.

[2] Zhu, W. J.; Ma, T. P.; Zafar, S.; Tamagawa, T. *IEEE Elec. Dev. Lett.* **2002**, *23*, 597.

[3] Bersuker, G.; Sim, J. H.; Park, C. S.; Young, C. D.; Nadkarni, S. V.; Choi, R.; Lee, B. H. *IEEE Trans. on Dev. and Mat. Rel.* **2007**, *7*, 138.

[4] Ludeke, R.; Gusev, E. *J. App. Phys.* **2004**, *96*, 2365.

[5] Kyuno, K.; Kita, K.; Toriumi, A. *App. Phys. Lett.* **2005**, *86*, 063510.

[6] Kremmer, S.; Wurmbauer, H.; Teichert, C.; Tallarida, G.; Spiga, S.; Wiemer, C.; Fanciulli, M. *J. App. Phys.* **2005**, *97*, 074315.

[7] Young, C. D.; Zhao, Y.; Heh, D.; Choi, R.; Lee, B. H.; Bersuker, G. *IEEE Trans. on Elec. Dev.* **2009**, *56*, 1322.

[8] Hoppe, E. E.; Aita, C. R. *App. Phys. Lett.* **2008,** *92,* 141912.

[9] Kerber, A.; Cartier, E. A. *IEEE Trans. on Dev. and Mat. Rel.* **2009**, *9*, 147.

[10] Nguyen, N. V.; Davydov, Albert V.; and Chandler-Horowitz, D. *App. Phys. Lett.* **2005**, *87*, 192903.

[11] Price, J.; Lysaght, P. S.; Song, S. C.; Li, H.; Diebold, A. C. *App. Phys. Lett.* **2007**, *91*, 061925.

[12] Price, J.; An, Y. Q.; Lysaght, P. S.; Bersuker, G.; Downer, M. C. *App. Phys. Lett.* **2009**, *95*, 052906.

[13] Klein, L. J.; Williams, C. C. *Appl. Phys. Lett.* **2002**, *81*, 4589.

[14] Bussmann E.; Kim D. J.; Williams, C. C. *Appl. Phys. Lett.* **2004**, *85*, 2538.

[15] Bussmann, E.; Zheng, N.; Williams, C. C. *Nano Lett.* **2006**, *6*, 2577.

[16] Bussmann, E.; Williams, C. C. *Appl. Phys. Lett.* **2006**, *88*, 263108.

[17] Zheng, N.; Johnson, J. P.; Williams C. C.; Wang, G. **2010** *Nanotechnology* (accepted).

[18] Johnson, J. P.; Zheng, N.; Williams, C. C. *Nanotechnology* **2009**, *20*, 055701.

[19] Dâna, A.; Yamamoto, Y. *Nanotechnology* **2005**, *16*, S125.

[20] Stomp, R.; Miyahara, Y.; Schaer, S.; Sun, Q.; Guo, H.; Grutter, P.;Studenikin, S.; Poole, P.; Sachrajda, A. *Phys. Rev. Lett.* **2005**, *94*, 056802.

[21] Zhu, J.; Brink, M.; McEuen, P. L. *Appl. Phys. Lett.* **2005**, *87*, 242102.

[22] Zheng, N.; Williams, C. C.; Mishchenko, E. G.; Bussmann, E. *J. Appl. Phys.* **2007**, *101*, 093702.

CHAPTER 5

SINGLE-SPIN ELECTRON SPIN RESONANCE

5.1 Introduction

Because it is possible to address an individual electronic state with SETFM, it is a technique that also shows potential for detecting the spin of a single electron. This chapter explores the possibility of observing magnetic resonance for individual paramagnetic trap states in oxides, which could allow for a more direct chemical identification of these states along with the spatial location offered by SETFS and DTFM.

For decades, magnetic resonance has been used to perform spectroscopy and image internal structure in physics, chemistry, and medicine. In magnetic resonance, spins precess in a magnetic field B_0 at the Larmor frequency

$$\omega_L = -\frac{eg}{2m} B_0, \tag{1}$$

with e the elementary charge, m the particle mass, and g (the g factor) a dimensionless quantity which depends on the type of spin (nuclear or electronic) and on the chemical environment of the spin. The magnetic field B_0 induces Zeeman splitting of the spin energy into high- and low-energy states where the spin is antiparallel and parallel to B_0,

respectively. The spins can be flipped between these states by an appropriately chosen RF electromagnetic radiation B_1 tuned to the Larmor frequency. Nuclear magnetic resonance benefits from the abundance of nonzero nuclear spins, notably in hydrogen, but the magnetic moment of nuclear spins is smaller than electron spins by a factor of approximately 2000 ($\sim m_p/m_e$). This means detection of some number of nuclear spins by magnetic resonance requires more sensitivity than it does to detect the same number of electronic spins in electron spin resonance (ESR). ESR has been used to identify chemical species that contain unpaired electrons, including paramagnetic centers in electronic materials [1-3].

Detecting magnetic resonance by induction is not compatible with nanometer-scale resolution, since at least 10^{12} nuclear spins [4] or 10^7 electron spins [5, 6] must be contained in the volume that is in resonance with the magnetic field B_1. Detection of single spins has been demonstrated using a number of techniques, such as magnetic resonance force microscopy (MRFM) [7], electrically detected magnetic resonance (EDMR) [8, 9], optically detected magnetic resonance (ODMR) [10-12], and possibly scanning tunneling microscopy [13]. Of these, only the optical method has detected a single spin at room temperature—the spin of an individual NV center in diamond. There is also a possibility that coupling individual diamond NV centers to other individual spins could be used in some way to sense spins close to it at room temperature [14, 15], although to now this has not been demonstrated.

5.2 Detection of single spins with SETFM

Because of the strong dependence of the tunneling rate on gap [16], SETFM can be used to address individual electronic states. This makes it an excellent candidate for nanometer-scale imaging of single spins in three dimensions at noncryogenic temperatures. The method described by Williams, Böhme, and McCamey [17] relies on having two paramagnetic states at the same energy, one in the surface and one in the tip. If the two states are brought close together, electrons will tunnel between states. The tunneling rate will be affected by the orientation of the electrons' spins because of the Pauli exclusion principle [18]. This is what is meant by spin dependent tunneling. Specifically, only when the spins of the electrons are antiparallel can the electrons occupy the same state, so the tunneling is modulated (turned off and on) by the relative spin direction. See Figure 5.1. Because the tunneling rate is changed by the spin blocking, if there is a means to detect whether the electrons are together or separated, observation of a spin dependent tunneling signal is possible. The following sections will discuss this detection, which is possible because the electrostatic force on the tip is different when the charges are together or separate.

5.2.1 Force calculation for two charges, each in a dielectric

Because the cantilever must be sensitive to whether the electrons are separated or together, the frequency shift of the cantilever for these two situations is calculated. First the electrostatic potential is found, which gives the total electrostatic energy E when multiplied by the free charge in the system according to the equation

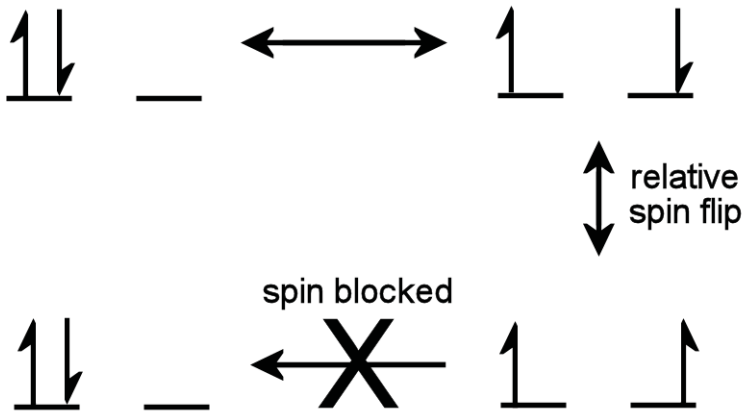

Figure 5.1 Spin blocking effect on electron tunneling. When two electrons are in separate paramagnetic states within tunneling range of each other, tunneling can only occur if the spins are antiparallel (top case). After [18].

$$E = \sum_i \frac{q_i V_i}{2}, \tag{2}$$

where the sum is over all free charges and V is the electrostatic potential at the location of each free charge q [19].

The potential is found using a solution for the potential of a charge near a semi-infinite dielectric slab, which involves an infinite series of image charges [20]. Namely,

$$V(z,\rho) = \frac{q}{4\pi\varepsilon_1\varepsilon_0\sqrt{|z+d|^2+\rho^2}} + \sum_{n=1}^{\infty}\left(Vaa_n + Vab_n + Vbb_n + Vba_n\right), \tag{3}$$

where z and ρ are cylindrical coordinates with the first interface of the slab at $z = 0$, q is the charge placed at $z = -d$ and $\rho = 0$, and ε_1 is the relative dielectric constant of the medium where the charge is placed. See Figure 5.2. The terms in the sum in equation (3) are defined as follows:

$$Vaa_n = -\frac{\beta^{2n-1}q}{4\pi\varepsilon_1\varepsilon_0\sqrt{\left(|z|+(2n-2)c+d\right)^2+\rho^2}}, \tag{4}$$

$$Vab_n = -\frac{\beta^{2n}q}{4\pi\varepsilon_1\varepsilon_0\sqrt{\left(|z-c|+(2n-1)c+d\right)^2+\rho^2}}, \tag{5}$$

$$Vbb_n = \frac{\beta^{2n-1}q}{4\pi\varepsilon_1\varepsilon_0\sqrt{\left(|z-c|+(2n-1)c+d\right)^2+\rho^2}}, \tag{6}$$

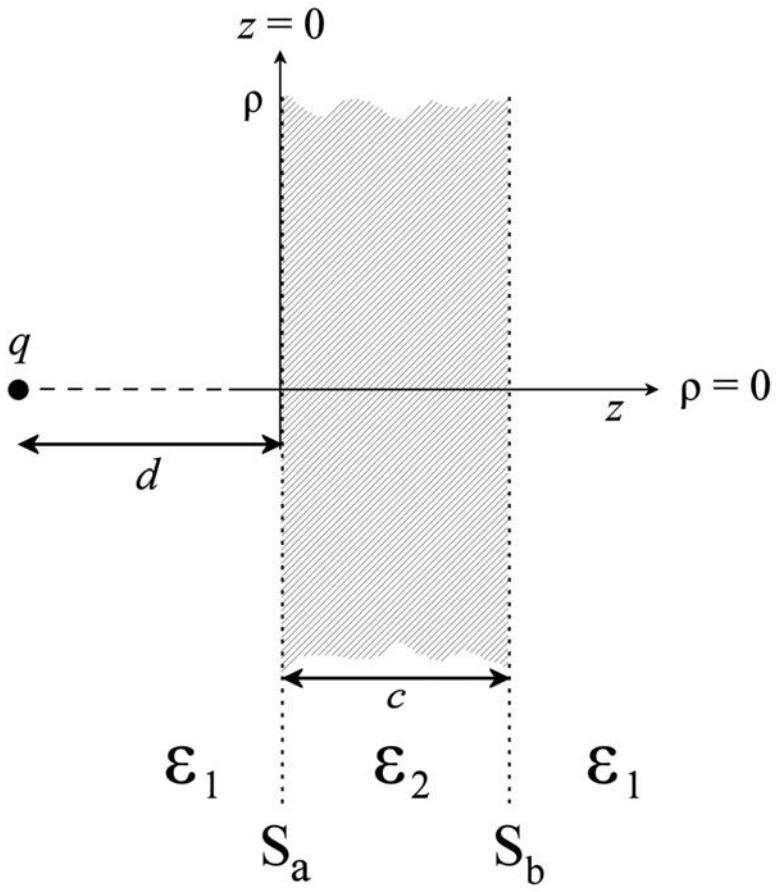

Figure 5.2 Dielectric slab model for a dielectric tip and dielectric sample. A charge q in a material of dielectric constant ε_1 a distance d to the left of a semi-infinite slab of material with dielectric constant ε_2. The solution for the electrostatic potential as a function of cylindrical coordinates z, ρ can be expressed with a series of image charge terms.

$$Vba_n = \frac{\beta^{2n} q}{4\pi\varepsilon_1\varepsilon_0\sqrt{\left(|z| + 2nc + d\right)^2 + \rho^2}}, \tag{7}$$

$$\text{With } \beta = \frac{\varepsilon_2 - \varepsilon_1}{\varepsilon_2 + \varepsilon_1}. \tag{8}$$

Here ε_2 is the relative dielectric constant of the slab, and c is the thickness of the slab. The first term is the potential due to the charge in the absence of the dielectric slab of dielectric constant ε_2, and the terms within the sum are the potential from the image charges that correctly represent the effects from the polarized bound charges at the boundaries and their effects on each other.

When the slab is vacuum ($\varepsilon_2 = 1$) and the left and right regions in Figure 5.2 are SiO_2 ($\varepsilon_1 = 4$), the solution describes the situation for paramagnetic states on either side of the vaccum gap. Effects from tip curvature are neglected since the tip radius of curvature (~30nm) is much larger than the dimensions important to the problem.

With the electrostatic potential defined everywhere, the energy of the system is found by taking the sum of all free charges multiplied by the potential at its location. The potential does contain an infinite series of terms, but the sum can be truncated for the calculation since the positions of the image charges get further from the location of the free charge, seen by the terms that go as $2nc$ in the denominator of equations (4)-(7). The force is obtained by taking the derivative of the total energy found in equation (2) with respect to a differential change in the tip-sample gap c:

$$F(c) = -\frac{\partial E}{\partial c}. \tag{9}$$

The first term in the potential given by equation (3) has a singularity at the location of the charge ($z = -d$, $\rho = 0$), but this term does not depend on c, and so it is not important in calculating the force and can be discarded. This force is used to find the frequency shift of the tip when the two charges are together or separate in the following section.

5.2.2 Frequency shift calculation for two charges, each in a dielectric

As discussed in Chapter 1, when an oscillating probe experiences a small force gradient during its oscillation, the resonant frequency changes by an amount

$$df = f - f_0 \approx -\frac{f_0 F_{eff}^{'}}{2K}, \tag{10}$$

where K the spring constant of the oscillator and f_0 is the resonant frequency in the absence of the force gradient. In Section 1.2, the effective force gradient is given by

$$F_{eff}^{'} = -\frac{2}{\pi A}\int_{-1}^{+1} F\left(z + A\left(1+u\right)\right)\frac{u}{\sqrt{1-u^2}}du. \tag{11}$$

Here, z is the distance of closest approach, $F(c)$ is the force on the cantilever as a function of gap given in equation (8), and A is the oscillation amplitude. Two substitutions have been made: $c = z + A(1 + u)$ and $u = \cos(2\pi f_0 t)$.

To review, in our force-detected scheme, the frequency shift signal df is the way tunneling is detected. The original purpose in finding df given by equations (10) and (11)

and the force in equation (9) was to see how large a change in the frequency shift signal would occur for a tunneling event that either separated the charges or brought them together. The change in these cases would be of the same magnitude but opposite sign.

When the state in the tip is brought within tunneling range of the state in the sample so that electrons in the two states can shuttle back and forth between the states, a random telegraph signal (RTS) is produced in the cantilever frequency shift. The size of this signal depends on the size of the change in frequency shift discussed above, which has been estimated in a calculation contained in the Appendix.

5.3 Random telegraph signal on and off resonance

For a single-spin ESR measurement to be possible, there must be a detectable difference between the RTS when the applied B_1 field is on resonance and when it is off resonance. It will be shown below that the average value of the frequency shift is unsuitable for this measurement [21]. For now, it is enough to say that there is not a difference in the average value of the frequency shift for the two cases, but there is a difference in the low-frequency power of the RTS signal for the two situations. The spin-lattice relaxation time T_1 for E' centers has been reported to be greater than 200μs at room temperature [2]. However, even 200μs gives an average spin flip time that corresponds to a frequency (~5kHz) that is outside of the detection bandwidth of the frequency demodulator (which measures the frequency shift signal) currently in use in our AFM system because it has a roll-off of approximately 1kHz. Because of this, direct detection of the spin flipping is not possible at room temperature and an indirect method to detect spin-dependent tunneling is required instead.

Let us look more carefully at the RTS signal in the cases for on- and off-resonance. When the electrons are in the same state, whether B_1 is on- or off-resonance, the time it takes for one of the electrons to tunnel through the gap to the other state has some average value T_t, the inverse of the tunneling rate, which is a function of state-state separation. See Figure 5.3. If the electrons are in the same state, their relative orientation cannot change. Once the electrons separate, though, if one electron flips so that they are in the same spin state (both up or both down), tunneling back is forbidden by the Pauli exclusion principle. When separated, the spins will flip relative to one another with an average rate defined by T_f, the average time for one flip of the spin relative to the other to occur. T_f is smaller in the on-resonance case compared with the off-resonance case, where T_f is equal to T_1 (the spin-lattice relaxation time).

In the case where B_1 is on resonance, $T_f = \gamma B_1$ and the average spin flip rate can be faster than the tunneling rate ($T_t >> T_f$). The effect of the resonance is to double the average time it takes for the electrons to come back together once they are separated, since on average they will be spin blocked half the time they are separated. See Figure 5.3a. This leads to an average occupation of the separated state of

$$\frac{0 \cdot T_t + 1 \cdot 2T_t}{3T_t} = \frac{2}{3}, \tag{12}$$

since on average it takes twice as long to tunnel back together as it does to tunnel apart.

When B_1 is off resonance ($T_t << T_f$), the electrons are free to shuttle back and forth between the two states until one spin has flipped relative to the other. The average time it takes for this to happen is 2 T_f, since half the time the spins are together and half

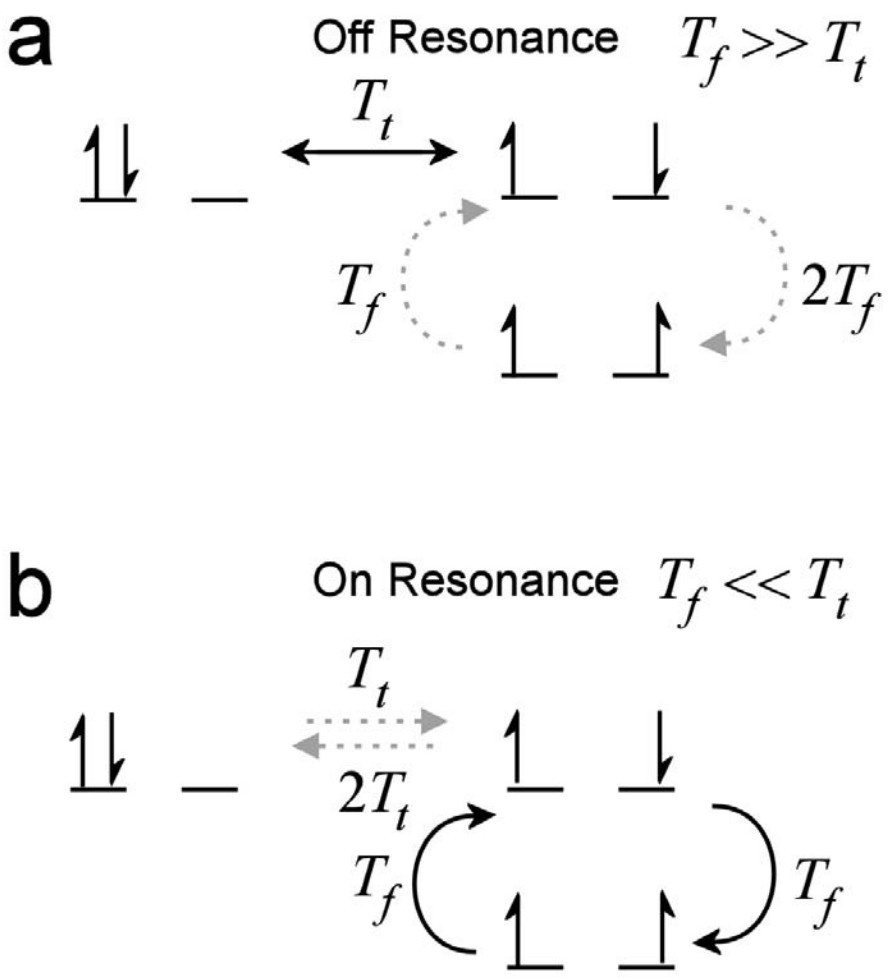

Figure 5.3 Spin blocking in the random tunneling signal (RTS). (a) Off resonance, the electrons spend most of the time tunneling back and forth between states because it is rare (shown by the dotted arrows) for a spin flip to occur. When a spin flip does happen while separated, the spins remain separated until again one of them flips, which takes a time T_f on average. (b) On resonance, once the electrons are separated, they flip in a very short time compared with the tunneling rate. This has the effect of increasing the time it takes to tunnel back together because during half of the time spent apart, tunneling is spin-blocked. In both cases, half the time spent separated is spent in the spin-blocked state.

the time they are separated and flipping can only occur when they are separated. See Figure 5.3b. This gives an average occupation of the separated state of

$$\frac{\frac{1}{2}\cdot 2T_f + 1\cdot T_f}{3T_f} = \frac{2}{3}, \tag{13}$$

which is the same value as for the on-resonance case given in equation (12). This analysis of the average value was thanks to Christoph Boehme and Dane McCamey.

Equations (12) and (13) show that the average frequency shift is not sensitive to whether B_1 is on or off resonance. However, it can be seen by comparing Figure 5.4a and Figure 5.4b that there is more low-frequency power in the off-resonance RTS. The result of a numerical simulation of the RTS for both cases by Payne, et al. [22], shown in Figure 5.4c and 5.4d, illustrates this difference. If the RTS is low-pass filtered, the amplitude of the frequency noise signal does depend on whether B_1 is on or off resonance, and spin dependent tunneling can be observed.

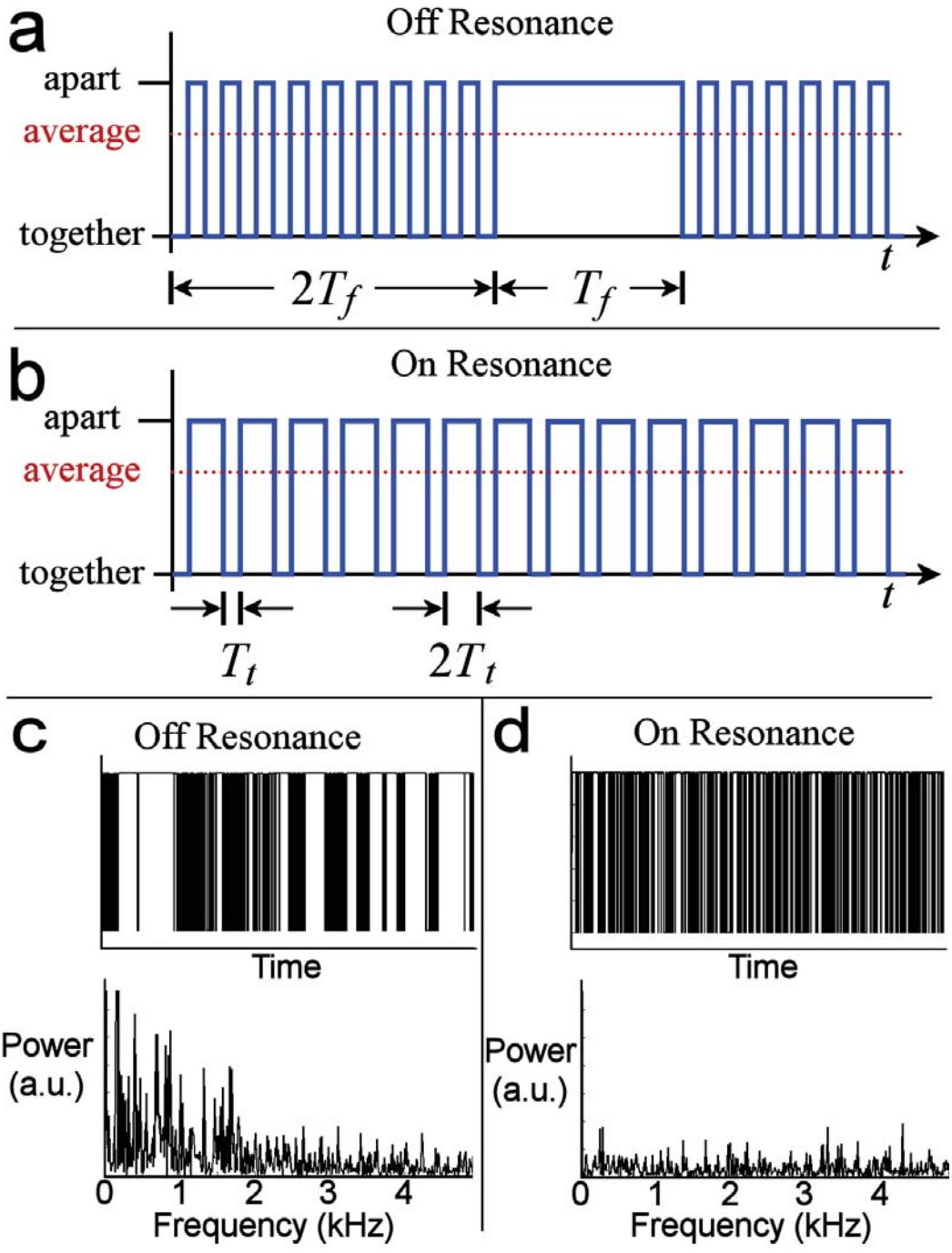

Figure 5.4 Simulated random telegraph signal (RTS) for B_1 off resonance (a, c) and on resonance (b, d). (a) Off resonance, the charge shuttles back and forth with an average tunneling time T_t. Occasionally, tunneling becomes spin blocked because one of the spins flips while separated. When this happens, the spins stay separated for an average time of T_f. (b) On resonance, the charges stay separated twice as long on average than they stay together because of spin blocking. (c) and (d) are from a numerical simulation [22], which shows that the off-resonance signal contains more low-frequency components in its power spectrum.

A critical question remains, though, as to whether the difference in the RTS signal for the two cases can be detected at room temperature using our current setup. Detection of the spin-dependent tunneling signal is only possible if the RTS frequency noise difference is larger than the frequency noise of the AFM system. The *df* noise of the current microscope has been measured as a function of detection bandwidth, and the results are shown in Figure 5.5. Also plotted in this figure is a theoretical calculation of the noise following Kobayashi [23]. The theoretical model overestimates the *df* noise by about 30-80%, depending on the detection bandwidth. Our group has combined the results of the frequency shift calculation described above with the RTS simulations [22] and have determined that the frequency shift noise in our current microscope is greater than the signal difference in the single spin case, so spin-dependent tunneling is not detectable at room temperature under current conditions.

However, much lower results for *df* noise have been obtained by other groups after improving the optical , for example at Kyoto University and Universität Osnabrück [23, 24]. If the noise in our system is improved to match that of these groups', it has been shown using the same theoretical noise calculation in Figure 5.5 [23] that even at room temperature the RTS difference signal would be larger than the *df* noise at each of the detection bandwidths that were simulated [22]. This means that improvements to the optical beam detection system (by increasing the power of the light source and/or replacing the position-sensing photodiode) could make single spin ESR measurements possible even at room temperature with our system.

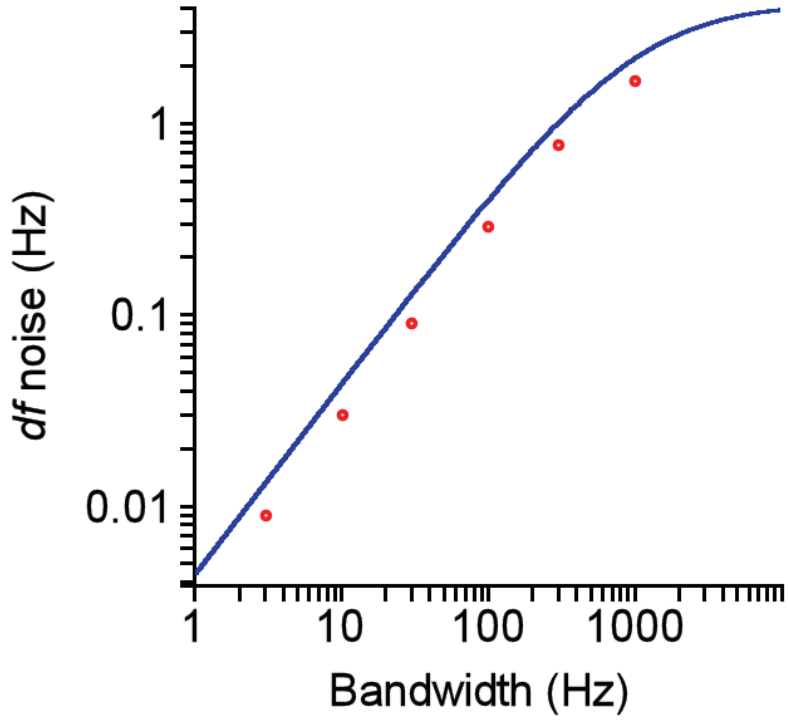

Figure 5.5 Measured *df* noise (circles) in the AFM system as a function of measurement bandwidth compared with the prediction from theory (solid line) [23]. The theoretical calculation systematically overestimates the noise by a small amount.

5.4 Experimental considerations for single-spin ESR

5.4.1 Changes to the AFM probe

The proposed method requires tunneling between two paramagnetic states. The conductive AFM probe typically used for SETFM is replaced with a Si tip that has a thick oxide grown on its surface. The growth parameters are chosen to give approximately 25nm SiO_2. The Si tips are heated to 1000ºC in 0.5 atm of O_2 for 20 minutes. Probes with these oxidation parameters detect what seems to be a random telegraph signal that only appears when the tip is within tunneling range. See Figure 5.6 for an example of this signal as the tip is slowly brought within tunneling range and then back out again. Similar results are obtained with other oxidized tips, as well.

5.4.2 Magnetic fields B_0 and B_1

The magnetic field B_0 at the location of the sample is supplied for this experiment by a magnetic field which already exists in the UHV chamber. Because only single spins are involved, the value of B_0 is only important at the location of the state itself, making spatial uniformity of B_0 less critical than in inductive magnetic resonance experiments, which detect spin ensembles. However, the more precisely the magnitude of B_0 at the tip's location is known, the greater the certainty in the Larmor precession frequencies to be explored to find magnetic resonance.

B_0 was measured using both a magnetoresistive sensor and a Hall probe, and the calibration for these sensors is shown in Figure 5.7, in which each sensor was placed in a Helmholtz coil to supply a known magnetic field.

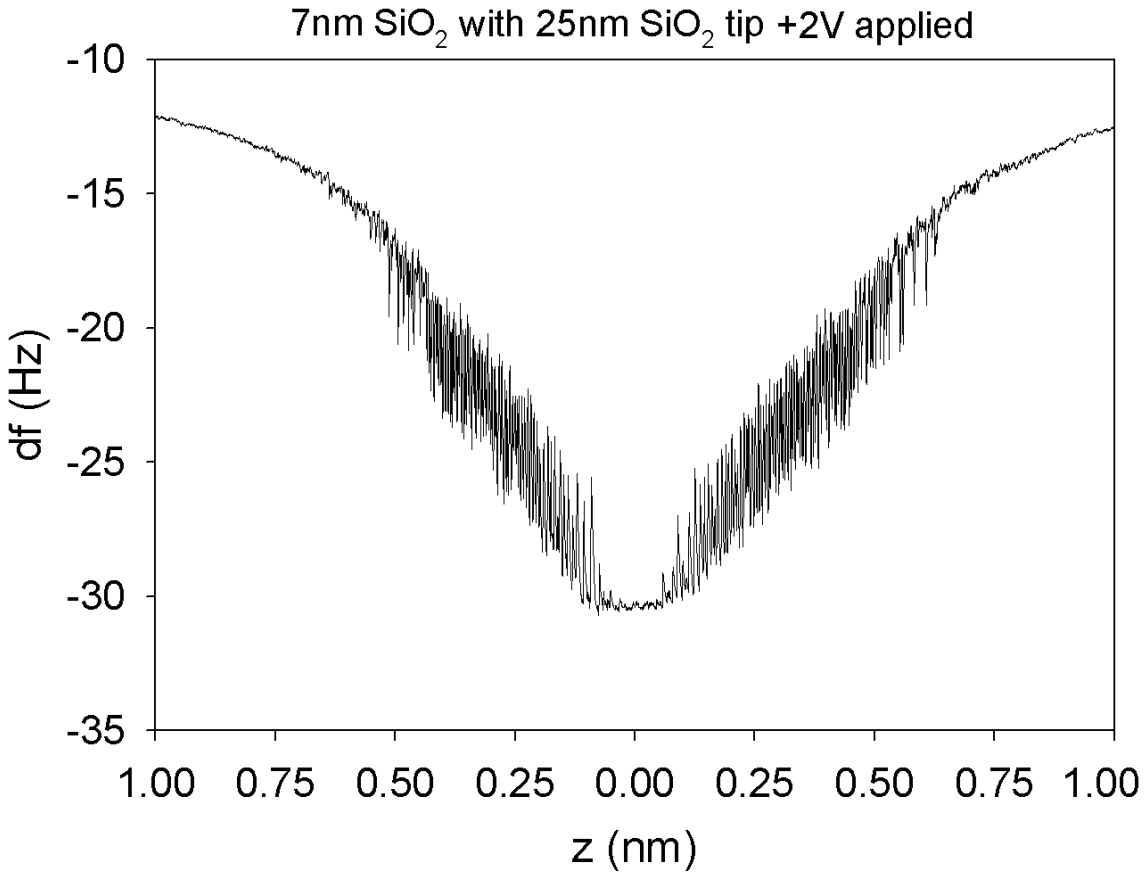

Figure 5.6 Experimental random telegraph signal. As the oxidized tip is brought within tunneling range of the SiO_2 surface, an apparently random telegraph signal is observed. It turns off when the tip comes in contact with the surface near $z = 0$nm.

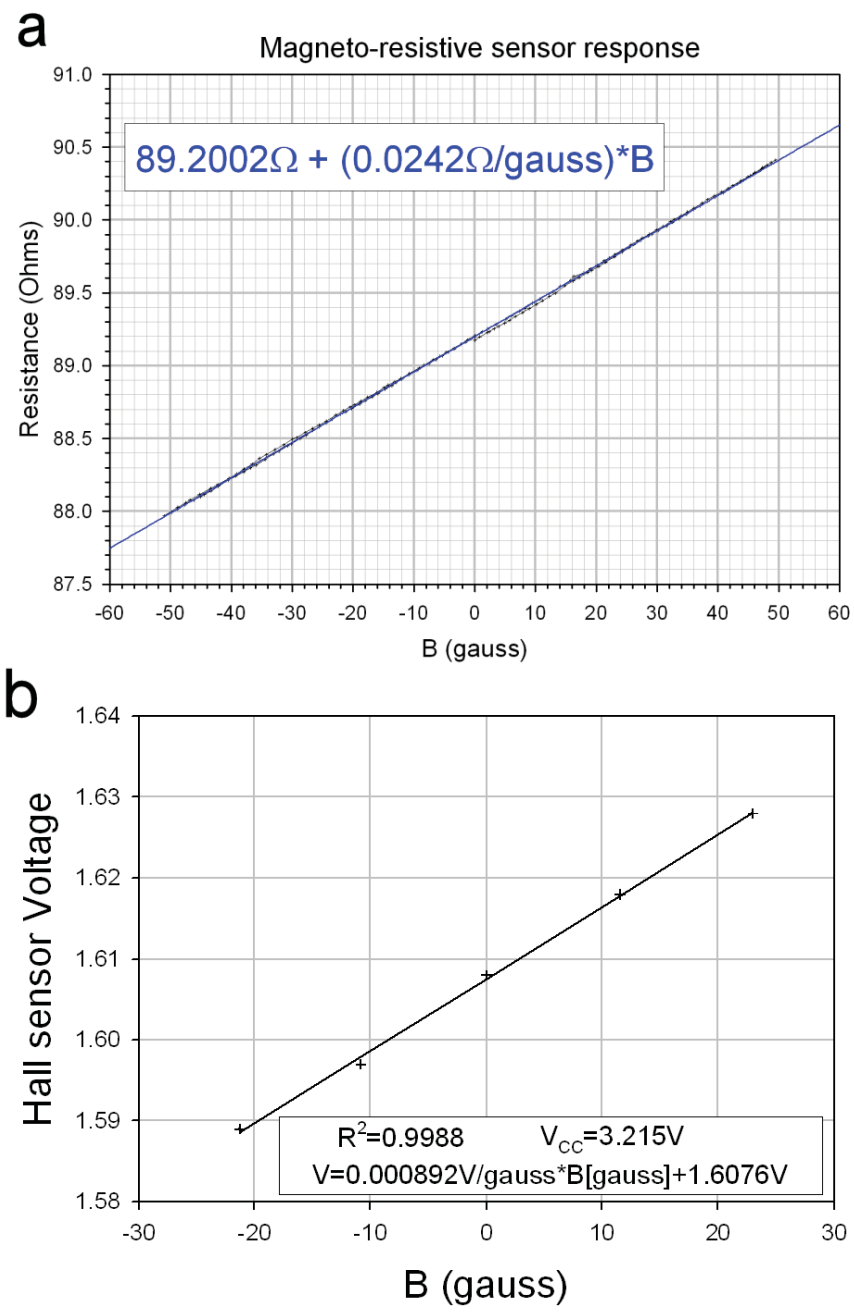

Figure 5.7 Magnetoresistive sensor and Hall sensor calibration. Both sensors were used because their different geometries made each one useful for different measurement axes in the crowded UHV chamber. A Helmholtz coil generated the magnetic field *B*.

The measured components of B_0 at the location of the tip are $B_x = 7 \pm 2$ gauss, $B_y = 44 \pm 2$ gauss, $B_z = 9 \pm 5$ gauss, giving a total $B_0 = 45 \pm 3$ gauss. Here, $\hat{z}$ is upward, $\hat{y}$ is toward the tip from the sample, and $\hat{x} \times \hat{y} = \hat{z}$. The uncertainty arises because of the difficulty in accurately positioning the sensors at the position of the tip. Using equation (1), the range of measured B_0 corresponds to a range of possible resonant B_1 frequencies of 126 ± 9 kHz.

The B_1 field is created by a coil within the UHV system. A Maple worksheet was created in order to predict various properties of the coil and the magnetic field it generates. Some of the most important predictions are listed here. Using equation (1), in order to flip the spins with an average time of T_f = 10μs, the magnetic field required is B_1 = 1.78x10^{-2} gauss. The field a distance z from a coil of radius r with N turns with its axis an angle θ from perpendicular to B_0 is

$$B = \frac{\mu_0 N I r^2 \cos(\theta)}{2\left(r^2 + z^2\right)^{3/2}}. \tag{14}$$

After solving for the current I in equation (14), the power dissipated in the coil is $P = I^2R$. One important consideration in designing the coil is that the power dissipated in the coil should be as small as possible because heat transferred into the system can raise its temperature and cause the tip to move relative to the sample due to thermal drift. For a given separation distance between coil and sample z, the power dissipated in the coil is minimized for $r = z$. Thermal drift that makes the two states drift out of tunneling range with each other would disrupt the measurement. For r = 1mm and z = 1mm and θ = 30˚, the calculated current required to supply a B_1 of 1.78x10^{-2} gauss is 9.25mA. This current gives a power dissipated in a 1-turn coil of wire (wire diameter 127 μm) of 725 nW,

which should be sufficiently small to avoid problems with adding thermal drift to the microscope. Also, the required drive voltage to produce this current in the coil was calculated to be 0.452V at 126kHz.

A coil with the parameters listed above was fabricated and placed in the chamber with a transmission line to bring the signal from outside the chamber. Also, a moveable support system to hold the coil close to the sample was added so that this coil used for the spin experiment can be moved away for standard experiments in which the coil is not required. Another result from the simulation is that for the coil and transmission line added to the system, the current through the coil differs from the current at the input by less than 5% in the range of frequencies for B_1 near 126kHz calculated above. This is important because it means that the B_1 power can be straightforwardly calculated from the power output by the signal generator.

5.4.3 Low temperature

Besides the improvements to the optical beam detection mentioned in Section 5.3, sensitivity can also be gained by decreasing the measurement temperature. At a lower temperature, the spin-lattice relaxation time T_1 of the E' centers is much longer [2], and this means that potentially even direct observation of the RTS signature on and off resonance shown in Figure 5.4 may be visible in the frequency shift signal.

5.5 References

[1] Al'tshuler S, Zavoisky E and Kazyrev B 1944 *J. Exptl. Theoret. Phys. (U.S.S.R)* **14** 407

[2] Castle J G, Jr.; Feldman D W; Klemens P G and Weeks R A 1963 *Phys. Rev.* **130** 577

[3] Lenahan P M and Conley J F, Jr. 1998 *J. Vac. Sci. & Tech. B* **16** 2134

[4] Ciobanu L, Seeber D A and Pennington C H 2002 *J. Magn. Reson.* **158** 178

[5] Blank A, Suhovoy E, Halevy R, Shtirberg L and Harneit W 2009 *Phys. Chem. Chem. Phys.* **11** 6689

[6] Kuehn S, Hickman S A and Marohn J A 2008 *J. Chem. Phys.* **128** 052208

[7] Rugar D, Budakian R, Mamin H J, Chui B W 2004 *Nature* **430** 329

[8] Elzerman J M, Hanson R, Willems van Bevern L H, Witkamp B, Vandersypen L M K, and Kouwenhoven L P 2004 *Nature* **430** 431

[9] Xiao M, Martin I, Yblonovitch E and Jiang H W 2004 *Nature* **430** 435

[10] Wrachtrup J, von Borcyskowski C, Bernard J, Orrit M and Brown R 1993 *Phys. Rev. Lett.* **71** 3565

[11] Jelezko F, Gaebel T, Popa I, Gruber A and Wrachtrup J 2004 *Phys. Rev. Lett.* **72** 076401

[12] Hanson R, Gywat O and Awchalom D D 2006 *Phys. Rev. B* **74** 161203

[13] Mannasen Y, Hamers R J, Demuth J E and Castellano A J, Jr.1989 *Phys. Rev. Lett.* **62** 2531

[14] Maze J R, Stanwix P L, Hodges J S, Hong S, Taylor J M, Cappellaro P, Jiang L, Gurudev Dutt M V, Togan E, Zibrov A S, Yacoby A, Walsworth R L and Lukin M D 2008 *Nature* **455** 644

[15] Balasubramanian G, Chan I Y, Kolesov R, Al-Hmoud M, Tisler J, Shin C, Kim C, Wojcik A, Hemmer P R, Krueger A, Hanke T, Leitenstorfer A, Bratschitsch R, Jelezko F and Wrachtrup J 2008 *Nature* **455** 648

[16] Zheng N, Williams C C, Mishchenko E G and Bussmann E 2007 *J. Appl. Phys.* **101** 093702

[17] Williams C C and Boehme C 2010 NSF Award abstract #0959328

[18] McCamey D R, Morley G W, Seipel H A, Brunel L C, van Tol J and Boehme C 2008 *Phys. Rev. B* **78** 045303

[19] Jackson J D 1999 *Classical Electrodynamics*, 3rd ed. Wiley (New Jersey) pp. 40-43

[20] Böhme C, personal communication.

[21] Sometani T 2000 *Eur. J. Phys.* **21** 549

[22] Payne A D, Johnson J P, Winslow D W and Williams C C 2010 SRC Deliverable Report

[23] Kobayashi K, Yamada H and Matsushige K 2009 *Rev. Sci. Inst.* **80** 043708

[24] Torbrügge S, Lübbe L, Cranney M, Eguchi T, Hasegawa Y and Reichling M 2008 *Rev. Sci. Inst.* **79** 083701

CHAPTER 6

CONCLUSION AND FUTURE WORK

6.1 Conclusion

Dynamic Tunneling Force Microscopy provides for the first time the ability to image electron trap states in completely non-conducting films with atomic-scale spatial resolution. Also, the depth and energy of trap states can be independently determined by a novel application of Single Electron Tunneling Force Spectroscopy. This information is important for gaining a physical understanding of trap states, which play an important role in electronic device performance.

In addition to the unique ability of these techniques to image and characterize localized states in insulating materials, the ability to perform spectroscopy of Au nanoclusters placed on thick insulating films also may provide a means to perform spatially-resolved energetic characterization of other nanoclusters, molecules, and low-dimensional electronic systems. The greater separation from a metal surface electrode in these measurements means that these nanosized systems can be measured with a greater decoupling from their support than is currently possible with Scanning Tunneling Spectroscopy.

A force-detected, spin-dependent tunneling signal due to electrons tunneling between two paramagnetic states that are on either side of the AFM tip-sample gap may offer a way to detect the spin of a single electron with subnanometer spatial resolution. With improvements to the force detection apparatus, this measurement may even be possible at room temperature.

6.2 Future Work

The changes to the optical deflection detection system mentioned in Chapter 5 will also improve the surface potential and DTFM measurements. One effect of decreasing the noise in the frequency shift signal is that dynamic tunneling will be possible at larger measurement bandwidths, which will make thermal drift a smaller problem because scans can be acquired in less time. A similar benefit should be seen in the SETFS spectrum, where improved signal to noise will allow for finer steps in height and applied voltage. This will decrease the size of the regions of depth-energy space that are accessible for tunneling, improving the experiment's resolution in both dimensions (energy and depth).

The noise in the SETFM measurements is not only due to noise in the deflection detection system. As in the previous work in SETFM, the noise in the depth-energy measurements may actually be limited by surface charge fluctuations. A dynamic version of the depth-energy separation experiment could decrease measurement time while also decreasing the sensitivity to the surface charge noise by inducing a shuttling signal that is out of phase with the surface potential signal (sensitive to charge fluctuations) as in DTFM. One area where progress is needed is in implementing such a technique. In order

to perform spectroscopic measurements, a bias voltage must be applied when in tunneling range in order to obtain a spectrum, and the DTFM signal size depends on the magnitude of the applied DTFM voltages. Options for performing this type of measurement need to be explored. One possible approach would be to establish the relationship between the signal size for a known amount of shuttled charge as a function of applied voltage.

Another area where further work is required is to establish an absolute energy scale in the spectroscopic measurements. The measurements presented in this dissertation are all taken relative to the flatband voltage, which is the voltage that must be applied to minimize the average electric field in the tip-sample gap. When the flatband voltage is applied, an assumption has been made that the position of the tip Fermi level is near the midgap level, halfway between the valence and conduction bands. This is only an approximation, which puts the spectroscopic results from SETFS on a relative energy scale. The results could be improved by establishing a method to reliably determine the location of the tip Fermi level relative to the conduction/valence band of the sample, which would put the measurements on an absolute energy scale. Some possible methods to accomplish this are listed here. Photo-assisted tunneling could be used to find the conduction/valence band, which has the advantage of leaving the bands essentially flat during the experiment. Measuring tunneling current versus applied voltage with the tip either in contact with the surface or far from the surface, both of which would be based on Fowler-Nordheim tunneling of electrons into the conduction band of the sample surface, could be fit to a tunneling model to find the location of the bands. A third method would be to attempt to independently measure the charge trapped in the oxide. If this were known, the flatband potential could be calculated relative to the midgap level.

Finding solutions to any of the issues discussed in this section would improve on the work described in this dissertation.

APPENDIX

STATE TO STATE FREQUENCY SHIFT CALCULATIONS

```
> ##########################################################
> ###  Method of images for two dielectric boundaries  ###
> ##########################################################
> ##this worksheet calculates the potential due to a charge
  ##next to a delectric plate and the frequency shift of an
  ##oscillating cantilever. It is based on
  ##Sometani, T.; Eur. J. Phys. 21 (2000) 549-554 and
  ##During, A.; APL 75 (1999) 433
> restart;
> ##global parameters. Changing them here changes them
  ##throughout the worksheet.
> ##eps1, eps2 relative dielectric constants;
  ##Q1, Q2 charges; D1, D2 depth of charges in oxide.
> ##A oscillation amplitude, f0 oscillation frequency,
  ##K spring constant, N number of terms in
  ##the image charge series to keep
> eps1:=4:  eps2:=1: eps0:=8.85e-12:
  Q1:=1.602e-19:  Q2:=Q1:  e:=1.602e-19:
  D1:=.5e-9:  D2:=.5e-9:
  A1:=1e-10:  f0:=160500:  K:=40:  N:=3:
> Phi:=q/4/Pi/epsilon1/epsilon0/abs(z - a + d)+sum(Vaa(n) + Vab(n) +
  Vbb(n) + Vba(n),n=1..N);
```

$$:= \frac{q}{4\,\pi\,\varepsilon1\,\varepsilon0\,|\,z - a + d|} + Vaa(1) + Vab(1) + Vbb(1) + Vba(1) + Vaa(2) + Vab(2) + Vbb(2) + Vba(2) + Vaa(3) + Vab(3) + Vbb(3) + Vba(3)$$

```
> beta:=(epsilon2-epsilon1)/(epsilon2+epsilon1);
```

$$\beta := \frac{\varepsilon2 - \varepsilon1}{\varepsilon2 + \varepsilon1}$$

```
> Vaa:=(n)->qaa(n)/4/Pi/epsilon0/(abs(z-a)+(2*n-2)*c+d);
```

$$Vaa := n \rightarrow \frac{qaa(n)}{4\,\pi\,\varepsilon0\,(|\,z - a|\, + (2\,n - 2)\,c + d)}$$

```
> Vab:=(n)->qab(n)/4/Pi/epsilon0/(abs(z-b)+(2*n-1)*c+d);
```

$$Vab := n \rightarrow \frac{qab(n)}{4\,\pi\,\varepsilon0\,(|\,z - b|\, + (2\,n - 1)\,c + d)}$$

```
> Vba:=(n)->qba(n)/4/Pi/epsilon0/(abs(z-a)+2*n*c+d);
```

$$Vba := n \to \frac{qba(n)}{4\,\pi\,\varepsilon 0\,(|\,z - a\,|\, + 2\,n\,c + d)}$$

```
> Vbb:=(n)->qbb(n)/4/Pi/epsilon0/(abs(z-b)+(2*n-1)*c+d);
```

$$Vbb := n \to \frac{qbb(n)}{4\,\pi\,\varepsilon 0\,(|\,z - b\,|\, + (2\,n - 1)\,c + d)}$$

```
> qaa:=(n)->beta^(2*n-1)*(-q)/epsilon1;
```

$$qaa := n \to -\frac{\beta^{(2\,n - 1)}\,q}{\varepsilon 1}$$

```
> qab:=(n)->beta^(2*n)*(-q)/epsilon1;
```

$$qab := n \to -\frac{\beta^{(2\,n)}\,q}{\varepsilon 1}$$

```
> qba:=(n)->beta^(2*n)*q/epsilon1;
```

$$qba := n \to \frac{\beta^{(2\,n)}\,q}{\varepsilon 1}$$

```
> qbb:=(n)->beta^(2*n-1)*q/epsilon1;
```

$$qbb := n \to \frac{\beta^{(2\,n - 1)}\,q}{\varepsilon 1}$$

```
> Phidi:=q/4/Pi/epsilon0/epsilon1/abs(z+d1);
  #this is for dielectric everywhere
```

$$Phidi := \frac{q}{4\,\pi\,\varepsilon 0\,\varepsilon 1\,|\,z + d1\,|}$$

```
> a:=0:  b:=c:  epsilon1:=eps1:  epsilon2:=eps2:
  q:=Q1:  epsilon0:=eps0:
```

```
> plot([subs(c=1e-9,d=D1,Phi), subs(d1=D1,Phidi)], z=-2e-9..2e-9, 0..5,
  numpoints=200);
  #the first plot is the potential due to a charge in
  #the dielectric with epsilon1. The second is the method
  #of images with the slab of epsilon2
```

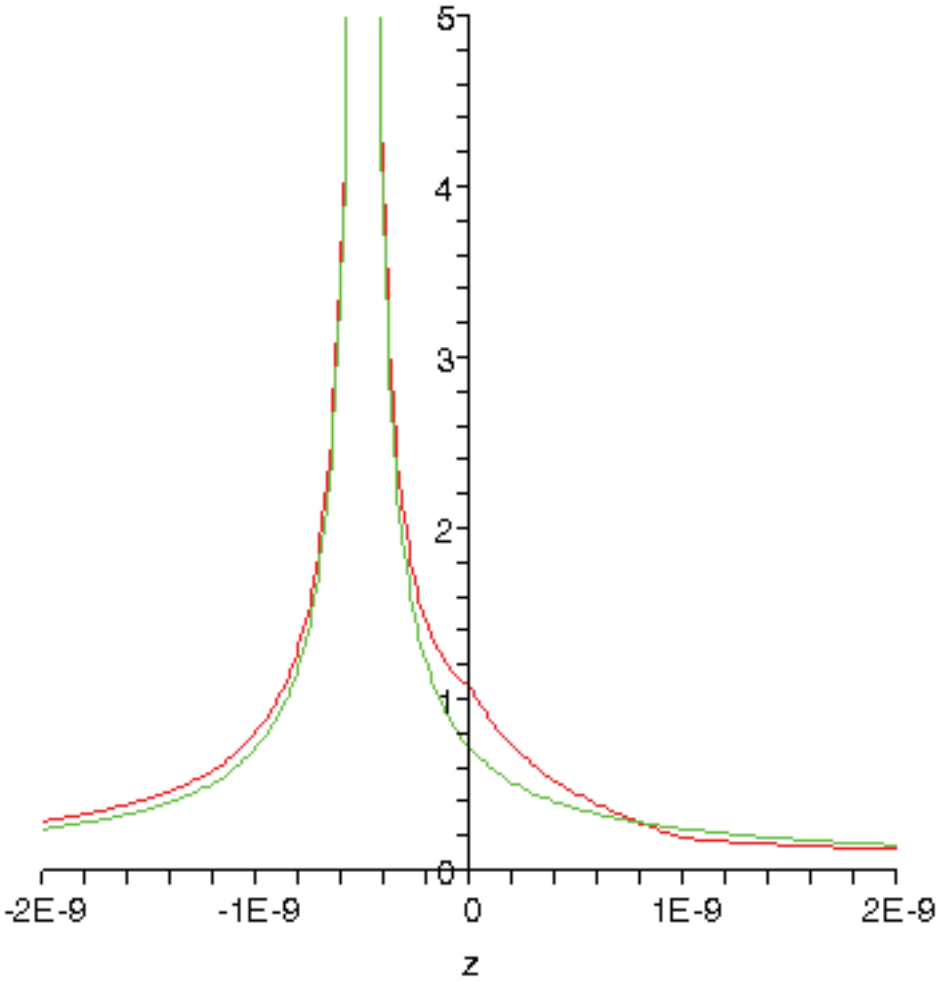


```
> plot([1/subs(c=1e-9,d=D1,Phi), 1/subs(d1=D1,Phidi)], z=-2e-9..2e-9,
  numpoints=200);
  ##the inverse of the potential for the same plots as above
```

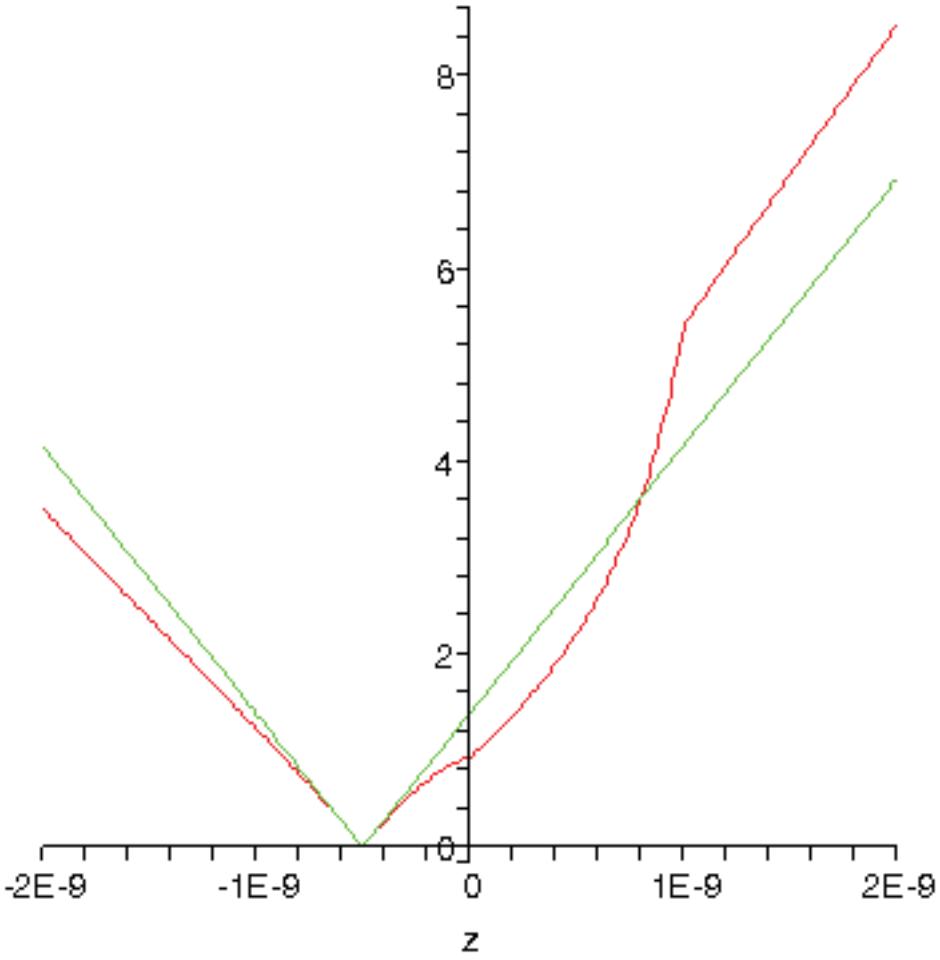


```
> ######  adding second charge. reset parameters   ########

> a:='a': b:='b': epsilon1:='epsilon1':
  epsilon2:='epsilon2': e:='e': q:='q':
  epsilon0:='epsilon0':

> Phinew1:=subs(z=(c+d1),d=d2,q=q2,Phi):
  ##this is the potential at the location (d1) of
  ##the first charge (q1), due to q2

> Phinew2:=subs(z=(c+d2),d=d1,q=q1,Phi):
  ##same as above, but for q2 at d2
  ##inside the other dielectric

> PhiP1:=subs(z=(-d1), d=d1, q=q1, Phi - q/4/Pi/epsilon1/epsilon0/abs(z
  - a + d)):
  ##this is the potential from q1, excluding the term
  ##with a singularity at z=-d1. This is the potential
  ##from the polarization.
```

```
> PhiP2:=subs(z=-d2, d=d2, q=q2, Phi - q/4/Pi/epsilon1/epsilon0/abs(z -
  a + d)):
  ##same as above, but with q2 at its depth d2

> ####################  parameters   ######################

> a:=0:  b:=c:  epsilon1:=eps1:  epsilon2:=eps2:
  e:=1.602e-19:  q:=e:  epsilon0:=eps0:

> Fimg:=-diff(PhiP1,c) * q1/2-diff(subs(a=0,b=c,z=-d1,Phinew1),c) *
  q1/2-diff(PhiP2,c)*q2/2-diff(subs(a=0,b=c,z=-d2,Phinew2),c) * q2/2:
  ##method of images force

> FGimg:=diff(Fimg,c):
  ##FG from method of images

> Fimg2:=diff(subs(a=0,b=c,z=-d1,Phinew1),c) * q1/2 -
  diff(subs(a=0,b=c,z=-d2,Phinew2),c) * q2/2:
  ##method of images force without polarization effects

> FGimg2:=diff(Fimg2,c): #FG from method of images without polarization

> ##Fimg2check:=-diff(subs(a=0,b=c,z=-d1,Phinew1),d2) *
  q1/2-diff(subs(a=0,b=c,z=-d2,Phinew2),d2)*q2/2:

> ##FGimg2check:=diff(Fimg2check,d2):

> ############################################################

> #########   dielectric (or vacuum) everywhere     ########

> ############################################################

> epsilon:='epsilon';
```

$$\varepsilon := \varepsilon$$

```
> Fdi:=q1*q2/4/Pi/epsilon0/epsilon/(d1+d2+c)^2;
  ##dielectric force (also vacuum case when epsilon=1)
```

$$Fdi := \frac{2.824858758\ 10^{10}\ q1\ q2}{\pi\ \varepsilon\ (c + d1 + d2)^2}$$

```
> FGdi:=diff(Fdi,c);
  ##FG for dielectric everywhere
```

$$FGdi := -\frac{5.649717516\ 10^{10}\ q1\ q2}{\pi\ \varepsilon\ (c + d1 + d2)^3}$$

```
> epsilon1:=eps1;
```

$$\varepsilon 1 := 4$$

```
> epsilon2:=eps2;
```

$$\varepsilon 2 := 1$$

```
> plot(subs(d1=D1,d2=D2,[subs(q1=Q1,q2=Q2,FGimg),
  subs(q1=2*e,q2=0,FGimg), subs(q1=e,q2=e,epsilon=1,FGdi),
  subs(q1=e,q2=e,epsilon=epsilon1,FGdi)]), c=0..3e-9,
  thickness=[2,2,2,2], color=[red, green, blue,black], numpoints=200);
  ##FG as a function of c (the tip-smple gap). In order of
  ##increasing magnitude at c=0: image method, dielectric
  ##everywhere, vacuum everywhere, two charges on one side.
```

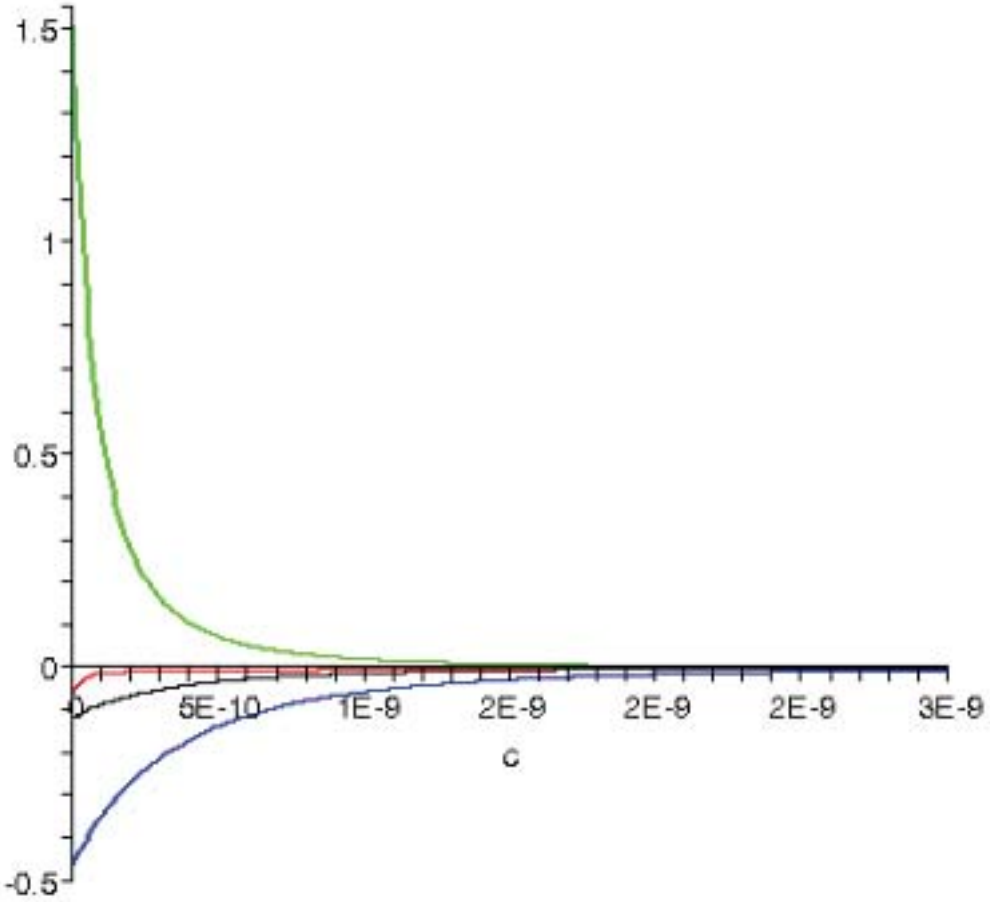


```
> plot(subs(d1=D1,d2=D2,[subs(q1=2*Q1,q2=0,Fimg), subs(q1=e,q2=e,Fimg),
  subs(q1=e,q2=e,epsilon=1,Fdi)]), c=0..3e-9,-2e-10..2e-10, color=[red,
  green,blue], thickness=2);
  ##Force as a function of c (the tip-smple gap).
  ##In order of increasing magnitude: image method,
  ##dielectric everywhere
```

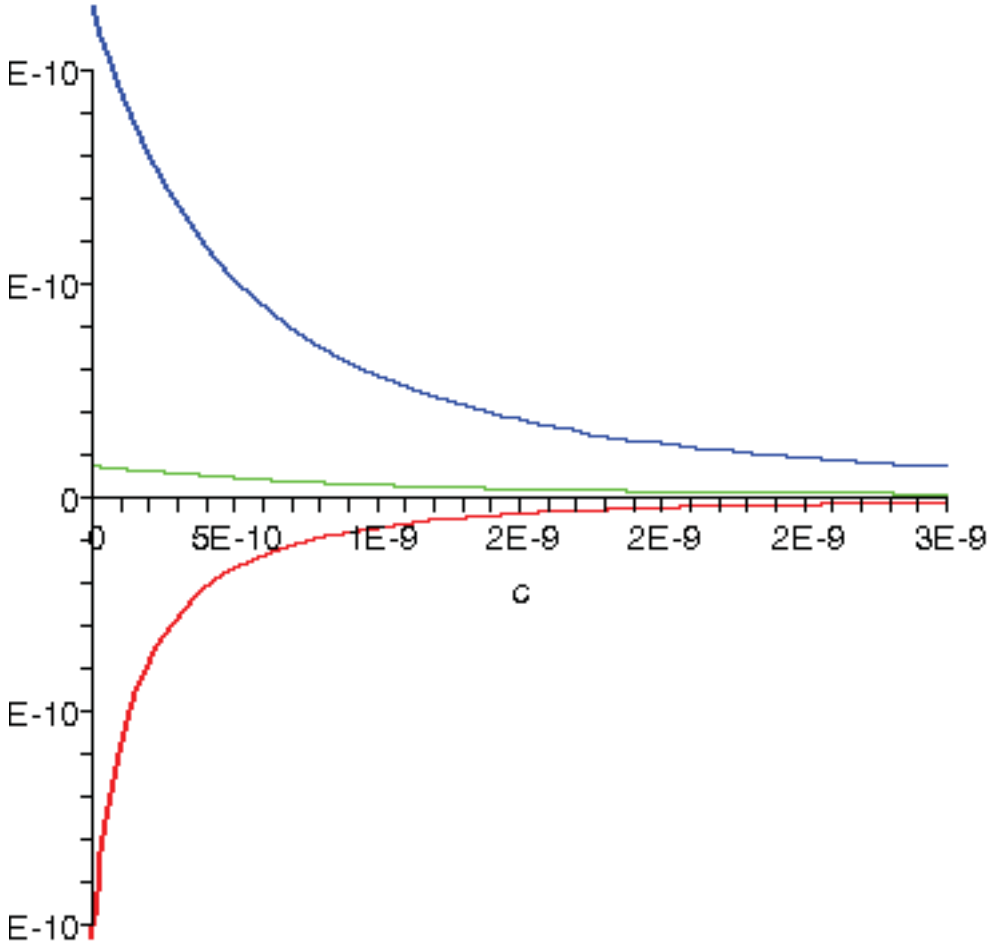


```
> evalf(subs(q1=Q1, q2=Q2, d1=D1, d2=D2, c=0, Fimg));
  ##image method force at c=0
```

$$1.644161854\ 10^{-11}$$

```
> evalf(subs(q1=Q1,q2=Q2,d1=D1,d2=D2,c=0,epsilon=epsilon1,Fdi));
  ##dielectric everywhere force for c=0
  ##(same separation distance as image force c=0)
```

$$5.769150884\ 10^{-11}$$

```
> ######################################################
> ##########    Effective Force Gradient   ############
> c:=Z+A*(1+U); A:=A1;
```

$$c := Z + A\,(1 + U)$$

$$A := 1\ 10^{-10}$$

```
> d1:=D1; d2:=D2; q1:=Q1; q2:=Q2;
```

$$d1 := 5\ 10^{-10}$$

$$d2 := 5\ 10^{-10}$$

$$q1 := 1.602\ 10^{-19}$$

$$q2 := 1.602\ 10^{-19}$$

```
> FGeffimg:=-2/(Pi*A)*int(-Fimg*U/(sqrt(1-A^2)),U=-1..1) assuming (Z>0);
  ##Warning: resource-intensive integration!
> deltafimg:=-1/2*f0*FGeffimg/K:
> evalf(subs(Z=0.4e-9,deltafimg));
```

$$7.674535970$$

```
> plot(deltafimg, Z=1e-11..2e-9, 0..15,thickness=2);
```

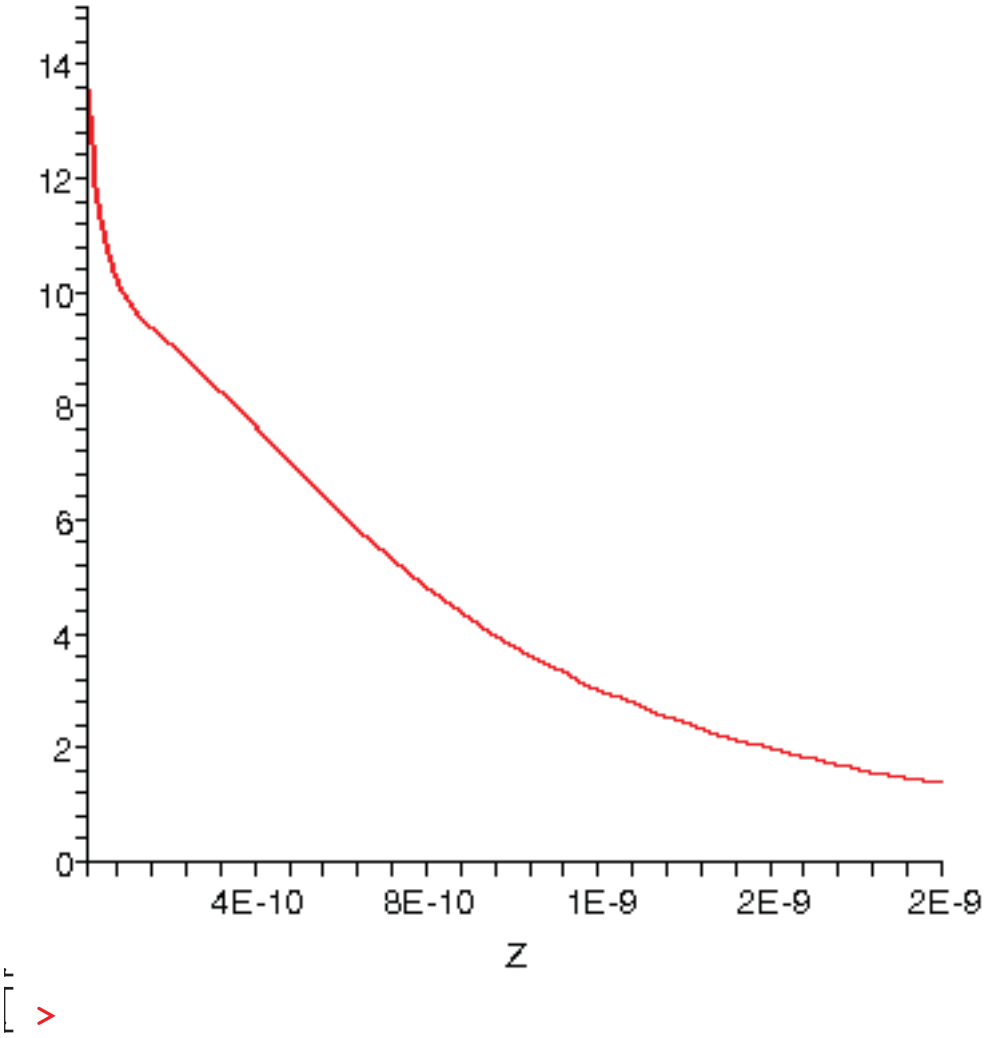
14
12
10
8
6
4
2
0
4E-10
8E-10
1E-9
2E-9
2E-9
Z